UNIVERSIDADE DA BEIRA INTERIOR
Ciências da Saúde

Desenvolvimento de novas abordagens terapêuticas para a regeneração da pele

Daniela Sofia Rodrigues Figueira

Dissertação para obtenção do Grau de Mestre em
Ciências Biomédicas
(2º ciclo de estudos)

Orientador: Prof. Doutor Ilídio Joaquim Sobreira Correia
Co-orientador: Mestre Sónia Alexandra Pereira Miguel
Mestre Tiago Ruivo Correia

Covilhã, junho de 2016

List of publications

Publication in a peer-reviewed international journal:

Fradique, R., Correia, T. R., Miguel, S. P., de Sá, K. D., Figueira, D. R., Mendonça, A. G., & Correia, I. J., *Production of new 3D scaffolds for bone tissue regeneration by rapid prototyping*. Journal of Materials Science: Materials in Medicine, 20016. *27*(4), 1-14.

Correia, T. R., Figueira, D. R., de Sá, K. D., Miguel, S. P., Fradique, R., Mendonça, A. G. & Correia, I.J., *3D printed scaffolds with bactericidal activity aimed for bone tissue regeneration*. International Journal of Biological Macromolecules, 2016. In press.

Ser digna na partida, na despedida,
Dizer adeus com jeito,
Não chorar para não enfraquecer o emigrante,
Mesmo que o emigrante seja o nosso irmão mais novo.
Dobrar-lhe as camisas,
Limpar-lhe as sapatilhas com um pano húmido,
Ajudá-lo a pesar a mala que não pode levar mais de 20 kg.
Quanto pesará o coração dele?
E o meu?
(...)
Nunca chorar!
Mesmo que o pai esteja a chorar,
Mesmo que estejam todos a chorar.
Acordar mais cedo para lhe fazer torradas antes da viagem,
Com manteiga, com doce de mirtilo,
Com tudo o que houver no frigorífico,
E não pensar que nunca mais seremos pequenos outra vez,
Cheios de mãe e de pai no quarto ao lado,
Cheios de emprego no quarto ao lado,
Quando ainda existia Portugal.
É tanto o que se pede a um ser humano no século XXI.
Que morra de medo e de saudade no aeroporto Francisco Sá Carneiro.
Mas que não chore.

Manual de despedida para Mulheres Sensíveis, Filipa Leal

À minha mãe Bela que sempre acreditou;
Ao meu pai Jorge que ainda não acredita.

Acknowledgments

A wise man once said that we should cultivate the habit of being grateful for every good thing that comes to our lives, and to give thanks continuously. Therefore, I wish to offer my most heartfelt thanks to the following people that somehow contributed for the work present in this dissertation.

First and foremost, I would like to express my deepest gratitude to my supervisor Professor Ilídio Correia, whose expertise, critical thinking, advices, and exigency made me grow up professionally. Without his guidance and constant feedback, this M.Sc. thesis would not have been achievable. It was a real privilege and honor to work with him.

Secondly, I must express my gratitude to Sónia Miguel, my co-supervisor, who is one of these unique people that "walk two miles when asked to walk one". I thank her for the all the knowledge she shared with me, for the companionship, constant support, and availability. Girl, there are no words for your kindness. I also would like to thank Tiago Correia for all his encouragement and co-supervision since my B.Sc. project.

I would also like to show my appreciation to Professor Abílio Silva for his help with the mechanical assays.

I must acknowledge all of my group colleagues for being always helpful and for the funny moments, either discussing Game of Thrones or the birthday cake Marco did not brought.

I have to offer my special thanks to my dearest friends who accompanied me throughout my academic life. To Marco Carvalho, Luís Xavier and Pedro Sousa I thank for the endless talks about endless subjects, for the laughs and for making me feel "one of the guys" during the long nights of study or fun in Travessa Escura. It was the closest I have ever been from a Friends episode and that is priceless.

Words cannot express how thankful I am to Kevin Sá, a.k.a. my part-time lover and full-time friend, for his endless love, enthusiasm and support. Most of all, I thank him for being such an adventurous partner who makes me happy and embraces every single challenge with me. We are growing up together distractedly, my love. "Grow old with me; the best is yet to be".

Finally, but by no means least, my gratitude goes to my family members who looked closely at my progress, kept encouraging me towards success and supported me financially. I am so grateful to my beautiful mom, Anabela Rodrigues, for his unwavering faith in me and in my abilities. Her humor has kept me sane while her optimism and persistence have pushed me in ways I could never have done for myself. Thank you for everything, but mostly for never once having said, "I

told you so". I also owe a special thank you to my father, Jorge Figueira, who showed me the true worth of hard work and the life that is not written in books.

To my gorgeous sister Márcia I thank for everything she taught me and for the inspiration she brings to my life. Her rebellion turned into poems and her heightened sensitivity to the promises of life are one the most beautiful realities of my life. To my brother Duarte, that little thing that keeps my eyes brilliant since the day he was born 5 years ago, I thank for all the strength he gives me, for surprising me with his shrewd eye on the world and for do not let dream came out of my life.

And I want to thank you, Lord, for life and all that is in it. Thank you for the day and for the hour, and the minute.

Grateful, so grateful.

Resumo

Todos os anos, milhões de pessoas em todo o mundo são vítimas de queimaduras, feridas crónicas ou feridas agudas que comprometem a integridade da pele. Tendo em vista a recuperação da pele lesada, uma das abordagens terapêuticas mais utilizadas consiste no uso de autoenxertos. Estes, no entanto, apresentam algumas limitações tais como a escassa disponibilidade de tecido dador e longos períodos de internamento hospitalar. Neste contexto, a engenharia de tecidos tem-se focado no desenvolvimento de matrizes sintéticas capazes de reproduzir a estrutura nativa da pele e promover a sua regeneração. Esta tese de mestrado apresenta o trabalho realizado ao longo dos últimos 9 meses onde foi produzida uma membrana com duas camadas através da técnica de eletrofiação que se pretende usar como substituto de pele. A camada superior da membrana era composta por ácido hialurónico e policaprolactona e foi concebida com o objetivo de atuar como barreira física contra agentes externos e ainda proporcionar o suporte mecânico necessário. Por outro lado, a camada inferior da membrana foi produzida com quitosano e zeína e posteriormente funcionalizada com ácido salicílico com o intuito de lhe conferir propriedades anti-inflamatórias e antimicrobianas. Os resultados obtidos revelaram que a membrana produzida possui porosidade, propriedades mecânicas e biocompatibilidade adequadas. Por outro lado, verificou-se a ausência de formação de biofilme durante, pelo menos, 5 dias. Os resultados obtidos revelam que a membrana possui as propriedades adequadas para ser usada na regeneração de feridas cutâneas.

Palavras-Chave

Ácido salicílico; electrofiação; engenharia de tecidos; membrana em bicamada.

Resumo alargado

A pele é o maior órgão do corpo humano, constituindo cerca de 8% da sua massa total. As principais funções da pele incluem proteção contra agentes externos, regulação da temperatura corporal e manutenção da homeostasia de líquidos. No entanto, a integridade deste órgão é frequentemente afetada por doenças ou trauma (ex. queimaduras). Geralmente, as lesões cutâneas têm uma elevada morbilidade associada e, em último caso, podem causar a morte do paciente.

Consoante o tipo e a duração do processo de cicatrização de feridas, as lesões cutâneas podem ser classificadas como agudas ou crónicas. A cicatrização de feridas é realizada através de uma cascata de eventos complexos e dinâmicos, que incluem a coagulação, inflamação, síntese e deposição de matriz extracelular, angiogénese, fibroplasia, epitelização, contração e remodelação. Tendo em vista a recuperação do tecido lesado, uma das abordagens clinicas mais recorrentes consiste na utilização de autoenxertos. No entanto, este tipo de terapia é limitado pela parca disponibilidade de tecido dador, particularmente em casos de pacientes com elevada percentagem do corpo queimada ou comprometida. Alternativamente, alguns cirurgiões recorrem ao uso de aloenxertos e xenoenxertos para o tratamento de lesões cutâneas. Porém, estas têm associado o risco de infeções e rejeições imunológicas. Para colmatar estas limitações, nas últimas décadas, a engenharia de tecidos tem desenvolvido vários substitutos de pele com o objetivo de acelerar o processo de cicatrização de feridas e restabelecer as funções da pele.

De acordo com a camada da pele que se tem que substituir, os substitutos de pele podem ser classificados como epidérmicos, dérmicos e dermo-epidérmicos. Os substitutos de pele podem ser produzidos com polímeros naturais e/ou sintéticos, sendo que alguns têm células incorporadas. Contudo, nenhum dos substitutos de pele produzidos até agora é capaz de reestabelecer, na íntegra, as propriedades funcionais e anatómicas da pele.

Entre uma diversidade de sistemas usados na promoção da cicatrização de feridas cutâneas, as membranas produzidas pelo processo de eletrofiação têm sido objetivo de intensa investigação nos últimos anos. A técnica de eletrofiação utiliza forças eletrostáticas para produzir malhas nanofibrosas com diâmetros entre 50-500 nm, que são semelhantes às dimensões das fibras de colagénio presentes na matriz extracelular. Esta semelhança estrutural torna as membranas produzidas por eletrofiação excelentes substratos para a adesão celular. Adicionalmente, a elevada porosidade e o baixo tamanho de poro permitem as trocas gasosas e conferem ainda proteção contra infeção bacteriana no local da ferida, respetivamente. Os exsudados das feridas são também eficazmente absorvidos pelas membranas devido ao seu elevado rácio área/volume, ajudando a manter um ambiente húmido no local da ferida. Por outro lado, estas estruturas nanofibrosas são conformáveis e adaptáveis a feridas com arquitetura irregular e podem ser facilmente funcionalizadas com moléculas que promovem o processo de cicatrização.

Desta forma, o presente estudo teve como objetivo a produção de uma membrana com duas camadas pelo processo de electrofiação para aplicação na regeneração de pele lesada. A camada superior da membrana era composta por ácido hialurónico e policaprolactona e foi desenvolvida com o intuito de proporcionar integridade estrutural ao sistema e simultaneamente constituir uma barreira física contra agentes externos. Por outro lado, a camada inferior foi concebida de forma a estimular o processo de cicatrização e ainda possuir propriedades antimicrobianas e anti-inflamatórias. Para tal, foi produzida uma membrana nanofibrosa composta por quitosano e zeína com ácido salicílico incorporado.

Após otimizado o processo produção, procedeu-se à caracterização físico-química e biológica da membrana. Os resultados obtidos revelaram que a membrana produzida possui porosidade, propriedades mecânicas e biocompatibilidade adequadas. Por outro lado, verificou-se a ausência de formação de biofilme na superfície da membrana durante pelo menos 5 dias. Os resultados obtidos revelam que a membrana possui as propriedades adequadas para ser usada na regeneração de feridas cutâneas.

Abstract

Every year, millions of patients suffer burns, chronic or surgical-related wounds. Autografts are still the gold standard used for the treatment of these injuries, although they have several drawbacks like limited availability of donor sites, patient morbidity, and long periods of hospitalization. To surpass such drawbacks, several studies have been focused on the development of polymeric matrices that are able to reproduce the skin native structure and also improve its regeneration. Herein, a bilayer membrane was produced by electrospinning and its properties have been characterized through *in vitro* assays. The upper layer of the membrane was comprised of hyaluronic acid and polycaprolactone in order to provide mechanical support and also to act as a physical barrier against external threats. Chitosan and zein were used to produce the bottom layer. Furthermore, salicylic acid was also incorporated in this layer for conferring anti-inflammatory and antimicrobial properties to the membrane. The obtained results showed that the produced electrospun meshes display an ideal porosity, appropriate mechanical properties, controlled evaporative water loss and an initial burst release of SA. Moreover, the membranes did not exhibit any toxic effects for human fibroblast cells and promoted their adhesion, spread, and proliferation. In addition, no biofilm formation was noticed on their surface along the experiments. The obtained data reveal that this electrospun membrane possesses the required properties to be used in wound healing.

Keywords

Bilayer membrane; electrospinning; salicylic acid; skin tissue engineering.

Contents

1. Introduction 2

1.1. Skin 2

1.1.1. Functions and structure 2

1.1.1.1. Epidermis 3

1.1.1.2. Basement Membrane 4

1.1.1.3. Dermis 5

1.1.1.4. Hypodermis 5

1.1.1.5. Skin appendages 5

1.2. Wounds 6

1.2.1. Wound Healing 8

1.2.1.1. Normal Wound Healing 9

1.2.1.2. Non-healing Wounds 11

1.2.2. Wound Healing Therapies 11

1.2.2.1. Autografts, allografts, and xenografts 11

1.2.2.2. Skin Tissue Engineering 12

1.3. Nanofibrous membranes produced by electrospinning 15

1.3.1. Electrospun nanofibrous membranes produced with natural polymers 17

1.3.1.1. Chitosan 18

1.3.1.2. Hyaluronic Acid 18

1.3.1.3. Zein 19

1.3.2. Electrospun nanofibrous membranes produced with synthetic polymers 19

1.3.2.1. Polycaprolactone 20

1.4. Antimicrobial Agents 20

1.4.1. Salicylic Acid 21

1.5. Aims 21

2. Materials and Methods 23

2.1. Materials 23

2.2. Methods 23

2.2.1. Deacetylation of Chitosan 23

2.2.2. Production of the electrospun bilayer membrane 23
2.2.4. Characterization of the mechanical properties of EBM 25
2.2.5. Evaluation of the porosity of EBM 25
2.2.6. Contact angle analysis of EBM 26
2.2.7 Water vapor transmission rate (WVTR) of EBM 26
2.2.8. Characterization of EBM biodegradation profile 26
2.2.9. Characterization of the release profile of SA 26
2.2.10. Characterization of the biological properties of EBM 27
2.2.10.1. Evaluation of cell viability and proliferation in the presence of EBM 27
2.2.10.2. Confocal microscopic analysis 27
2.2.10.3. Evaluation of the antimicrobial properties of EBM 27
2.2.11. Characterization of the morphology and biological performance of the EBM by SEM analysis 28
2.2.12. Statistical Analysis 28
3. Results and discussion 30
3.1. Deacetylation of Chitosan 30
3.2. Morphological characterization of the scaffolds 30
3.3. Attenuated Total Reflectance-Fourier Transform Infrared Spectroscopic analysis 32
3.4. Characterization of the mechanical properties of the EBM 33
3.5. Evaluation of the porosity of EBM 35
3.6. Determination of contact angle at the surfaces of EBM 36
3.7. Water vapor transmission rate 37
3.8. Characterization of the biodegradation profile of EBM 38
3.8. Determination of SA release from EBM 40
3.9. Evaluation of cell viability and proliferation in the presence of EBM 41
3.10. Characterization of the antimicrobial properties of the produced membranes 44
4. Conclusion 48
5. Bibliography 50
Appendix 60

List of figures

Figure 1. Schematic representation of the structure of normal skin tissue. 2
Figure 2. Representation of the structure of the skin. 4
Figure 3. Representation of the different type of skin wounds 7
Figure 4. Representation of the healing process 8
Figure 5. Schematic representation of the five stages of wound healing process 10
Figure 6. Representation of a tissue engineering strategy used to regenerate a functional tissue 12
Figure 7. Representation of a conventional electrospinning apparatus 16
Figure 8. Chemical structure of natural and synthetic polymers 17
Figure 9. Schematic representation of the setup used to produce the EBM 24
Figure 10. Representative macroscopic images of the top and bottom view of the produced EBM. 31
Figure 11. Macroscopic and SEM cross-section images of the EBM. 32
Figure 12. ATR-FTIR analysis of the EBM and raw materials 33
Figure 13. Representative stress–strain curve and macroscopic images of the EBM during the tensile test. 34
Figure 14. Characterization of the porosity of the EBM 36
Figure 15. Characterization of the water contact angles of EBM 37
Figure 16. Characterization of the water vapor transmission profile of EBM 37
Figure 17. Evaluation of weight loss of EBM 39
Figure 18. SEM images of EBM after 1, 3 and 7 days of being incubated with PBS. 40
Figure 19. Release profile of SA from electrospun EBM 41
Figure 20. Microscopic images of NHDF in the presence of EBM 42
Figure 21. Evaluation of NHDF viability when cultured in the presence of EBM 43
Figure 22. SEM micrographs of fibroblasts morphology at surface of EBM. 43
Figure 23. CLSM images of fibroblasts in contact with EBM 44
Figure 24. Evaluation of the bactericidal activity of EBM 45
Figure 25. SEM images of EBM in contact with *S. aureus* 46

List of tables

Table 1. Tissue-engineered skin constructs commercially available 14
Table 2. Degree of deacetylation of the different CS 30
Table 3. Mechanical parameters of EBM and native human skin 35
Table 4. Water vapor transmission profile of EBM 38

Acronyms

1DUVS	First Derivative UV-spectroscopy
3D	Three-Dimensional
ATR-FTIR	Attenuated Total Reflectance-Fourier Transform Infrared Spectroscopy
bFGF	Basic Fibroblast Growth Factor
CFU	Colony Forming Units
COX	Cyclooxygenase
CS	Chitosan
CSLM	Confocal Laser Scanning Microscopy
DD	Deacetylation
DETCs	Dendritic γδ Epidermal T Cells
DMEM-F12	Dulbecco's Modified Eagle's Medium
DMF	Dimethylformamide
DMSO	Dimethyl Sulfoxide
EBM	Electrospun Bilayer Membrane
ECM	Extracellular Matrix
EDTA	Ethylenediaminetetraacetic Acid
EGF	Epidermal Growth Factor
EtOH	Ethanol
FBS	Fetal Bovine Serum
FGF	Fibroblast Growth Factor
HA	Hyaluronic Acid
HB-EGF	Heparin-Binding Epidermal Growth Factor
HIV	Human Immunodeficiency Virus
LMW	Low Molecular Weight
MMPs	Matrix Metalloproteinases
MPa	Megapascal
MTT	3-(4,5-dimethylthiazol-2-yl)-2,5-diphenyltetrazolium bromide
NHDF	Normal Human Dermal Fibroblasts
PBS	Phosphate-Buffered Saline Solution
PCL	Polycaprolactone
PDGF	Platelet-Derived Growth Factor
PEG	Poly(ethylene glycol)
PFA	Paraformaldehyde
PLA	Poly(lactic acid)
RGD	Arginine-Glycine-Aspartic Acid
RT	Room Temperature

SA	Salicylic Acid
SEM	Scanning Electron Microscopy
TFE	Trifluoroethanol
TFG-ß	Transforming Growth Factor-ß
TIMP	Tissue inhibitor of Metalloproteinase
TNF-α	Tumor Necrosis Factor-α
UV	Ultraviolet
VEGF	Vascular Endothelial Cell Growth Factor
WVTR	Water Vapor Transmission Rate
ZN	Zein
ZnO	Zinc Oxide

Chapter I - Introduction

1. Introduction

1.1. Skin

1.1.1. Functions and structure

Skin is the largest and heaviest organ of the human body, with an area of 1.5–2.0 m^2 and a weight of 3.5–10 kg [1]. This complex organ is the outermost barrier of the body that protects inner organs from microbial pathogens, mechanical and chemical insults, regulates the body temperature, gives support to blood vessels and nerves, and prevents dehydration. Furthermore, it is also involved in the immune surveillance and sensory detection process [2].

Anatomically and functionally, the skin is formed by three connected layers, the epidermis, the dermis and the hypodermis (figure 1). The basement membrane separates physically epidermis from the dermis, acting as a consistent and dynamic interface [3]. Associated with the skin layers are various appendages such as hair follicles, nails, sweat and sebaceous glands that play different functions [4]. A more detailed description of the structure of the human skin is given in the following sections.

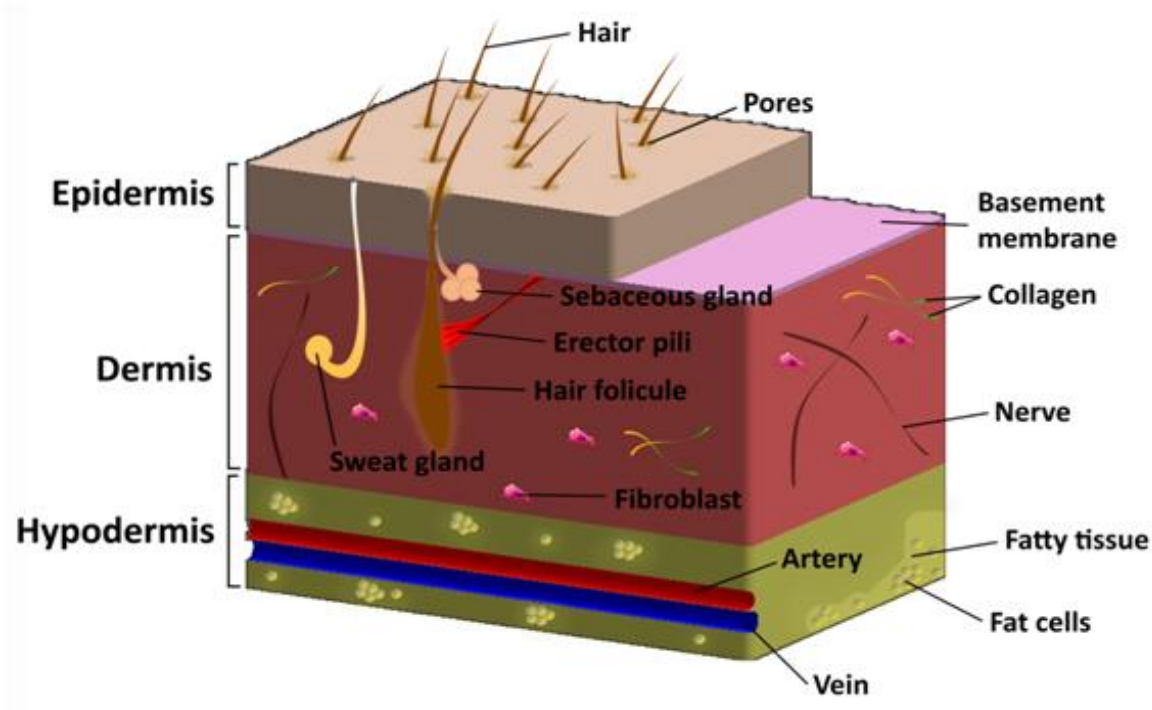

Figure 1. Schematic representation of the structure of normal skin tissue.

1.1.1.1. Epidermis

Epidermis is the most superficial layer of the skin and it is composed of stratified squamous epithelium. Epidermis thickness varies according to body location [4]. The main function of the epidermis is to protect the skin from potential threats and also to act as an efficient barrier at the top of the skin [5]. As can be observed in figure 2A, the epidermis is composed of five distinct cell layers, according to the different stages of keratinocyte maturation. From the deepest to the most superficial, these layers are known as *strata basale*, *spinosum*, *granulosum*, *lucidum*, and *corneum* [6].

The *stratum basale* consists in several layers containing cuboidal nucleated epithelial cells, also known as skin stem cells. These stem cells have a high self-renewal capacity and move upwards while they differentiate [3]. Initially, they are in the *stratum basale* and then they migrate to the *stratum spinosum* where the keratinization process begins. At this stage, cells start to lose their cytoplasm, suffer shape variation and start to synthesize keratin [7]. In the *stratum granulosum*, differentiated keratinocytes are highly active and accumulate lipid granules that are critical for the maintenance of a water barrier due to its hydrophobic nature. In fact, while delivering the content of the secretory lamellar granules to the intercellular spaces, the keratinocytes present in this layer become flat and spread. In *strata lucida* and *corneum*, cells enter into the programmed cell death process and all of the cytoplasmic organelles are degraded [4]. The *stratum corneum* is the most external layer of the epidermis and represents the final stage of keratinocyte differentiation [8]. It is composed of 10-20 layers of completely differentiated dead keratinocytes, known as corneocytes, that are interspersed with intercellular lipids, mainly ceramides and sphingolipids [5]. The keratinized *stratum corneum* is in direct contact with the environment and provides the main barrier to prevent water loss and penetration of hazard agents. Keratinocytes migration from the *stratum basale* to the outer *stratum corneum* takes approximately 28 days [9].

In addition to keratinocytes, which account for about 80% of epidermal cells, the epidermis is also composed by melanocytes, responsible for the pigmentation, Langerhans cells, which play a sensory role, and Merkel cells that are involved in the skin immune defense system [6, 7].

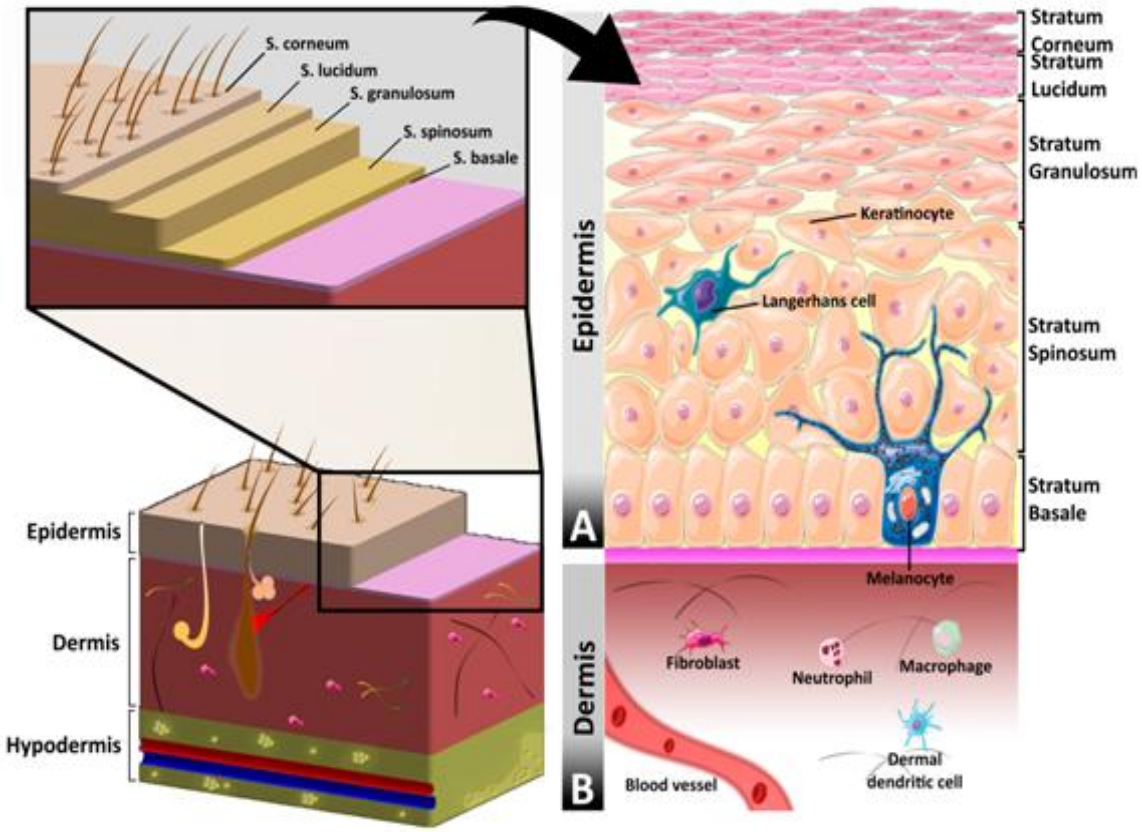

Figure 2. Representation of the structure of the skin. The outermost layer of the epidermis, the stratum corneum, is fundamental for avoiding microorganisms penetration and also protect the skin from environmental insults. The other strata (lucidum, granulosum, spinosum and basale) are fundamental for the remodeling of the stratum corneum. The epidermis also contains Langerhans cells and melanocytes (A). The dermis has as mainly cellular components the fibroblasts but also contains cells of the immune system (neutrophils and macrophages), blood vessels, and nerve fibers (B).

1.1.1.2. Basement Membrane

In the basal surface of the epithelium, it is found the basement membrane that is responsible for establishing a functional link between the epidermis and the dermis. Skin basement membrane has a thickness of 50-100 nm and it is composed of two main regions: a) lamina lucida, the layer closer to the epidermis, composed of laminin, entactins, and dystroglycans and b) lamina densa that is located above the papillary dermis and is mostly formed by collagen type IV [10,11]. This junction regulates the permeability to substances that migrate from the dermis to epidermis and vice versa [12]. Epidermis attachment to the basement membrane is ensured by hemidesmosomes that bind to the keratin filaments of keratinocytes. In turn, the basement membrane is bound to the dermal layer through fibrils of collagen VII that are interspersed into the papillary dermis [13].

1.1.1.3. Dermis

The dermis is located below the basement membrane and is the major component of human skin, with 3-5 mm thick. This layer supplies energy and nutrition to the overlying epidermis and also provides mechanical integrity to the skin due to the arrangement of collagen fibers that are deposited by local fibroblasts [7].

The dermis is composed of two distinct layers: the upper papillary dermis and the deeper reticular dermis [3]. The papillary dermis is essentially composed of loose connective tissue, namely elastin fibers interspersed with collagen fibers. It also holds numerous blood vessels that assure nutrients delivery, remove waste products and also allow the regulation of the body temperature. In turn, the reticular dermis is denser and composed by larger collagen fibers that confer flexibility to the skin [14]. Fibroblasts are the main cell type found in the dermis and they are responsible for the production and deposition of extracellular matrix (ECM) components. The dermal layer also contains cells of the immune system (neutrophils and macrophages), lymphatic vessels, nerve fibers, sweat and sebaceous glands, the deep portion of hair follicles and endothelial cells (figure 2B) [4].

1.1.1.4. Hypodermis

Hypodermis is the deepest skin layer and it is mainly composed of adipose tissue. This layer insulates the body and provides mechanical protection against physical shock [15]. Structurally, hypodermis is divided into lobules containing adipose cells separated by fibro-vascular septa. The septa are composed of collagen and reticulin fibers, blood and lymphatic vessels. In addition to adipose cells, hypodermis also contains fibroblasts and macrophages, that have an important role in the stimulation of thermogenesis during cold exposure or exercise [3].

1.1.1.5. Skin appendages

Skin has a variety of appendages, such as hair, nails, sebaceous and sweat glands, which maintain and protect the skin and their functions as explained in the following topics.

- **Hair**

Hair, a unique mammalian trait, has important functions in thermoregulation, physical protection, sensory activity, and social interactions. Each hair arises through a tubular invagination of the epidermis into the dermis [6]. Histologically, hair is arranged in three concentric layers - the inner layer or medulla, the middle layer or the cortex and the outer layer or cuticle – that are composed of keratin [4, 16]. Hair follicles are distributed over the entire surface of the body, although there are specific regions of the body where they are absent (soles of the feet, palms of the hands, glans penis, clitoris, labia minora, and mucocutaneous junctions). At the proximal end of the hair follicle is the hair bulb that contains a population of hair stem cells [6].

- **Nail**

The nail is a highly keratinized structure that grows on the dorsal tip of the fingers [17]. Nail functions include physical protection of the end of the fingers and toes, assistance in manipulation and scratching [18]. The nail unit is composed of the proximal nail fold, the nail matrix, the nail bed and hyponychium, which together form and support the nail plate, which is a keratinized structure that continuously grows throughout life [18, 19]. The nail is also composed of water, lipids and trace elements like iron, zinc, and calcium [16].

- **Sebaceous Glands**

Sebaceous glands are holocrine glands that are widely distributed throughout the skin but are mainly associated with hair and, therefore, concentrated on the face and scalp. Furthermore, they are absent from the palms, soles, and dorsum of feet [20]. Sebaceous glands often open directly into the hair follicle and produce sebum, an oily complex of triglycerides, fatty acids and their breakdown products (wax esters, squalene and cholesterol esters). Due to its lipid-hydrophobic composition, sebum acts as a natural lubricant that protects the skin against friction and avoids its dehydration [6].

- **Sweat Glands**

Sweat glands are located within the dermis. They are composed of coiled tubes and found all over the skin, but in abundance on palms, soles, axillae and forehead [6, 16, 17]. These glands secrete sweat, which is fundamental for the thermoregulation and excretion of metabolites [17]. There are two types of sweat glands – eccrine and apocrine – according to their secretory mechanism. The eccrine sweat glands secrete high amounts of an aqueous liquid following a merocrine mechanism. In turn, the apocrine glands secrete low amounts of a lipid-rich liquid and join up into the hair canal instead of the skin surface [21].

1.2. Wounds

Due to its exposition to environmental conditions, the skin suffers different types of lesions and diseases that compromise its structure and functions. According to the US Wound Healing Society, wounds are defined as the result of disruption of normal anatomic structure and functions of the skin [22].

Wounds - particularly surgical incisions, thermal injuries and chronic ulcers - are a major medical issue, since they lead to physical incapacity and ultimately to the death of the patient [23,24]. In fact, every year, more than 70 million surgical procedures are performed just in the United States of America with more than one-third resulting in hypertrophic scarring or keloid formation [25]. It is also estimated that burn injuries affect more than 11 million people worldwide annually [25, 26]. On the other hand, the number of patients suffering from chronic wounds, mainly pressure

ulcers, and diabetic foot ulcers, is increasing and affects nowadays more than 1% of the worldwide population [27].

According to the number of skin layers that are damaged, wounds can be divided into superficial, superficial partial-thickness, deep partial thickness, and full thickness, as depicted in figure 3 [28, 29].

- **Superficial injuries,** typically caused by sunburns, light scalds and grazing. They are usually able to self-renewal within few days, due to the presence of epidermal stem cells. Such injuries do not require specific surgical treatment since only the epidermis is affected. Moreover, this type of lesions regenerates rapidly without scarring, since no ECM deposition occurs.

- **Superficial partial-thickness injuries** affect the epidermis and the upper part of the dermis. This type of injury is followed by epidermal blistering and severe pain to the patient. They usually heal rapidly (≈2 weeks) in a healing process that involves the epithelialization from the margins of the wound through basal keratinocytes that migrate from the wound edge, hair follicles or sweat glands. In fact, the rate of skin regeneration depends on the density of these skin appendages. For example, thin hairless skin (e.g. inner arm, eyelids) heals more slowly than hairy skin (e.g. back, scalp).

- **Deep partial-thickness injuries** involve a dermal damage, where the skin appendages are destroyed and they are characterized by a slow healing. Scarring is pronounced in this type of injuries since fibroplasia is more intensive when compared with superficial partial-thickness wounds.

- **Full-thickness injuries** involve the complete destruction of the epidermis and dermis. Sometimes, this type of injury can also affect the hypodermis, muscle, and even bone. Skin appendages are destroyed and, therefore, there is no potential source to trigger epithelial regeneration. Full-thickness skin wounds lead to extensive scarring, cause mobility restrictions and cosmetic issues to the patients. If not properly treated, the full thickness damaged tissue will start to break down providing a perfect nutrient source and environment for invading microorganisms.

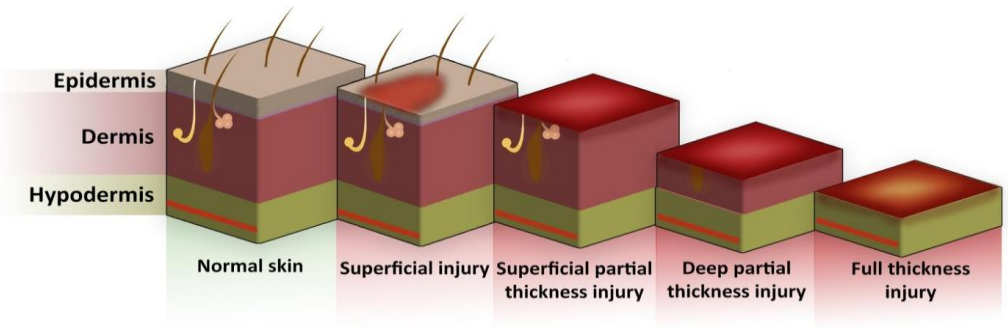

Figure 3. Representation of the different types of wounds that affect skin integrity.

1.2.1. Wound Healing

Wound healing is a complex biological process that allows the restoration of skin integrity. Based on the nature of the healing process, wounds can be divided in acute and chronic. Acute wounds (figure 4A) occurs as a consequence of mechanical injuries (abrasions, superficial, surgical or traumatic wounds) [27]. In this type of injury, the normal wound healing process occurs (see section 1.2.1.1. for further details) [30]. In turn, chronic wounds (figure 4B) are usually associated with comorbidity conditions, such as diabetes, obesity, tumor or microbial infection. In this type of wound, the healing process is not effective and a state of pathologic inflammation occurs (see section 1.2.1.2.) [30, 31].

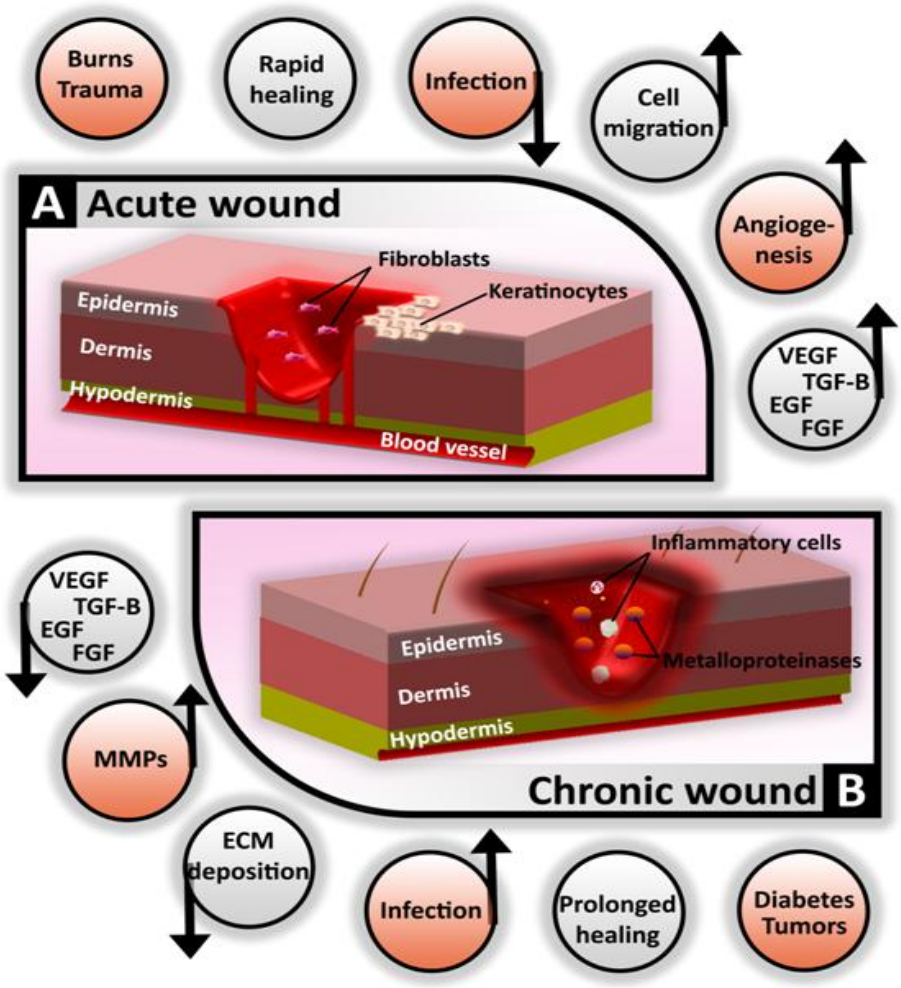

Figure 4. Representation of the healing process that occurs in acute and chronic wounds. Acute wound healing (A) is characterized by cell migration, proliferation and also by the secretion of high levels of growth factors that are involved in the stimulation of the synthesis of new ECM; Chronic wound healing (B) is characterized by an exuberant inflammation, increased MMPs production that impairs cell proliferation and hence delays the formation of the new skin tissue.

1.2.1.1. Normal Wound Healing

The normal wound healing process involves a series of coordinated events including bleeding and coagulation, acute inflammation, cell migration, proliferation, differentiation, angiogenesis, re-epithelialization, synthesis and remodeling of ECM [24]. These complex events can be divided into five overlapping steps: wounding (A), hemostasis (B), inflammation (C), proliferation (D) and remodeling (E) (see figure 4 for further details).

- **Wounding**

The wounding phase (figure 5A) is the first stage of the wound healing process. After the skin damage occurs, the wound site is filled with fluids from injured blood and lymphatic vessels. At this point, bacteria start to invade the open and unprotected wound [32].

- **Hemostasis**

Hemostasis begins immediately after the injury occurs in order to prevent bleeding. This process involves the formation of a provisional matrix at the wound site (figure 5B). The extrinsic and intrinsic coagulation cascades are activated, leading to platelet aggregation. Such event promotes the vasoconstriction of the injured vessels, reducing blood loss and simultaneously filling the tissue gap with a blood clot comprised of fibrin, fibronectin, vitronectin, and thrombospondin. The clot also acts as a provisional matrix for the migration of leukocytes, keratinocytes, fibroblasts, endothelial cells and growth factors during the wound healing process [32, 33].

- **Inflammation**

The inflammatory phase of the wound healing is represented on figure 5C. It occurs hemostasis and can last up for 6 days. This phase is characterized by the sequential influx of immune cells. Specifically, monocytes that migrate to the wound site, where they differentiate into macrophages and remove bacteria and foreign material through phagocytosis. Monocytes are attracted to the wound site by several chemoattractive agents, such as clotting factors, platelet-derived growth factor (PDGF), transforming growth factor-ß (TGF-ß), elastin and collagen breakdown products. In the wound, macrophages produce numerous growth factors, such as TGF-ß, tumor necrosis factor-α (TNF-α), heparin-binding epidermal growth factor (HB-EGF), and fibroblast growth factor (FGF) that are involved in the activation of keratinocytes, fibroblasts, and endothelial cells. Mast cells are also active in this phase and release granules filled with enzymes, histamine, and other active amines. These mediators are responsible for the characteristic symptoms associated with inflammation, i.e. *rubor* (redness), *calor* (warmth), *tumor* (swelling), *dolor* (pain) and *functio laesa* (loss of function). Lymphocytes, particularly $CD4^+$, $CD8^+$, and dendritic γδ epidermal T cells (DETCs), arrive approximately 6 days after the injury occur and participate in the following stages of the wound healing [32, 34, 35].

- **Proliferation**

The proliferative phase starts on the 6th day after the injury occurs and lasts for about 3 weeks (figure 5D). It is characterized by the re-epithelization of epidermis, repair of the dermal layer and neovascularization. At this stage, keratinocytes migrate from the surrounding tissue to the wound, where they became organized in stratified layers. This migration is stimulated by connexins and by the contact established between the keratinocytes and fibrin molecules. It is noteworthy that the migration, proliferation, and differentiation of the keratinocyte cells lead to the closure of the epithelial gap and to the restoration of the epithelium. On the other hand, the dermis is restored by fibroblasts that synthesize and secrete new ECM. The migration of fibroblasts into the wound is facilitated by ECM-cleaving matrix metalloproteinases (MMPs) that are produced by these cells. Furthermore, fibroblasts attach to the fibrin matrix and produce collagen (predominantly type I). As the collagen matures, intramolecular and intermolecular cross-links are created, increasing the strength of the new skin tissue. Simultaneously, the wound microenvironment, which is characterized by low pH, reduced oxygen content, and high concentration of lactate contribute for triggering the angiogenic process. This process is also stimulated by vascular endothelial cell growth factor (VEGF), basic fibroblast growth factor (bFGF), and TGF-β [21, 34, 36].

- **Remodeling**

The remodeling of the wound is the final phase of the normal wound healing process and may last for 1–2 years or even longer (figure 5E). In this phase, all the processes that were activated after injury occurrence cease. Specifically, it is verified the degradation and replacement of immature ECM, the return to a normal vascular density and the apoptosis of inflammatory cells at the wound site. All of these changes lead to the contraction of the wound and to the formation of acellular scar tissue. Although the remodeling process continues for a long period of time, the scar tissue does not achieve the strength of the native skin [32, 34, 36].

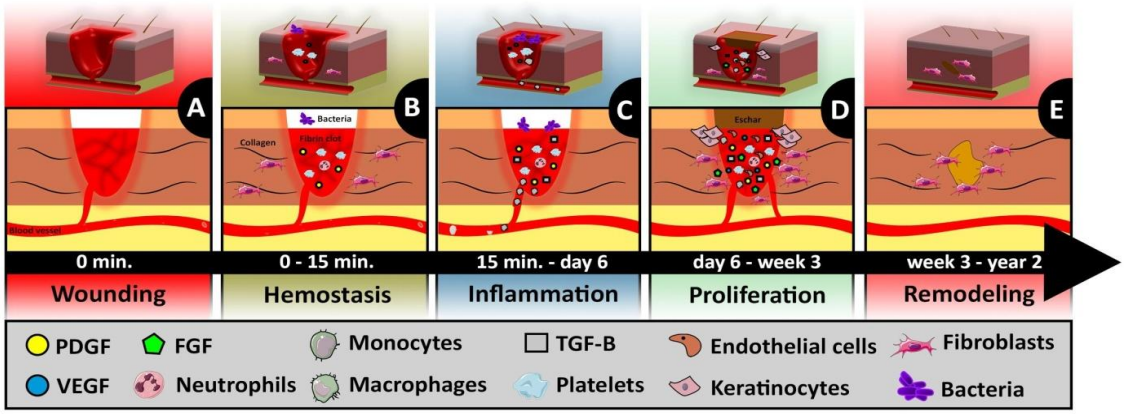

Figure 5. Schematic representation of the five stages that characterize the normal wound healing process. During wounding damaged skin is vulnerable to bacteria invasion (A). The hemostasis is characterized by the

formation of a clot that becomes a provisional ECM (B). Inflammatory phase is characterized by inflammatory cells infiltration (C). In the proliferative phase, new fibroblasts and keratinocytes migrate into the wound, in order to perform the re-establishment of the dermal layer and the re-epithelization of the epidermis, respectively (D). In remodeling, the wound contracts and an acellular scar tissue is formed. The chronologic duration of each phase of the wound healing is also represented in the figure.

1.2.1.2. Non-healing Wounds

Non-healing wounds occur in situations where the normal healing process is delayed, incomplete, and does not follow the proper order [30]. A chronic wound is continuously subjected to inflammation that is caused by an excessive infiltration of neutrophils and, therefore, is unable to progress through the normal stages of the wound healing [34]. This up-regulation of the inflammatory cascade can be caused by pressure, bacterial overgrowth, leukocyte trapping or ischemic injury. Neutrophils release the enzyme elastase, which is capable of destroying important healing factors, such as PDGF and TGF-ß that promote proliferation and ECM deposition. Moreover, the mitogenic activity of cells is suppressed in chronic wounds and they cannot enter into the proliferative phase, unlike what happens in normal wound healing process. It is noteworthy that the time required for chronic wound healing is increased and, in some cases, the wound size increases over time [31].

1.2.2. Wound Healing Therapies

1.2.2.1. Autografts, allografts, and xenografts

Autologous skin grafts are still the gold standard used in the clinic for the treatment of full-thickness skin wounds [37]. Before the autografting process, an early excision of the damaged skin tissue is performed [38]. Subsequently, the autograft procedure is performed with a dermatome that cuts thin slices of the epidermis and initial part of the dermis of the patient uninjured skin, which are subsequently transplanted to the wound site [39]. Such grafting procedure provides sufficient coverage without risk of rejection but presents serious drawbacks like limited availability of donor sites, induction of scar formation, patient morbidity, and long periods of hospitalization [2].

Alternatively, allograft and xenograft procedures have also been used for the treatment of severe wounds. In this case, implantable skin is collected from human and non-human cadavers, respectively. However, these procedures cannot be seen as efficient therapeutic alternatives to autografts since they present risks of viral transmission (e.g., hepatitis B and C or HIV), immune rejection and their use are dependent on tissue availability on skin banks [2, 39].

Hence, in the last few years, researchers from Tissue Engineering field attained significant progress in the development and clinical use of improved skin substitutes that are able to surpass some of the limitations associated with auto-, allo-, and xenografts.

1.2.2.2. Skin Tissue Engineering

Tissue engineering is an interdisciplinary field that combines the principles and methods of engineering and life sciences toward the development of biologic substitutes that are able to restore, maintain, or improve the functions of native tissues. The main strategy used in the area of tissue engineering involves cell seeding in contact with biomaterials, which serve as temporary scaffolds, in order to restore the structure and functions of a tissue (see figure 6) [40].

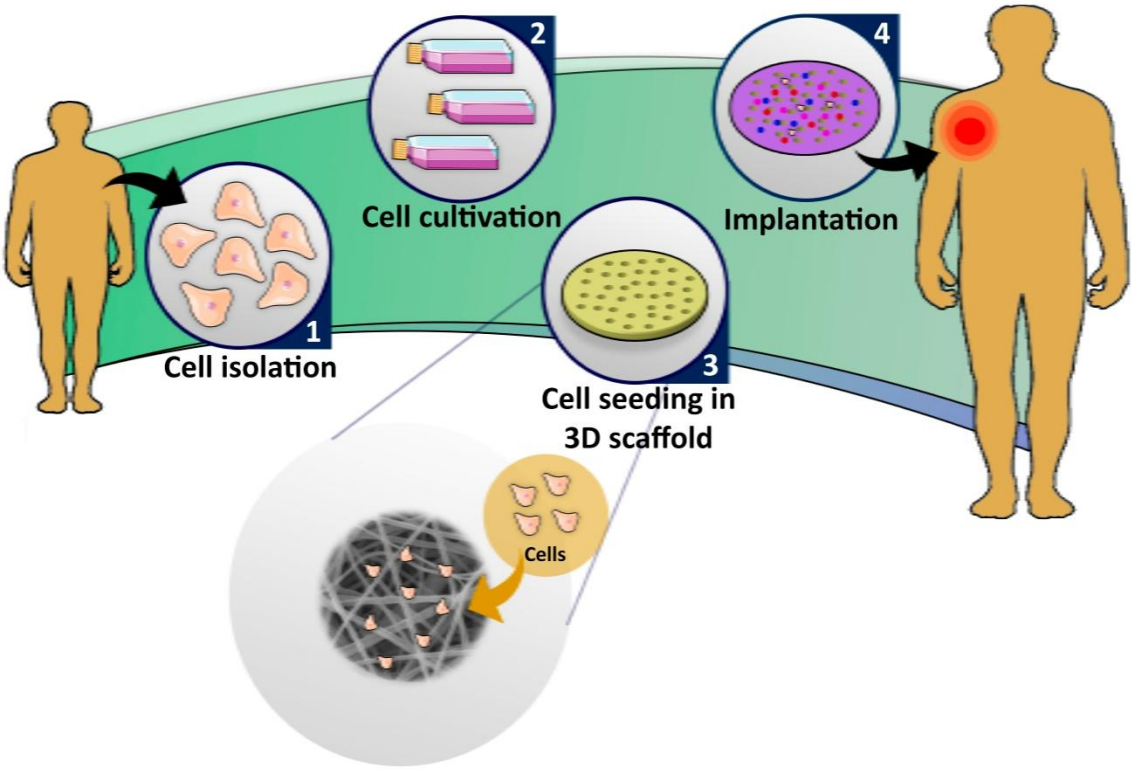

Figure 6. Representation of a tissue engineering strategy used to regenerate a functional tissue. Such therapeutic approach involves cell seeding in a porous scaffold. Cells are isolated from the patient (1) and expanded *in vitro* (2). Subsequently, cells are seeded in a scaffold (3). Ultimately, the construct is transplanted to the damaged tissue in order to restore its structure and function.

Skin tissue engineering revolutionized the therapy of extensive acute or chronic wounds. An ideal skin substitute has to fill certain requirements, such as biocompatibility, biodegradability, non-toxicity, and non-immunogenicity. It may also protect against bacterial infection, be nonadherent to the wound site, allow gaseous and fluid exchanges, absorb the excess exudates, and support the handling during application and regeneration of the new tissue. Furthermore, it should also be capable of improving the healing process, mimic the native skin environment, be comfortable and cost effective [2, 41].

Today, as a result of intense research, a myriad of skin substitutes exists and some of them are already available to be used in the clinic. Depending on wound severity, skin substitutes can be classified as epidermal, dermal and bilayered/dermo-epidermal substitutes (see table 1) [29]:

- **Epidermal Skin Substitutes**

Epidermal skin substitutes aim to restore the epidermis by promoting the reepithelialization of the wound. The majority of the epidermal skin substitutes are created by isolation of keratinocytes from the patient, followed by its subsequent *in vitro* cultivation on biocompatible substrates (e.g. bovine collagen, hyaluronic acid, etc.). When a suitable cell mass has grown, it is transferred to the wound bed for restoring the barrier function and enhancing the wound healing [42, 43]. In general, the available epidermal substitutes are expensive, difficult to handle due to their thin and fragile nature, cannot be used to treat full-thickness skin wounds and their production is time-consuming [44].

MySkin® is an example of an epidermal skin substitute that uses subconfluent autologous keratinocytes grown on a silicon support layer [29]. Contrariwise, Cryoskin® and Celaderm® are epidermal replacements containing allogeneic keratinocytes [45]. Suprathel® represents a reliable acellular epidermal skin substitute, based on polylactide, trimethylene carbonate and ε-caprolactone [45, 46].

- **Dermal Skin Substitutes**

Dermal skin substitutes are able to restore the injured dermis and are usually acellular. They display great structural integrity, prevent the wound from contracting and are able to mimic the basic properties of ECM [11]. However, they cannot efficiently replace the epidermal layer of the skin.

Alloderm®, Integra®, MatriDerm®, and Oasis® are examples of acellular dermal replacements. Integra® consists of a porous scaffold made of bovine collagen type I and shark chondroitin-6-sulphate glycosaminoglycan bonded to a silicone membrane. MatriDerm® is made up of bovine collagen and elastin hydrolysate. Cellular dermal substitutes, such as TransCyte® or Dermagraft®, use autologous dermal fibroblasts or neonatal human foreskin fibroblasts [42, 45].

- **Bilayered/ Dermo-Epidermal Skin Substitutes**

Bilayered/ Dermo-epidermal skin substitutes are the most advanced skin substitutes, which are conceived to mimic the histological structure of normal skin with both epidermal and dermal layers [29]. These bilayers provide biological stimulus for skin regeneration and at the same time act as temporary wound coverage. Keratinocytes and fibroblasts, either autologous or allogenic, are commonly used to prepare these bilayered structures [44]. Nevertheless, the bilayered skin substitutes that are available in the market are very expensive, present risk of infection to the patient and have low mechanical properties.

Apligraf® consists of viable allogeneic neonatal fibroblasts grown in a bovine collagen type I gel matrix combined with a layer of viable allogeneic neonatal keratinocytes [47]. OrCell® is a tissue

engineered skin construct that includes fibroblasts seeded into a bovine type I collagen sponge, on top of which keratinocytes are seeded to form a confluent layer [42]. Additionally, Mediskin® is an example of an acellular dermo-epidermal skin substitute that is based on porcine xenografts [48].

Although some of the different skin substitutes are very complex and effective, they are not able to completely mimic the skin's natural environment. Therefore, further studies are needed to improve these products.

Table 1. Skin substitutes available in the market.

		Company	Application	Cells	Biomaterials
Epidermal	**Celaderm®**	Advanced BioHealing, Inc., Connecticut, USA	Chronic wounds	Frozen cultured allogeneic keratinocytes	-
	Cryoskin®	Cryo Diffusion, Lery, France	Chronic wounds	Allogenic keratinocytes from newborn foreskin	Silicon backing matrix
	Myskin®	CellTran Ltd, Sheffield, UK	Diabetic foot; venous leg ulcers; burns	Cultured autologous human keratinocytes	Polyacrylic acid membrane
	Suprathel®	Stapleline GmbH, Bochum, Germany	Acute superficial partial-thickness injuries	-	Copolymer of polylactide and ε-caprolactone
Dermal	**Alloderm®**	LifeCell Corporation, New Jersey, USA	Full- and partial-thickness wounds	-	Human acellular lyophilized dermis
	Integra®	Integra Life Sciences, Inc., New Jersey, USA	Full- and partial-thickness wounds	-	Bovine collagen I; glycosaminoglycan matrix
	Matriderm®	Medskin Solutions, Billerbeck, Germany	Full- and partial-thickness wounds	-	Bovine non-crosslinked lyophilized dermis, coated with α-elastin hydrolysate
	Oasis®	Cook Biotech Inc., Indiana, USA	Full- and partial-thickness wounds	-	Acellular porcine small intestine submucosa matrix
	Transcyte®	Advanced BioHealing, Inc., Connecticut, USA	Full-thickness burns	Neonatal foreskin allogeneic fibroblasts	Nylon mesh covered with silicone
	Dermagraft®	Advanced BioHealing, Inc., Connecticut, USA	Full-thickness burns	Neonatal foreskin allogeneic fibroblasts	Polyglactin scaffold
Dermo-Epidermal	**Apligraf®**	Organogenesis, Inc., California, USA	Chronic wounds	Allogenic keratinocytes; fibroblasts	Bovine collagen
	OrCel®	Ortec Internation, Inc., New York, USA	Chronic wounds	Allogenic keratinocytes; fibroblasts	Bovine Collagen
	Mediskin®	Brennen Medical, Minnesota, USA	Acute and chronic wounds	-	Frozen porcine xenograft chemically crosslinked

1.3. Nanofibrous membranes produced by electrospinning

Electrospinning is a technology that uses electrostatic forces to produce polymeric nanofibrous meshes with diameters ranging from 2 nm to several micrometers [49]. Electrospinning was for the first time described in literature more than a century ago, in 1902, when Cooley and Morton separately patented methods and apparatuses for electrically dispersing fluids. However, only recently electrospun polymeric nanofibers became a topic of huge research [50].

A conventional electrospinning setup (figure 7) is composed of a syringe pump, a capillary needle connected to a syringe, a high-voltage power supply, and a metal collector. In this technique two electrodes are used - one is connected to the needle and the other is fixed to the collector - in order to complete a circuit that produces an electric field. The syringe pump is used to force the solution to pass through the needle with a controlled flow rate. When a high voltage is applied at the tip of the capillary needle, the polymeric solution remains at the tip of the needle due to surface tension. With the increasing of the intensity of the electrical field, the charge causes the elongation of the droplet into a cone, known as the Taylor Cone. An additional increase in the electric field will generate a critical value with which the repulsive electrostatic forces overcome the surface tension and a polymer jet is ejected from the tip of the Taylor Cone. Before reaching the collector, the jet undergoes a series of electrically driven instabilities and gradually thins in the air due to solvent evaporation [50, 51]. If the jet is collected in a stationary collect, as shown in figure 8, non-woven meshes composed of randomly oriented nanofibers are obtained. However, aligned nanofibers can also be produced by this technique using rotary collectors [52].

The production of electrospun meshes is dependent on specific parameters such as the precursor solution (e.g. conductivity, surface tension, viscosity and solvent selection), processing variables, and environmental conditions. The control of these particular features has a direct impact on the mean diameter and arrangement of the accumulated fibers. Particularly, solutions with high viscosity lead to the production of fibers with a high diameter, while an increase in the surface tension or conductivity of the polymer solution results in a decrease in nanofiber diameter. Furthermore, an increase in voltage or a decrease in feed rate results in a reduction of the fiber diameter. However, a high electrical potential is not desired since it may lead to the formation of beads or to the formation of defective nanofibers. Moreover, the distance between the needle and the collector needs to be sufficient to allow solvent evaporation but close enough to allow production of fibers with the required morphology. Regarding the environmental parameters, an increase in temperature is responsible for decreasing the average fiber diameter, due to a decrease in solution viscosity, while an increase in humidity increases the average fiber diameter due to polymer swelling [32, 50].

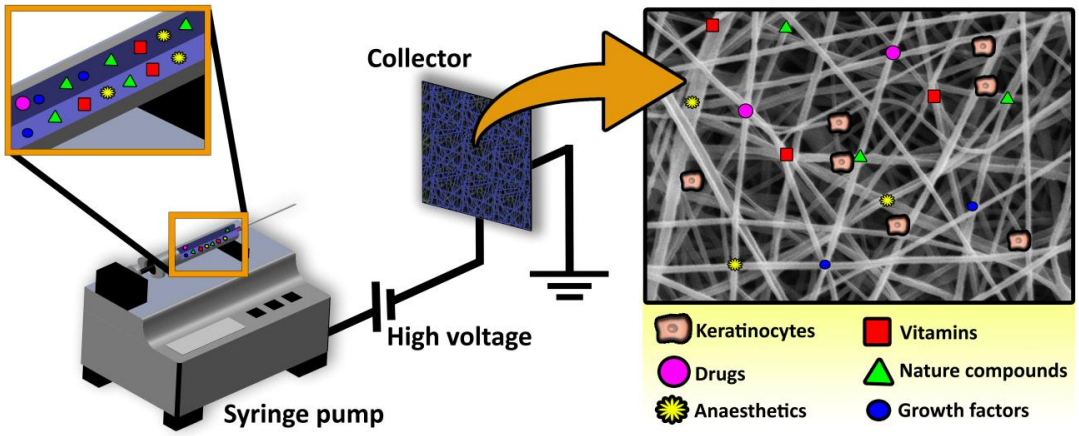

Figure 7. Representation of a conventional electrospinning apparatus that is used to produce non-woven meshes composed of randomly oriented nanofibers. Bioactive molecules that may enhance the wound healing process have been incorporated in electrospun meshes.

In the last years, electrospun nanofibrous membranes become one of the most studied platforms for skin tissue engineering applications. According to Augustine and Abrigo, the main advantages of the electrospun membranes to be used as skin substitutes are [52, 53].

- **Mimic the ECM**

The nanofibers produced by electrospinning have diameters ranging from 50-500 nm, which is within the diameter range presented by the collagen fibrils found in the natural ECM. The structural similarity is very important in cell adhesion, proliferation, migration, and differentiation.

- **Exudate uptake capacity**

The high surface area presented by electrospun nanofibrous meshes allows them to absorb the wound exudates. The great absorptive properties of this type of skin substitute help in the maintenance of a moist environment at the wound site.

- **Semi-permeable**

The porous structure of electrospun meshes allows gas exchange and confers protection against bacteria invasion.

- **Conformability**

Conformability of the material is a crucial issue when materials are aimed for skin tissue engineering. Electrospun nanofibrous membranes are easy to fit in a wound with irregular architecture, thus providing a great conformability.

- **Functionality**

The nanofibers produced by electrospinning can be easily functionalized with bioactive compounds in order to improve skin regeneration. Depending on the stage of treatment and the intended functionality, drug molecules (e.g. antiseptics, antifungal, and vasodilators), genes, antimicrobial agents, growth factors (e.g. FGF, EGF, and TGF) and even cells (e.g. fibroblasts and keratinocytes) can be delivered to the wound, in a controlled manner, for improving the wound healing process. Blend, coaxial and emulsion electrospinning are strategies employed to fabricate biofunctional nanofibrous scaffolds (figure 7). To produce blended electrospun meshes, active agents are mixed with the polymeric solution before performing the electrospinning process [54]. In coaxial electrospinning, a syringe containing a core and an outer compartment is used. Through this technique, the active agents are incorporated in the core and the polymeric solution in the outer compartment. Subsequently, both polymer and active agent are coaxially and simultaneously electrospun to produce fibers with a core-shell structure [32]. Another route to obtain core-shell nanofibers is by performing emulsion electrospinning, which is a technique that does not require a particular needle setup. In this type of electrospinning, an aqueous solution, with active agents is emulsified into an organic phase containing a polymer that forms the shell [55].

1.3.1. Electrospun nanofibrous membranes produced with natural polymers

Natural polymers are usually biocompatible and present low immunogenicity. Moreover, natural polymers have an inherent capacity to promote cell adhesion since they have specific aminoacids sequences, such as RGD (arginine/glycine/aspartic acid). Cellulose acetate, chitosan, collagen, elastin, gelatin, hyaluronic acid, silk fibroin, and zein are examples of natural polymers successfully electrospun and applied for skin regenerative purposes. The main drawback of natural polymers is associated to its poor mechanical properties [54]. In the following sections, some of the natural polymers are described in further detail.

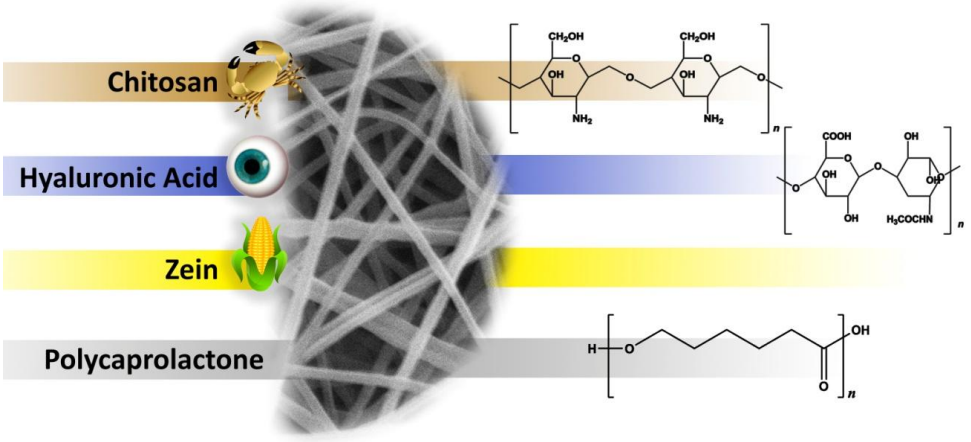

Figure 8. Chemical structure of some examples of natural and synthetic polymers used in skin tissue engineering.

1.3.1.1. Chitosan

Chitosan (CS) is obtained from chitin, which is the second most abundant polysaccharide found in nature. This polymer is usually obtained from the shells of crustaceans, the exoskeleton of insects and cell walls of fungi [54]. CS polysaccharide is composed of glucosamine and N-acetyl-glucosamine [56]. CS has many advantages like biocompatibility, biodegradability, antimicrobial and hemostatic activity. Moreover, CS can stimulate collagen synthesis, a feature that is fundamental for enhancing the wound healing [2].

CS is easily incorporated into films, gels, or sponges, but very hard to electrospun in its pure form since it forms highly viscous solutions. Hence, this polymer is usually modified or combined with other polymers in order to be electrospun. Zhou et al produced the first CS-based electrospun membranes aimed for skin regeneration. Their electrospun membranes were produced with water soluble CS and poly(vinyl alcohol) that promoted the adhesion and proliferation of mouse fibroblast cells [57]. The antimicrobial properties of CS are also reported in the literature by several authors. Cai et al produced CS/silk fibroin electrospun membranes that inhibit the growth of the Gram-negative bacteria *Escherichia Coli* (*E.Coli*) [58]. Antunes and collaborators produced a deacetylated/arginine-modified chitosan electrospun membrane with enhanced bactericidal activity against both gram-positive *Staphylococcus Aureus* (*S. Aureus*) and gram-negative *E.Coli* [59].

1.3.1.2. Hyaluronic Acid

Hyaluronic acid (HA), also known as hyaluronan or hyaluronate, is a linear polysaccharide composed of repeating units of glucuronic acid and N-acetylglucosamine that is found in the ECM of connective tissues [60]. It can be obtained from bacteria or from the enzymatic digestion of connective tissues [56]. HA has excellent biocompatibility and biodegradability. Furthermore, as a natural polysaccharide present in the skin ECM, HA presents a high water retention capacity, and as a component of granulation tissue, it facilitates the migration of inflammatory cells and fibroblasts into the healing wounds through the interaction with CD44 receptors present in the plasma membrane [54].

The application of HA electrospun meshes in the wound healing process has been limited by its high viscosity and surface tension [61]. Hsu and colleagues produced HA/collagen electrospun membranes cultured with foreskin fibroblast cells. In their study, they verified that HA promotes a scarless wound healing since it decreases the ratio of tissue inhibitor of metallopeptidase 1 (TIMP1) to matrix metalloproteinase-1 (MMP1) characteristic of scarless wounds [62]. Later on, HA/ Polycaprolactone (PCL) /Silk fibroin electrospun membranes were produced to be used in skin tissue engineering. The addition of HA gave hydrophilic properties to the membranes, which caused the suppression of non-specific protein adsorption, leading to a reduction of fibrosis thickness and macrophages adhesion *in vivo*. Further, this study showed that HA-based membranes present a significant increase in fibroblasts proliferation and adhesion. These findings suggested that HA-based electrospun membranes are excellent candidates to be used as wound

dressings [63]. Recently, HA electrospun meshes were used as growth factors delivery systems in order to promote wound healing [64, 65]. A recent study reported the efficient encapsulation of EGF in HA/PCL electrospun membranes [64]. Moreover, Lai and collaborators developed an HA/collagen electrospun membrane capable of performing a controlled release of several angiogenic growth factors, such as PDGF, VEGF, bFGF, and EGF, either directly embedded in the nanofibers or encapsulate in gelatin nanoparticles according to the wound healing stage required. Moreover, this study also showed that the produced membranes possess mechanical properties similar to those of human native skin [65].

1.3.1.3. Zein

Zein (ZN) is a protein found in corn or maize. It is mainly composed of nonessential amino acids such as glutamic acid (21–26%), leucine (20%), alanine (10%) and proline (10%). ZN is biodegradable, biocompatible, moderately hydrophobic, highly elastic and easily electrospinable [66, 67].

The study of ZN nanofibers for biomedical applications began in 2009. Yao and co-workers reported the production of electrospun blends composed of ZN/silk fibroin with improved mechanical properties and biocompatibility [68]. In 2013, ZN nanofibers were used as drug delivery system for wound healing applications. Huang et al. produced ZN nanofibers loaded with Ibuprofen through coaxial electrospinning technique. The i*n vitro* release experiments showed that the drug-loaded fibers provided sustained drug release for 10 hours [69]. Another study reported the production of ZN/polyurethane/cellulose acetate electrospun membranes blended with an antimicrobial agent, streptomycin sulfate. These electrospun membranes presented features, such as hydrophilicity, excellent cell adhesion capacity, and blood clotting activity [70]. Moreover, ZN/silver nanoparticles electrospun membranes were also produced for being applied as wound dressings by Dashdorj and collaborators. The results obtained demonstrated that membranes had a good cytocompatibility and fibroblasts were able to adhere on the composite nanofibers and also displayed bactericidal activity against *S.aureus* and *E.coli* [71].

1.3.2. Electrospun nanofibrous membranes produced with synthetic polymers

Synthetic polymers are often characterized by having improved mechanical properties (viscoelasticity and strength), and slow degradation rates. Typical synthetic polymers used in biomedical applications are hydrophobic biodegradable polyesters, such as polyglycolide, polylactide, polyurethane, and PCL, which were already used as nanofibrous scaffolds [54]. In the following section, the use of PCL to produce electrospun mats for wound healing purposes is reviewed in further detail.

1.3.2.1. Polycaprolactone

PCL is an aliphatic linear polyester, synthesized through ring-opening polymerization of ε-caprolactone. It is characterized by being biocompatible, bioresorbable, inexpensive and degrades through the hydrolysis of its ester linkages under physiological conditions. Therefore, it has been used as a valuable material for tissue engineering applications. However, the use of PCL in tissue engineering is compromised by its hydrophobic nature that limits cell adhesion and leads to uncontrolled biological interaction [72].

In order to overcome such drawbacks, PCL has been blended with other polymers such as chitosan or gelatin. Duan et al investigated the feasibility of using gelatin/PCL electrospun membranes to produce an epidermal skin substitute. These membranes showed good mechanical and biological properties that are compatible with their use in epidermis regeneration [73]. Bonvallet and co-workers synthesized PCL/collagen electrospun membranes with micropores to be used as dermal skin substitutes. These nanofibers accelerated the wound closure and stimulated the regeneration of healthy dermal tissue [74]. Another study, performed by Augustine and colleagues, reports the development of a PCL electrospun membrane loaded with zinc oxide (ZnO) nanoparticles. This was the first study that evaluated the ability of biomaterials containing ZnO nanoparticles to enhance the mammalian cell proliferation. The authors noticed that fibroblasts adhered and proliferated when seeded on top of these membranes, a process that is crucial for enhancing the wound healing process [53].

1.4. Antimicrobial Agents

Bacterial infections are regarded as the most severe and devastating complications associated with the implantation of biomaterials in the human body [75]. Nowadays, it is estimated that 65-80% of bacterial infections are caused by organisms that form biofilms on implants surface, compromising their successful application [76]. In this context, the development of biomaterials with antimicrobial activity is fundamental to avoid infections related to materials implantation.

So far, different approaches have already been used to confer antimicrobial properties to tissue engineering constructs. Some authors reported the prevention of bacterial adhesion via through modification of surface charges or incorporation of adhesion-resistant coatings (e.g. polymer brushes or diamond-like carbon coatings) [59, 77-80]. Other antimicrobial strategies include the release of antimicrobial agents (e.g. antibiotics, drugs, metallic nanoparticles, nitric oxide or quaternary ammonium compounds) to the surrounding areas in order to avoid contaminations by bacteria [81-84].

However, the commonly used antimicrobial agents display cytotoxicity and induce microbial resistance [85]. Therefore, there is a huge demand to develop of new and effective antibacterial tissue engineering constructs that do not trigger any adverse effect on the host.

1.4.1. Salicylic Acid

Salicylic Acid (SA) is a phenolic compound produced by plants (e.g. Nicotiana tabacum, *Cucumis sativus*, and *Arabidopsis thaliana)* that plays an important role in several physiological processes, such as the induction of plant defense responses against pathogen attacks. Furthermore, it is also an antiseptic agent of *Aloe vera* as well as the active component of aspirin [86-88]. SA owns anti-inflammatory, analgesic, antipyretic, and antimicrobial properties that are crucial for the promotion the wound healing process [89]. Moreover, SA is biocompatible and do not exhibit any microbial resistance. Despite these interesting properties, it has found limited application in the area of tissue engineering. Griffin and collaborators developed one of the few studies where SA was used for tissue engineering applications. These authors have produced SA-derived poly(anhydride-ester) electrospun fibers for the regeneration of the peripheral nervous system. These authors verified that SA-based poly anhydride fibers can promote not only nerve regeneration but also the regeneration of other tissues [90].

1.5. Aims

The overall aim of the present thesis was to design, develop and characterize a new electrospun bilayer membrane (EBM) to be used as a skin substitute. The upper layer of the EBM was conceived to provide structural integrity to the final construct and the bottom layer was designed to stimulate the healing process and also display antibacterial and anti-inflammatory activity.

The specific aims of this study were:

- Optimize and produce the EBM;
- Evaluate and characterize the physicochemical properties of the EBM;
- Evaluate and characterize the biological properties of the produced EBM;
- Evaluate and characterize the antimicrobial properties of the produced EBM.

🛠 Chapter II – Materials and Methods

2. Materials and Methods

2.1. Materials

3,3,3 Trifluoroethanol (TFE), HA 95% (MW=1.5 to 2.2 million Da), SA and ZN were purchased from Acros Organics (New Jersey, USA). 3-(4,5-dimethylthiazol-2-yl)-2,5-diphenyltetrazolium bromide (MTT) was purchased from Alfa Aesar (Ward Hill, USA). Fetal bovine serum (FBS) (free from any antibiotic) was acquired from Biochrom AG (Berlin, Germany). Glacial acetic acid was obtained from LabChem (New York, USA). Paraformaldehyde (PFA) was obtained from Merck, SA (Algés, Portugal). Normal Human Dermal Fibroblasts (NHDF) cells were purchased from PromoCell (Labclinics, S.A., Barcelona, Spain). Amphotericin B, CS (low molecular weight (LMW), Dimethylformamide (DMF), Dulbecco's modified Eagle's medium (DMEM-F12), Ethylenediaminetetraacetic acid (EDTA), Gentamicin, Kanamycin, LB Broth, Phosphate-buffered saline solution (PBS), PCL, Sodium hydroxide (NaOH) and Trypsin were purchased from Sigma-Aldrich (Sintra, Portugal). Dimethyl sulfoxide (DMSO) was obtained from Thermo Fisher Scientific (Rockford, IL,USA).

2.2. Methods

2.2.1. Deacetylation of Chitosan

CS was purified and deacetylated through a method previously described by Miguel and colleagues [91]. Briefly, 500 mg of CS LMW were dispersed in 10mL of NaOH (1M) solution, under magnetic stirring for 4 h, at 50 ^{o}C. Then, the mixture was filtered using a Whatman® quantitative filter grade 541:0.22 µm (Sigma-Aldrich) and a Buchner funnel to recover the deacetylated CS. The remaining material was washed extensively until the sample pH reached 7.4. Subsequently, the samples were dried at 40 ^{o}C overnight. The degree of deacetylation (DD) was determined by using the first derivative UV-spectroscopy (1DUVS) method [92]. UV–vis chitosan spectra were obtained using a Thermo Scientific Evolution 201 UV–vis spectrophotometer.

2.2.2. Production of the electrospun bilayer membrane

To produce the EBM, two distinct polymeric solutions were electrospun using a conventional electrospinning apparatus. The system setup was comprised of a high voltage source (Spellman CZE1000R, 0–30 kV), a precision syringe pump (KDS-100), a plastic syringe with a stainless steel needle (21 Gauge) and an aluminum disk connected to a copper collector. In order to produce the bottom layer of the electrospun mesh, 40% ZN (w/v) and 7% CS (w/v) were dissolved in 80% ethanol (EtOH) (w/v) and 70% AA (w/v), respectively. The final mixture (9:1 w/w ratio) was then homogenized with an X10/25 Ultra-turrax®, during 15 min. Finally, SA 8% (w/v) was added to the

mixture. To produce the top layer of the electrospun mesh, 7% PCL (w/v) was dissolved under stirring in 80% TFE (w/v) at 60ºC and 1% HA (w/v) was dissolved in 4:1 NaOH (5M)/DMF (w/v). After the complete dissolution of both polymers, a 1:9 HA/PCL (w/w) final ratio was prepared for the following step.

Then, 10 mL of the CS_ZN_SA solution were placed in the syringe and electrospun using a constant flow rate of 3.0 mL/h, a working distance of 15 cm and an applied voltage of 28 kV (see figure 9A for further details). After the first layer be produced, 10 mL of the HA_PCL polymeric solution were electrospun on CS_ZN_SA surface at a constant flow rate of 2.5 mL/h, using a working distance of 15 cm and an applied voltage of 25 kV (figure 9B). The produced EBM was used to perform different *in vitro* assays in order to evaluate its applicability as a wound dressing (figure 9C).

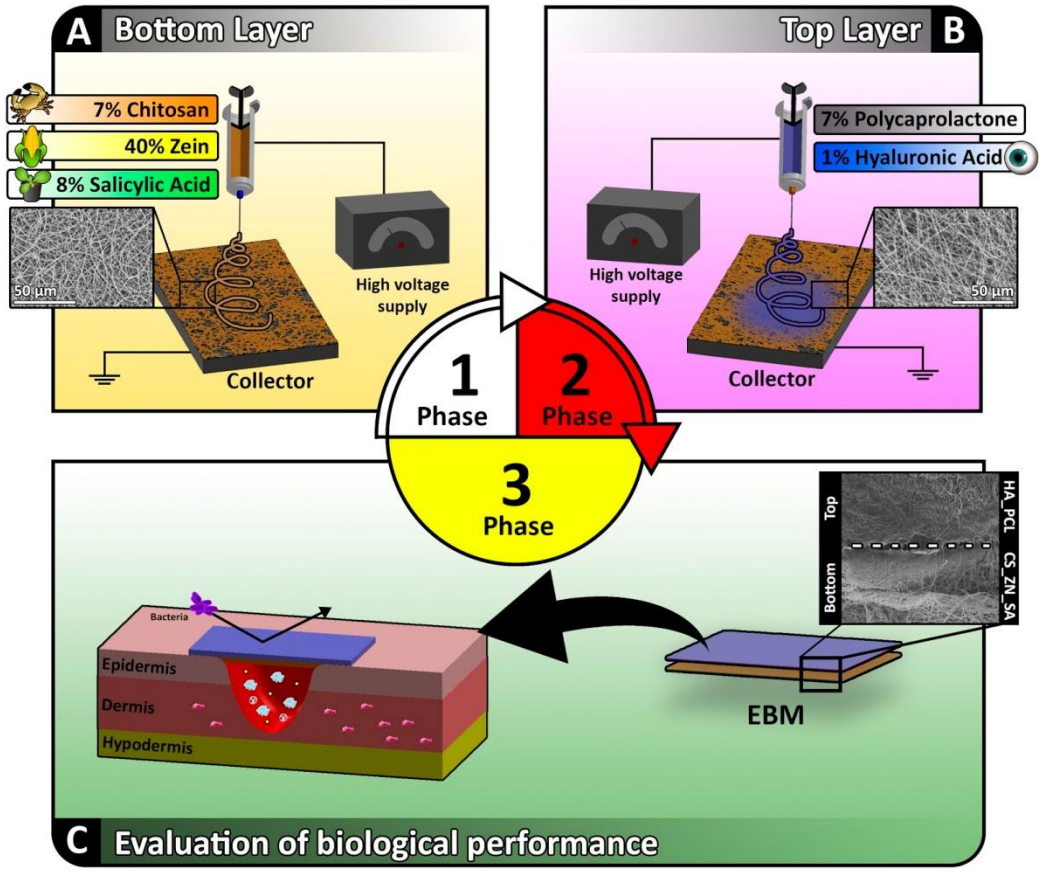

Figure 9. Schematic representation of the experimental setup used to produce the EBM. The bottom layer was produced by loading a syringe with a CS_ZN_SA solution and then electrospun (A); After the HA_PCL polymeric solution was electrospun towards the CS_ZN_SA mesh to produce the EBM (B). Finally, the properties of the produced EBM were studied in order to evaluate its suitability to be used as a wound dressing (C).

2.2.3. Attenuated Total Reflectance-Fourier Transform Infrared Spectroscopy analysis

To characterize the composition of the produced EBM, ATR-FTIR analysis was performed. The spectra were acquired for the different samples using an average of 128 scans, between 400 and 4000 cm^{-1}, with a spectral resolution of 4 cm^{-1}. All the samples were mounted on a diamond window, and the spectra were recorded using a Nicolet iS10 FTIR spectrophotometer (Thermo Scientific, Waltham, MA, USA). In order to compare the spectra of individual components with those of the produced membranes, all the raw components used for nanofibrous mesh production were analyzed.

2.2.4. Characterization of the mechanical properties of EBM

The tensile properties of EBM were determined using a Shimadzu AG-X Tensile Testing Machine (Tokyo, Japan) at room temperature (RT), as described elsewhere [93]. This assay was performed accordingly to the guidelines established by ASTM standard D3039/ D3039 M (Standard Test Method For Tensile Properties of Polymer Matrix Composite Materials). The samples (n=5) had a width of 2 cm, a length of 6 cm and a thickness ranging from 0.41 to 0.52 mm. The length between the clamps was set to 2 cm and the speed of testing set to 2 mm/min. Load-extension data were recorded and the stress–strain curve of the EBM was constructed by applying the equations (1) and (2), respectively:

$$\text{Stress} = \sigma = \frac{\text{F}}{\text{A}} \qquad (1)$$

$$\text{Strain} = \varepsilon = \frac{\Delta \text{l}}{\text{L}} \qquad (2)$$

Where *F* is the applied force; *A* is the cross-sectional area; Δl is the change in length, and *L* is the length between the clamps.

2.2.5. Evaluation of the porosity of EBM

The microporosity of the EBM was determined by using a liquid displacement method adapted from Antunes and collaborators [59]. Briefly, 3 specimens were weighed and then, immersed in absolute EtOH for 1 h and then reweighed. Finally, the membrane porosity was calculated by determining the amount of EtOH absorbed, through equation (3):

$$\text{Porosity}\ (\%) = \frac{W_w - W_d}{D_{ethanol} * V_{membrane}} * 100 \qquad (3)$$

Where W_w and W_d are the wet and dry weights of the membrane, respectively. $D_{ethanol}$ represents the density of EtOH at RT and $V_{membrane}$ is the volume of the wet membrane.

2.2.6. Determination of contact angle at the surface of EBM

The contact angles at the surface of EBM were determined using a Data Physics Contact Angle System OCAH 200 apparatus, operating in static mode, at RT. For each sample, water drops were placed on the top and bottom layers of the EBM. The reported contact angles are the average of at least three independent measurements.

2.2.7 Water vapor transmission rate (WVTR)

The water vapor diffusion through the EBM was evaluated as described elsewhere [59]. Briefly, the EBM samples were used to seal the opening of a glass test tube (1.77 cm^2) containing 10 mL of ultrapure water, parafilm tape was used to attach the membrane and avoid water losses. Afterward, the membranes were incubated at 37 °C. Non-sealed tubes were used as a control. At specific time points, water evaporation was obtained by determining the weight loss. The water vapor transmission rate (WVTR) was calculated through equation (4):

$$\text{Water vapor transmission} = \frac{W_{loss}}{A} \qquad (4)$$

Where W_{loss} is the daily weight loss of water and A is the area of the tube opening.

2.2.8. Characterization of EBM biodegradation profile

The *in vitro* degradation of EBM and of their individual layers (CS_ZN_SA and HA_PCL) was monitored by immersing the samples in PBS (pH 5.50), under stirring (40 rpm), at 37 °C. The samples were then removed from the solutions and weighed at 1, 3 and 7 days after being completely dried. The degradation percentage at each time point was calculated according to equation (5):

$$\text{Weight loss } (\%) = \frac{W_i - W_t}{W_i} * 10 \qquad (5)$$

Where W_i corresponds to the initial weight of the sample and W_t to the weight of the sample at time t.

2.2.9. Characterization of the release profile of SA

SA release from EBM was evaluated as formerly reported by Ouimet and collaborators [94]. EBM samples were immersed in 20 mL glass scintillation vials containing 10 mL of PBS, at pH 5.50. The vials were then stored at 37 °C with agitation (40 rpm) in an incubator shaker, in order to mimic the physiological conditions. A 5 mL aliquot of the media was removed and replaced by an equal volume of fresh PBS, every 24 h, to ensure sink conditions. The amount of SA released was determined at 303 nm using a Thermo Scientific Evolution 201 UV–vis spectrophotometer. A calibration curve of the standard SA solutions in PBS was performed to determine the exact amount of SA released from EBM. All sets of experiments were performed in triplicate.

2.2.10. Characterization of the biological properties of EBM

2.2.10.1. Evaluation of cell viability and proliferation in the presence of EBM

NHDF were cultured in DMEM-F12, supplemented with 10% heat-inactivated FBS, amphotericin B (100 µg/mL) and gentamicin (100 µg/mL) in 75 cm^2 culture T-flasks. Cells were maintained in a humidified atmosphere at 37 °C, with 5% CO_2, until confluence was attained. Subsequently, cells were trypsinized with 0.18% trypsin (1:250) and 5 mM EDTA and then centrifuged during 5 min. Prior to cell seeding, membranes were placed into 96-well plates and then sterilized by UV irradiation for 1 h. Following, cells were seeded at a density of $10x10^3$ cells per well, in order to evaluate cell adhesion and proliferation in the presence of EBM. The culture medium was changed every two days until the end of the assay.

The cytotoxic profile of HA_PCL, CS_ZN_SA individual membranes and EBM was characterized using an MTT assay that was performed according to the guidelines set for ISO10993-5 standard. Briefly, the culture medium was removed and 50 µL of MTT (5 mg/mL PBS) were added to each sample, followed by their incubation for 4 h, at 37 °C, in a 5% CO_2 atmosphere. Then, cells were treated with 200 µL of DMSO (0.04 N) for 30 min. A microplate reader (Biorad xMark microplate spectrophotometer) was used to read the absorbance at 570 nm for each well. Five replicates of each sample were used. Cells cultured without materials were used as a negative control (K^-), whereas cells cultured with EtOH (90%) were used as positive control (K^+).

2.2.10.2. Confocal microscopic analysis

Confocal laser scanning microscopy (CLSM) was used to characterize the cell distribution on both layers of the EBM. Cells ($10x10^3$ cells/mL) were seeded in µ-Slide 8 well Ibidi imaging plates (Ibidi GmbH, Germany) on the bottom and top layers of EBM. Cells seeded on the surface of the Ibidi imaging plate were used as a control group. After 24h, cells were fixed with 4% PFA in PBS for 20 min and then stained with the WGA-Alexa 594® conjugate. Cells were then rinsed several times with PBS and labeled with Hoechst 33342® nuclear probe (2 µM). The 3D reconstruction and image analysis were performed using Zeiss Zen 2010 software.

2.2.10.3. Evaluation of the antimicrobial properties of EBM

S. Aureus, a gram-positive bacterium obtained from the clinic, was used to study the bactericidal activity of the HA_PCL, CS_ZN_SA, and EBM. A modified Kirby-Bauer technique was used to perform this antimicrobial assay [95]. Briefly, 200 µl of bacteria medium (with a concentration of 1×10^8 colony forming units (CFU)/mL of *S. Aureus*) were dispensed onto an agar plate. Then, circular membranes (n=3) were placed on the agar plate and incubated during 24h, at 37 °C. After that, the inhibitory halos around the samples were photographed and their diameter measured using ImageJ software.

2.2.11. Characterization of the morphology and biological performance of the EBM by SEM analysis

SEM analysis was performed to characterize the EBM morphology, cellular attachment and biofilm formation on its surface. Samples that contain cells or bacteria were fixed for 4 h with 2.5% (v/v) glutaraldehyde. After, samples were washed three times with PBS and dehydrated with growing concentrations of EtOH (50, 60, 70, 80, 90 and 99.9%). Subsequently, scaffolds were frozen using liquid nitrogen and freeze-dried for 3h. Finally, all samples were mounted onto aluminum stubs with Araldite glue and sputter-coated with gold using a Quorum Q150R ES sputter coater. SEM images were then acquired with different magnifications, at an acceleration voltage of 20kV, using a Hitachi S-3400N Scanning Electron Microscope.

2.2.12. Statistical Analysis

The statistical analysis of the obtained results was performed using one-way analysis of variance (ANOVA), with the Newman-Keuls post hoc test. A p value lower than 0.05 ($p<0.05$) was considered statistically significant.

Chapter III - Results and Discussion

3. Results and discussion

3.1. Deacetylation of Chitosan

The deacetylated CS used for EBM production had a DD of 98.36% ± 0.22 (table 2), which indicates that almost all of the primary amine groups of the CS polymer chain were positively charged. It is known that when CS with a high DD is used to produce 3D constructs, they have improved strength, antimicrobial properties and also enhance cellular attachment and proliferation [96, 97].

Table 2. Degree of deacetylation of the different CS samples measured by 1DUVS (mean ± SD, n = 3).

Sample	Nominal DD* (%)	Determined DD** (%)
Commercial CS	75 - 85	82.41 ± 0.17
Modified CS	-	98.36 ± 0.22

* Provided by the manufacturer

** Determined by 1DUVS.

3.2. Morphological characterization of the scaffolds

The electrospinning technique was used to produce a new bilayered nanofibrous dressing, where each layer plays different roles in the promotion of the wound healing process. The top layer (HA_PCL) was conceived to endow the system with the suitable physical and mechanical properties, whereas the bottom layer (CS_ZN_SA) was designed to assure cell adhesion and proliferation as well as antimicrobial and anti-inflammatory properties to the final EBM. Figure 10 shows the macroscopic images of the top and bottom view of EBM, where both layers present an opaque appearance and a uniform structure. Additionally, HA_PCL layer shows a white color which is in accordance with previously published studies [98]. On the other hand, the CS_ZN_SA electrospun layer presents a light yellow color due to the xanthophyll pigments present in corn that bound to ZN protein fraction through hydrophobic interactions [99, 100].

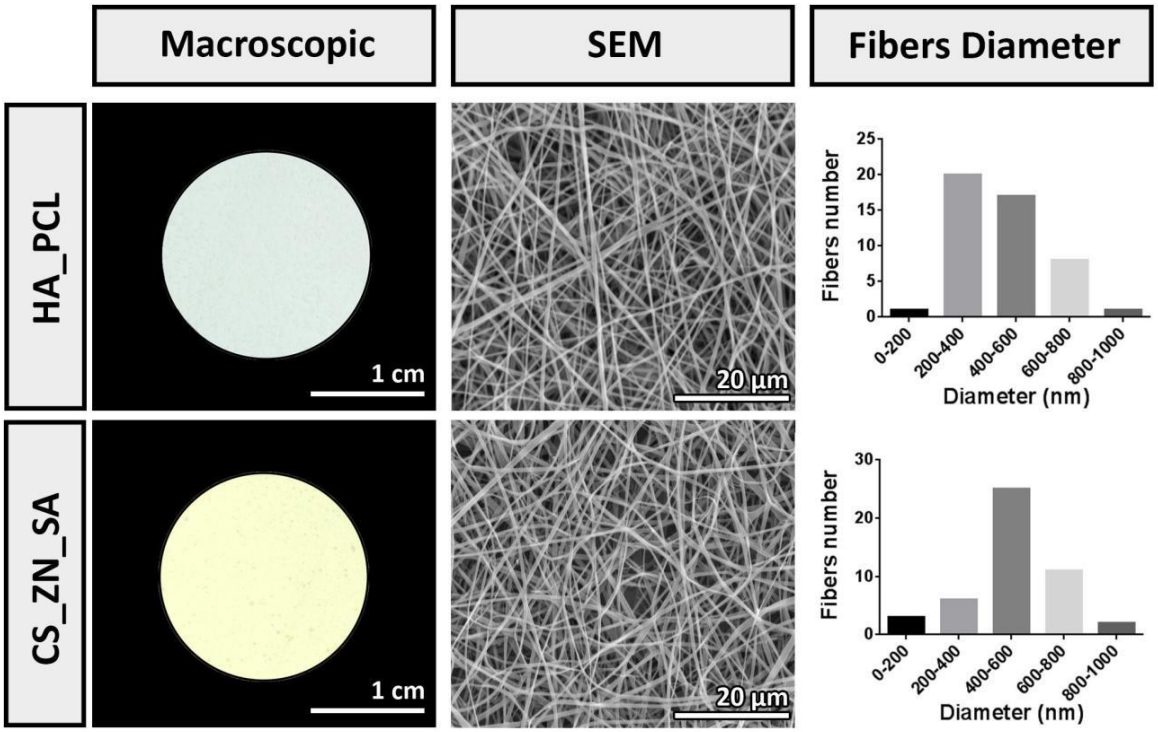

Figure 10. Characterization of the morphology of the two layers of EBM; SEM images of top (HA_PCL) and bottom (CS_ZN_SA) electrospun meshes are presented as well as the fiber diameters distribution.

Furthermore, the morphology of electrospun nanofibers was also analyzed by SEM. Figure 10 shows that both HA_PCL and CS_ZN_SA layers presented a highly porous 3D nanofiber network composed of randomly oriented fibers with diameters of 472 ± 192 nm and 530 ± 180 nm for HA_PCL and CS_ZN_SA electrospun layers, respectively. It is noteworthy that the diameters of the produced nanofibers are within the range displayed by collagen fibrils found in natural ECM since their size varies between 50 and 500 nm [95]. Therefore, these results suggest that the produced EBM mimic some of the structural features of the ECM, providing an optimal microenvironment for cell recruiting/seeding, adhesion, proliferation, differentiation, and ultimately improve new skin tissue formation [101].

Moreover, SEM images were also acquired by performing cryofracture of EBM. Through the analysis of figure 11, it is possible to observe that both layers form an almost continuous arrangement from the bottom to the top of the EBM. Moreover, the connection between the two layers can be explained by the presence of polymers with opposite charges in both layers. Indeed, HA present in HA_PCL electrospun layer possesses glucuronic acid residues that contain carboxyl groups that confer a negative charge to this membrane layer [102]. On the other hand, deacetylated CS present in CS_ZN_SA layer contains amine groups positively charged [103]. Consequently, an electrostatic interaction between HA and CS may be responsible for the interconnection established between the two layers.

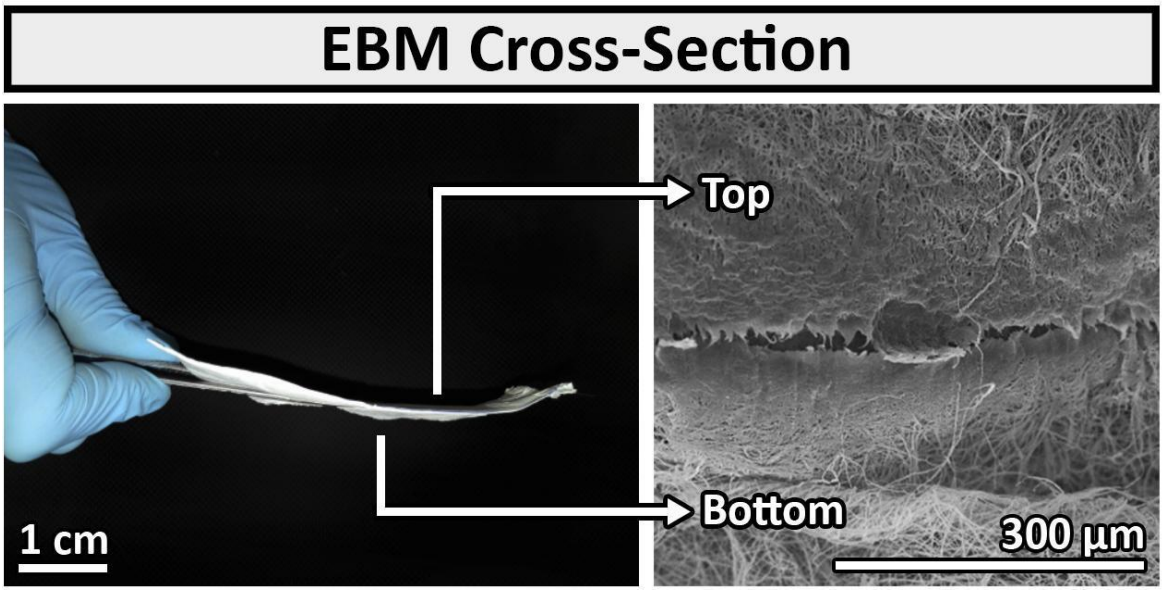

Figure 11. Macroscopic and SEM cross-section images of the EBM.

3.3. Attenuated Total Reflectance-Fourier Transform Infrared Spectroscopy analysis

Figure 12 shows the ATR-FTIR spectra of raw materials and of the EBM. In the HA_PCL spectrum (figure 12A), the characteristic peaks of HA at 3200–3600 cm^{-1} (OH and NH stretching), 1640–1690 cm^{-1} (C=O stretching of primary amide) and 1035 cm^{-1} (C-O-C stretching) can be observed [104]. Additionally, in the HA_PCL spectrum, the characteristic peaks of PCL at 2949 cm^{-1} (asymmetric CH_2 stretching), 2865 cm^{-1} (symmetric CH_2 stretching), 1727 cm^{-1} (carbonyl stretching), 1293 cm^{-1} (C-O and C-C stretching), 1240 cm^{-1} (asymmetric C-O-C stretching) and 1170 cm^{-1} (symmetric C-O-C stretching) were also observed [98].

On the other hand, the spectrum of the CS_ZN_SA electrospun membrane (figure 12B) contains, as expected, the typical bands of CS, ZN, and SA. The peak observed at 1374 cm^{-1} corresponds to –C–O stretching of the primary alcohol group of CS [59]. The other characteristic peaks of CS can be visualized at 3200–3400 cm^{-1} (–OH stretch), 2872 cm^{-1} (aliphatic C–H stretch) and at 1650 cm^{-1} (acetylated amine group) [105]. Additionally, the data obtained clearly show the characteristic bands of ZN are visualized in the CS_ZN_SA spectrum at 3286 and 3057 cm^{-1} (N-H stretching band of secondary amide), 1645 cm^{-1} (C=O stretching of primary amide band), and 1515 cm^{-1} (N-H bending of secondary amide band) [106]. The SA peaks in the CS_ZN_SA spectrum have a low relative intensity due to the low concentration of SA used and to the merging of the peaks with those from ZN. However, in the gathered spectrum it is possible to observe C-H stretching vibrations in the range of 3037 and 3019 cm^{-1}, and a band at 1248 cm^{-1} assigned to O-H vibrations that are characteristic of SA. Further, the band between 1830 cm^{-1} and 1750 cm^{-1} observed in the CS_ZN_SA spectrum can be assigned to the C=O vibration of SA. The C-C-C stretching of SA is

attributed to the bands that appear in the CS_SA_ZN FTIR spectrum between 1583 and 1030 cm^{-1} [88].

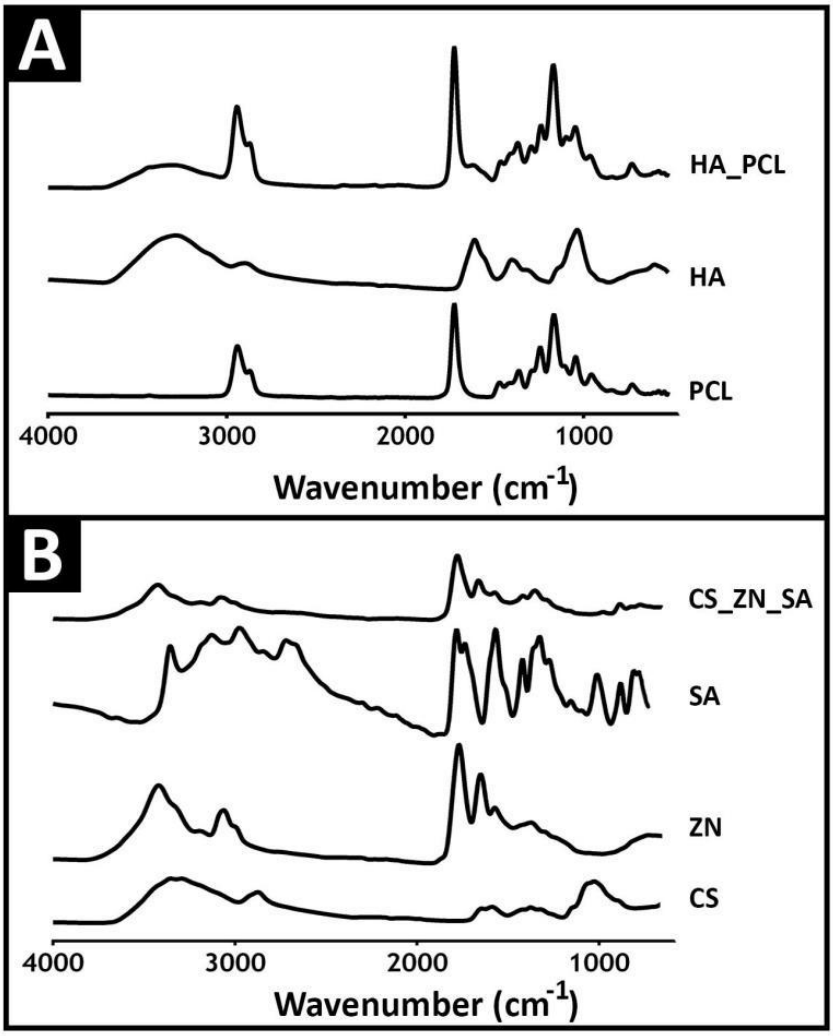

Figure 12. ATR-FTIR analysis of the EBM electrospun membranes and raw materials. ATR-FTIR analysis of HA_PCL electrospun membrane and of their raw materials (A); The ATR-FTIR spectra of the CS_ZN_SA electrospun membrane and of their raw materials are presented in (B).

3.4. Characterization of the mechanical properties of the EBM

Skin is a viscoelastic tissue whose mechanical strength is provided by the structural organization of fibers network (namely dermal collagen, elastin, and fibrillin) [107, 108]. The mechanical properties of skin are dependent on age, skin color, previous lesions, and genetic factors [93]. Nowadays, the skin substitutes produced are mechanically fragile and are unable to fully re-establish the native features of skin [109]. To overcome these drawbacks, new skin substitutes with improved mechanical properties are currently being developed. These new devices must be flexible and strong enough to allow their handling during implantation at the wound site and also confer support during new tissue formation.

Herein, extension tensile tests were performed to evaluate the mechanical properties of the EBM produced. Representative stress–strain curve and macroscopic images of the EBM during the assay are presented in figure 13. The Young's modulus, tensile strength, and elongation at break of EBM and native skin are presented in table 3. The Young's modulus obtained for EBM (4.29±1.46 MPa) is extremely close to the values displayed by native skin (4.6-20 MPa). However, the tensile strength and breaking strain values obtained for the produced EBM are slightly lower than those displayed by skin. Nevertheless, the mechanical properties of EBM are compatible with its handling during surgery and are similar to that reported for other electrospun membranes produced by other authors, that are aimed to be used as skin substitute [110, 111].

The mechanical performance displayed EBM can be attributed to PCL, a synthetic polymer well known by its mechanical strength [112]. Furthermore, the natural materials used in this study are known by their weak mechanical properties [113]. An increase in the percentage of PCL used to produce EBM would improve the mechanical behavior of the final membrane. But on the other hand, a high percentage of PCL increases the degradation time of the EBM, which could impair the healing process.

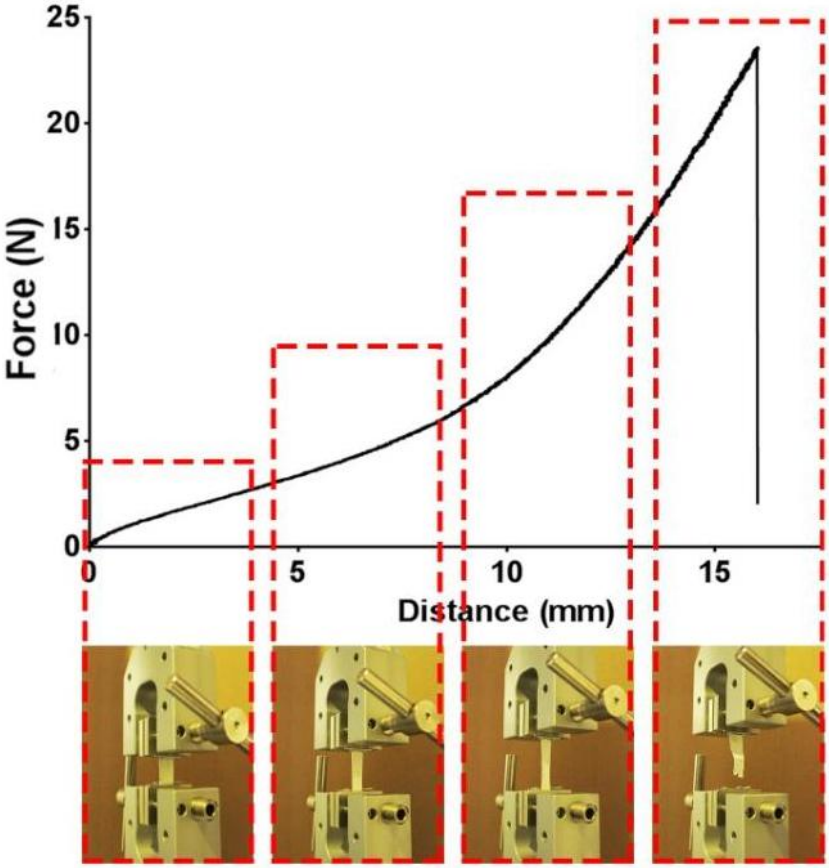

Figure 13. Representative stress–strain curve and macroscopic images of the EBM during the tensile test.

Table 3. Young's modulus, tensile strength, and elongation at break of EBM and native human skin.

	Young´s Modulus (MPa)	Tensile Strength (MPa)	Elongation at break (%)
EBM	4.29 ± 1.46	2.17 ± 0.62	23.09 ± 3.07
Native skin	4.6 - 20	5 - 30	35 - 115

3.5. Evaluation of the porosity of EBM

Porosity is viewed as a crucial feature of 3D constructs aimed for biomedical application. Cells are prone to adhere and proliferate within porous 3D constructs. Different reports have highlighted the importance of the porosity of skin substitutes for improving fibroblast, endothelial, and stem cell infiltration, as well as nutrient transport and neovascularization [114]. Electrospun meshes are characterized by a high degree of porosity which is essential for promoting homeostasis, exudates absorption, gas permeability and cell proliferation [115]. As shown in figure 14, the EBM porosity was greater than 90%. According to Freyman and colleagues porosities above 90% are ideal for tissue engineering applications since they allow cell penetration and ingrowth [116]. The HA_PCL individual electrospun mesh presented a porosity percentage below 90% which compromises the ingrowth of cells, vascularization, and diffusion of nutrients. However, the presence of a top layer with a low porosity may avoid bacterial contamination since it is described that bacteria adhere preferentially to porous materials than on dense materials [117]. Moreover, CS_ZN_SA membrane porosity is extremely high (162.35 ± 34.68 %) and cells may have difficulties in filling the void spaces existent in the nanofibrous mesh. Such feature may also compromise the mechanical properties of the membrane, as previously described by Bonvallet and collaborators [74]. As a consequence, the combination of HA_PCL with CS_ZN_SA resulted in a wound dressing with optimal porosity (90.40 ± 4.25 %) that provides a 3D structure that allows cell accommodation, migration and also enables gasses, nutrients and fluids exchange. Such processes are essential for hemostasis, and ultimately to allow a proper wound healing to occur [118].

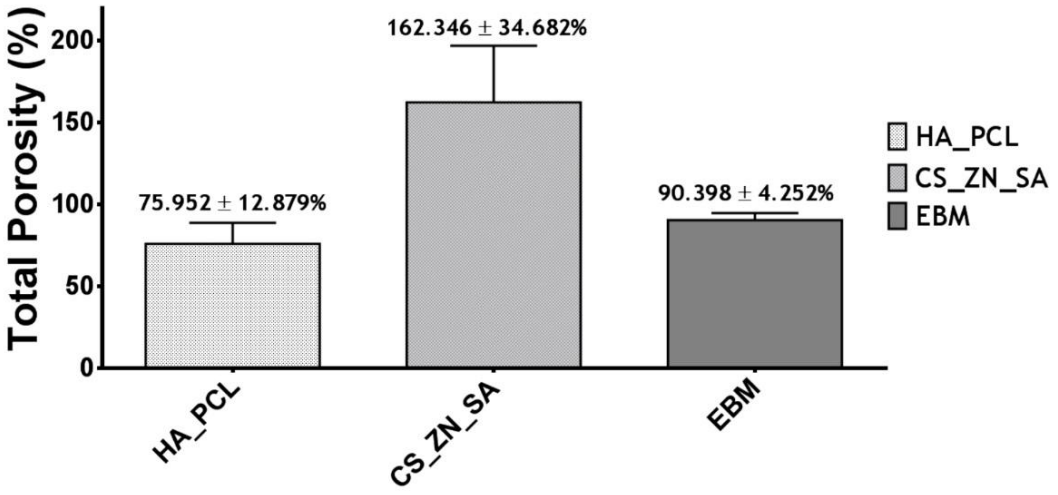

Figure 14. Characterization of the porosity of the EBM and their individual layers.

3.6. Determination of contact angle at the surfaces of EBM

In literature, it is described that a surface is considered hydrophilic if the contact angle is lower than 90°, whereas surfaces with contact angles higher than 90° are considered moderately hydrophobic. Surfaces with a contact angle between 150° and 180° are called superhydrophobic [119]. Furthermore, the wettability of the nanofibrous membranes is an important parameter since it influences the host response to the implanted material, affecting the initial cellular adhesion and also their proliferation [120].

Herein, the upper layer of EBM (HA_PCL) presented a contact angle of 120.20 ± 0.85° and thus a hydrophobic character (90°<Water Contact Angle<150°). These results were expectable since PCL is present in this layer [53]. On the other hand, the bottom layer of EBM (CS_ZN_SA) presented a water contact angle of 101.96 ± 5.08° (figure 15). This value shows that this inner layer has a less hydrophobic character than the top layer (HA_PCL). Nevertheless, the hydrophobicity of CS_ZN_SA layer is related to the high hydrophobicity of ZN protein used to produce the electrospun mesh. Specifically, the presence of apolar amino acids (proline and glutamine) in the polypeptide chain of ZN may explain its hydrophobic character [121]. However, the hydrophobic character displayed by CS_ZN_SA layer is desirable, since it may have an important role in the regulation of the release of SA, by preventing the immediate hydration of the matrix, solubilization of the drug and diffusion from the fibers [122]. Therefore, the amount of ZN used was selected in order to maintain fiber stability and simultaneously allow an appropriate drug release. In addition, the effect of EBM surface properties in cellular attachment and proliferation is discussed in more detail in section 3.9.

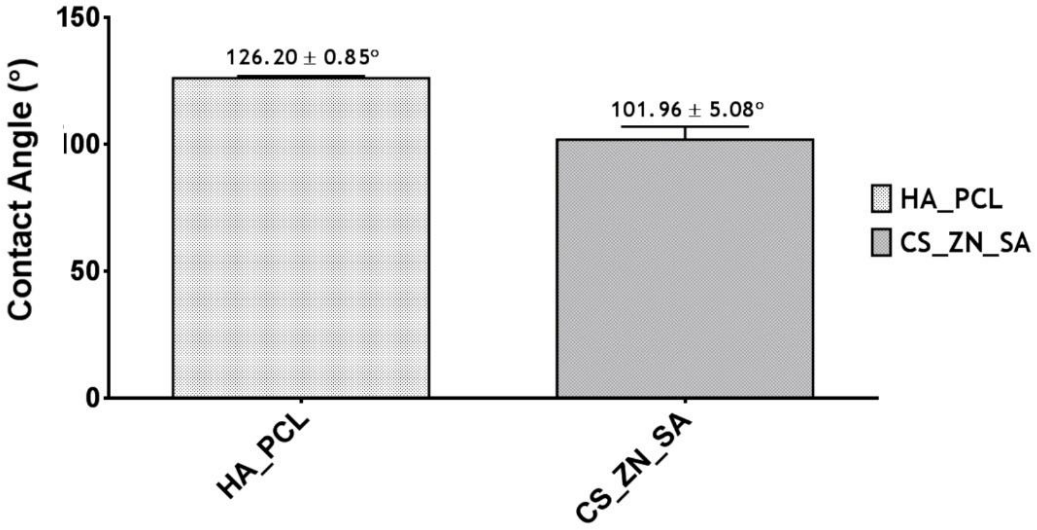

Figure 15. Characterization of the water contact angles of the top and bottom layers of EBM.

3.7. Water vapor transmission rate

The maintenance of a moist environment at the wound site is crucial for improving the healing process. In fact, a moist environment avoids patient dehydration, enhances angiogenesis and collagen synthesis. Thereunto, WVTR was determined in order to assess the EBM capacity to maintain a moist environment in the wound. The obtained data shows a nearly constant water weight loss for control and membrane sealed group (figure 16).

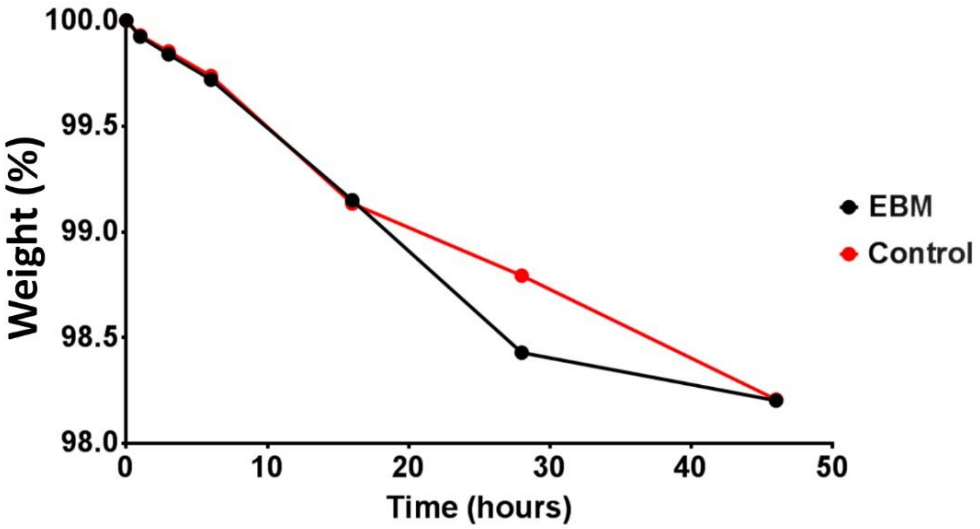

Figure 16. Characterization of the water vapor transmission profile for control and EBM.

The results showed that EBM had a WVTR of 1762.91 ± 187.50 mL/m^2/day, a value that is similar to the control (1539.36 ± 50.01 mL/ m^2/day) (table 4). These results demonstrate that EBM does not limit water vapor exchanges. Furthermore, the recommended WVTR of wound dressings is 2000-2500 mL/m^2/day, which is half of the value presented by granulation tissue (5138 ± 202

mL/m^2/day) [123]. Therefore, EBM can be used to control the water vapor losses and also prevent the accumulation of exudates, which are commonly present in full thickness wounds. The exudate retention leads to the buildup of a back pressure that is responsible for the maceration of the healthy surrounding tissue, thus inducing pain to patient [124].

Table 4. Water vapor transmission profile for control and EBM.

Water Vapour Transmission Rate (mL/m²/day)	
Control	EBM
1539.36 ± 50.06	1762.91 ± 187.49

3.8. Characterization of the biodegradation profile of EBM

Biomaterials applied in tissue regeneration must be biodegradable in order to allow their application as temporary ECM. Ideally, the degradation rate of polymeric matrices must be compatible with the new tissue formation. Fast degradation rates lead to the loss of tissue integrity and functions, whereas slow degradation rates can result in mechanical mismatches such as stress shielding, that may lead to the failure of the system. To mimic the environment found in skin, degradation studies of the individual HA_PCL, CS_ZN_SA and EBM were performed using PBS, at pH 5.50, and 37 ^{o}C.

As can be observed in figure 17, HA_PCL membrane lost approximately 5% of its weight after 7 days. Such result can be explained by the presence of PCL, which exhibits a slow degradation rate [125]. As an aliphatic polyester, PCL degrades through the hydrolysis of the ester bonds but it can also be degraded through enzymatic action [126]. Several works evidenced that PCL-based wound dressings present a weight loss compatible with skin regeneration [109]. On the other hand, it was demonstrated that HA-based polymers present a controlled biodegradability. These polymers can be degraded by enzymatic action, specifically through hyaluronidases [127].

Moreover, the obtained results show that the CS_ZN_SA monolayer membrane presents the highest weight loss (almost 30%) after 7 days [11]. This result is in agreement with the data available in the literature: Lin and colleagues, produced ZN-collagen nanofibers that suffered a maximum 47% of weight loss after 14 days [121]. However, it was also demonstrated that the degradation products of ZN and CS can enhance cell proliferation [128-130]. Sun *et al*, for example, added the ZN degradation products to RPMI 1640 complete culture medium and verified that when their concentration was lower than 1 mg/mL, these products were able to stimulate the proliferation of human liver cells (HL-770) [128]. The degradation products of ZN are mainly composed of amino acid residues (such as cysteine and methionine) that do not affect the pH of the culture medium and do not impair cellular behavior [131]. Additionally, Ribeiro and

collaborators produced a CS hydrogel and concluded that the CS by-products (N-acetylchito-oligosaccharides and chitooligosaccharides) do not affect NHDF cells viability [132].

EBM lost 5% of its mass in 3 days and almost 10% after 7 days. The controlled degradation process observed for EBM further corroborates the entanglement between two layers. Figure 18 shows that the top and bottom layers of EBM suffered some changes along 7 days of incubation. After this period, the layers displayed a lower fiber density and fibers became more irregular. This may have a positive effect on cellular internalization, nutrients diffusion and ultimately on the skin healing process.

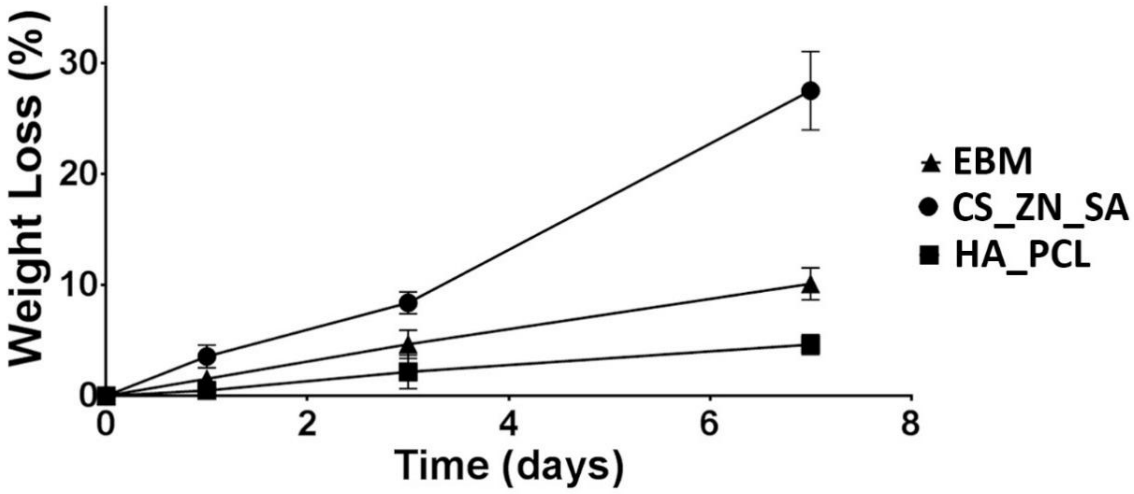

Figure 17. Evaluation of the weight loss of the different membranes produced along 7 days.

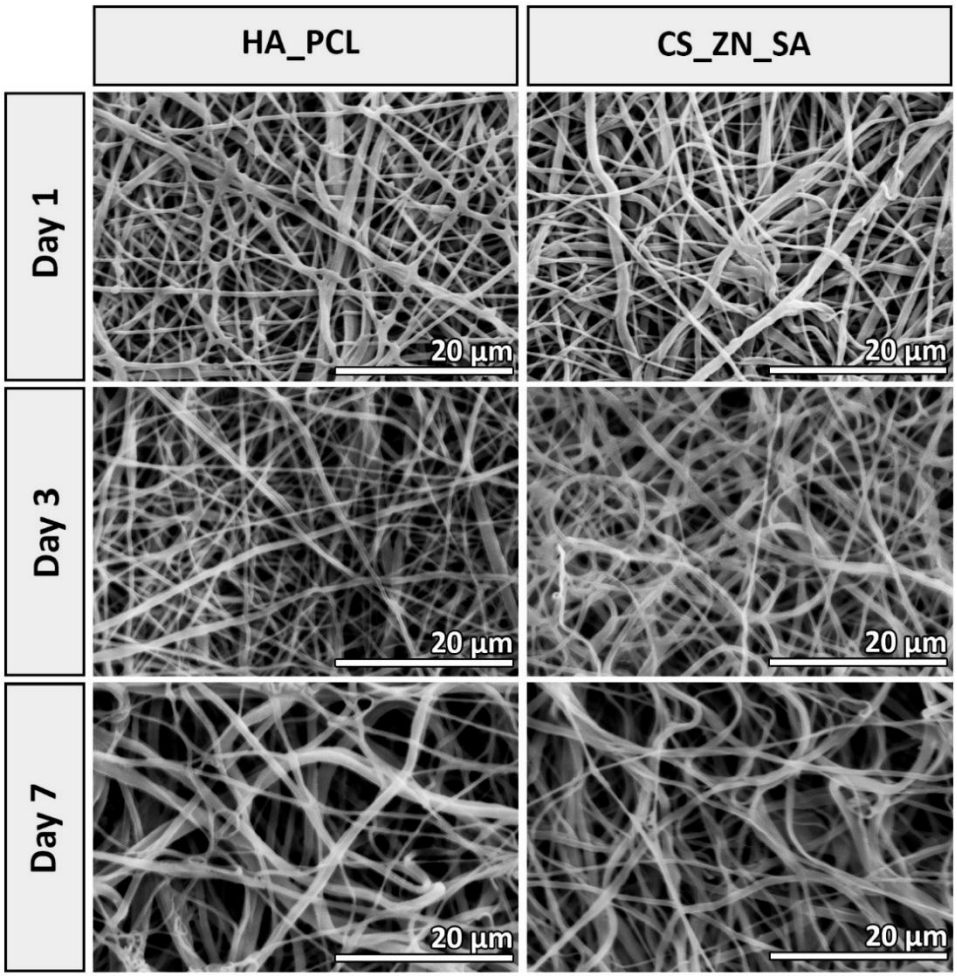

Figure 18. SEM images of the top (HA_PCL) and bottom layer (CS_ZN_SA) after 1, 3 and 7 days of being incubated with PBS.

3.8. Determination of SA release from EBM

As can be observed in figure 19, approximately 16% of SA was released from EBM during 5 days. SA release is controlled predominantly by the degradation of the EBM. Thus, as the polymers degrade, the drug is released. During the first hour in contact with PBS at 37 ^{o}C, the EBM exhibit a significant release of SA, known as burst release. Following that, a sustained release of the SA entrapped within the polymeric mesh was noticed. The initial burst release of SA is appropriate to eliminate bacteria at the wound site, while a subsequent slow release of the drug may avoid biofilm formation and infection at the wound site [32]. Similarly, Nguyen and co-workers have incorporated SA in poly(ethylene glycol) (PEG) and poly(lactic acid) (PLA) core-shell electrospun membranes, in order to improve the wound healing process. In their study, the SA suffered an initial burst release due to the high concentration of the drug available on the nanofibers surface and a subsequent sustained release during 5 days [133]. The results obtained in our study for SA release avoided the formation of at least 5 days, as will be discussed in section 3.10.

Furthermore, there are several studies which emphasize the important role of SA in the treatment of skin disorders, such as acne, bacterial and fungal infections [134]. In cosmetics, SA

is applied to reduce wrinkles and sagginess of the skin after wound repair. Moreover, SA is also used as antiseptic and disinfectant since its keratolytic activity promotes the removal of dead or hyper keratinized skins, while reducing inflammation [135].

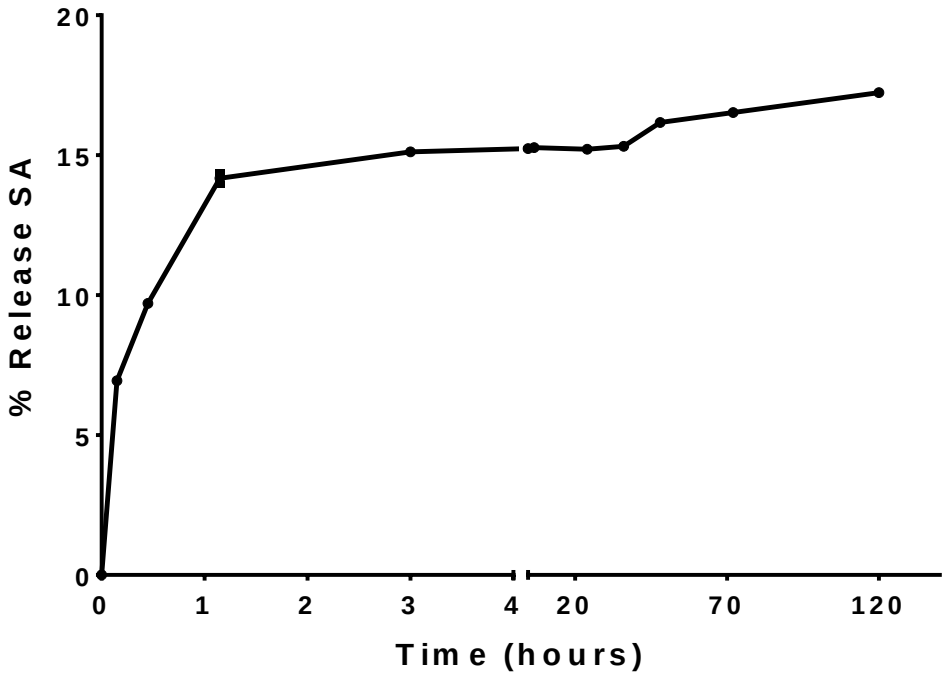

Figure 19. Release profile of SA from electrospun EBM into PBS at 37 °C and pH 5.50.

3.9. Evaluation of cell viability and proliferation in the presence of EBM

To evaluate the cytotoxic character of EBM, NHDF were used as model cells. NHDF were chosen due to their important role in wound healing process, specifically, they interact with the surrounding cells (keratinocytes, fat cells, and mast cells) and produce ECM proteins, glycoproteins, adhesive molecules and various cytokines [136].

Optical microscopic images of NHDF cells in contact with the produced membranes at 1, 3 and 7 days were acquired (figure 20). The images show that NHDF cells in contact with the materials do not suffer any morphologic variation and were able to proliferate similarly to cells from K^- (cells grown without being in contact with biomaterials). As expected, cells presented in K^+ display a spherical shape, which is characteristic of dead cells.

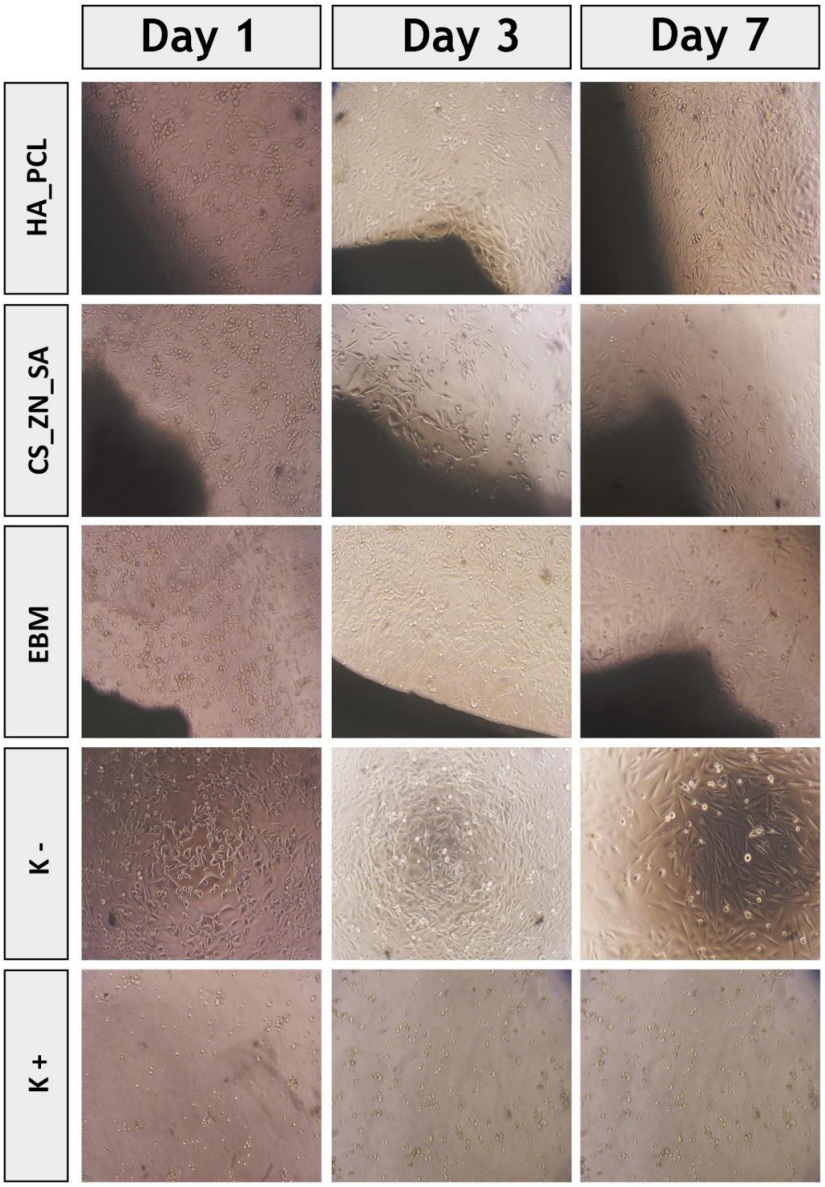

Figure 20. Microscopic images of NHDF in the presence of electrospun membranes after 1, 3 and 7 days after seeding; K - (negative control); K + (positive control).

Additionally, cell viability was also characterized through an MTT assay during 1, 3 and 7 days. The metabolic conversion of MTT, a yellow tetrazole salt, to purple formazan crystals occurs in living cells and such process is proportional to the number of viable cells present in each well [137]. The data obtained from the MTT assay (figure 21) revealed that the individual electrospun layers (HA_PCL and CS_ZN_SA) and EBM did not affect the cellular viability for 7 days.

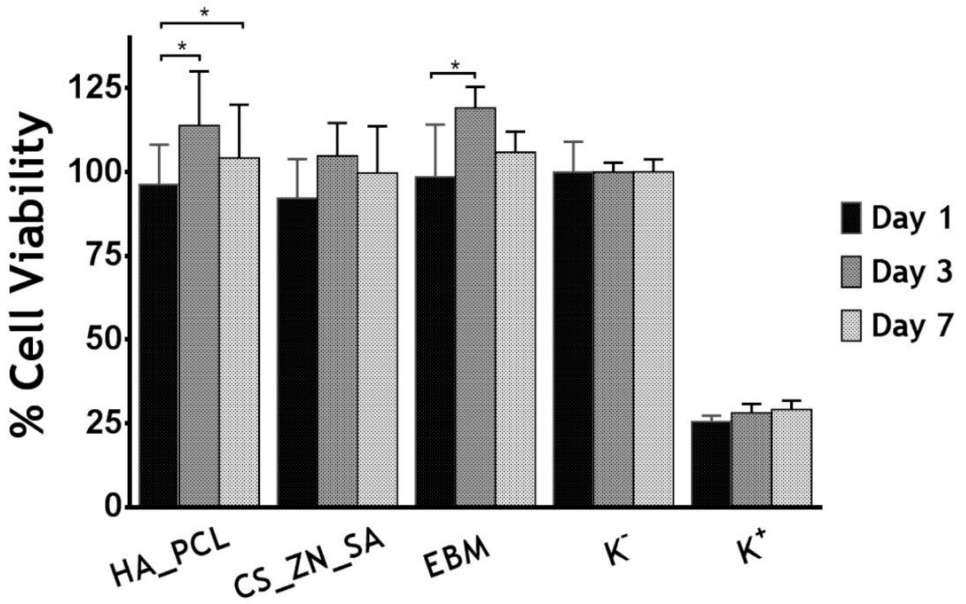

Figure 21. Evaluation of NHDF viability when cultured in the presence of the produced electrospun membranes after 1, 3 and 7 days. Positive control (K+) and negative control (K−) indicate dead and viable cells, respectively. Statistical analysis was performed using one-way ANOVA with Newman–Keuls test.

On the other hand, EBM may provide a three-dimensional structure for cellular attachment, growth, and migration. Therefore, cellular morphology and the interaction between cells and nanofibers were also evaluated by SEM (figure 22). After 3 days, the cells already present a typical morphology with various filopodia protrusions, suggesting that NHDF cells can adhere and proliferate on the surface of EBM. At day 7, cells were completely attached to the top and bottom of EBM. Such fact can be explained by the interaction of cells membrane glycosaminoglycans with the amine groups present on the surface of CS_ZN_SA membrane [138].

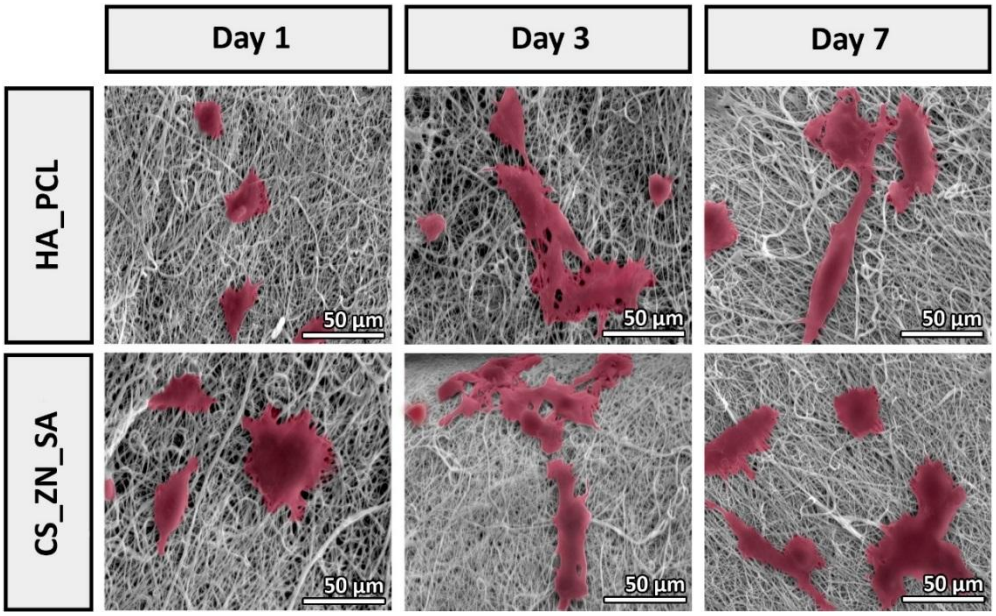

Figure 22. SEM micrographs illustrating fibroblasts morphology at the surface of the different electrospun membranes produced after 1, 3 and 7 days.

Furthermore, CLSM images were also acquired (figure 23), and they corroborate the previous results obtained by SEM analysis. The cells maintained a normal phenotype and remained biologically active on the surface of both layers of EBM. After 3 days of culture, the cellular adhesion and proliferation onto the nanofibrous matrix are higher than in K^-. These results demonstrate that EBM has excellent potential to support fibroblasts attachment, migration, and proliferation, which is crucial for improving the wound healing process.

All these data clearly shows that EBM enhances the wound healing process by promoting the migration, proliferation, and adhesion of fibroblast cells. Once fibroblasts are at the wound site, they produce and secrete ECM proteins (predominantly collagen type I) and also activate growth factors such as Transforming Growth Factor-ß1 (TGF-ß1) that are required for restoring the structure of the injured tissue [34].

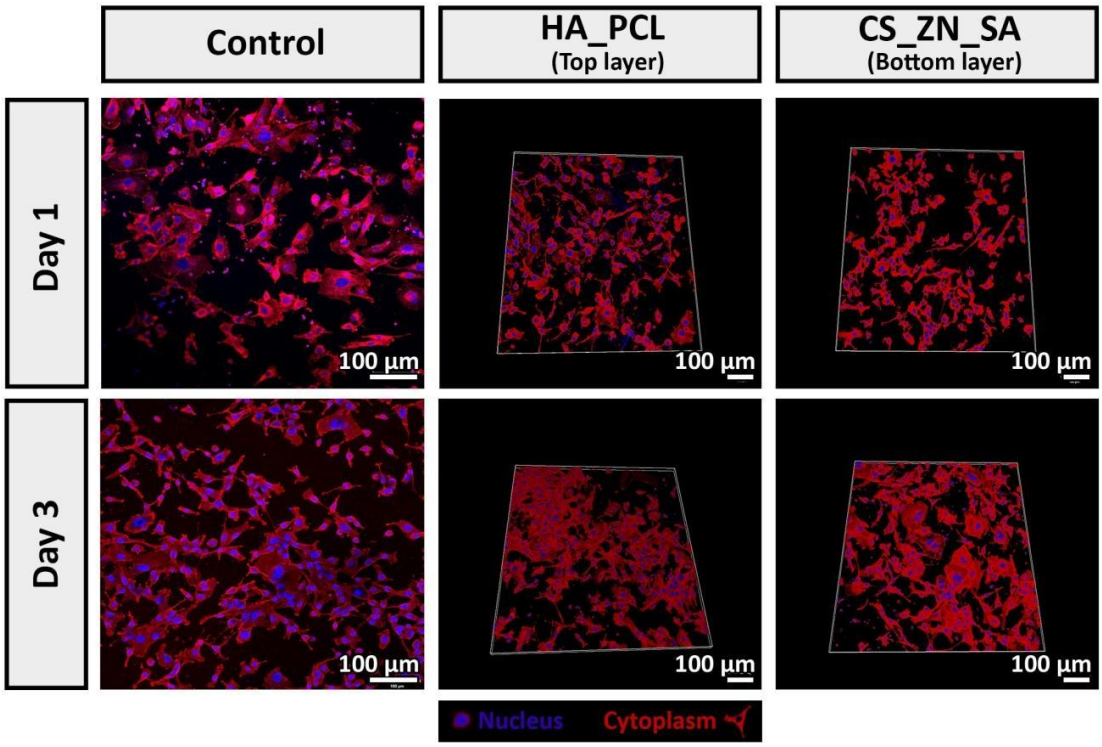

Figure 23. CLSM images of fibroblasts cultured on µ-Slide 8 well Ibidi imaging plates (Control), HA_PCL and CS_ZN_SA membranes after 1 and 3 days. Blue channel: cell nuclei-labeled Hoechst 33342®; Red Channel: cytoplasm stained with WGA-Alexa 594® conjugate.

3.10. Characterization of the antimicrobial properties of the membranes

Bacterial infections are currently regarded as the most severe and devastating complications associated with the implantation of biomaterials in the human body [75]. Nowadays, it is estimated that 65-80% of bacterial infections are caused by organisms that form biofilms on implants´ surface, compromising their successful application [76]. In this context, the

development of biomaterials with bactericidal activity is fundamental to avoid infections related to materials implantation.

S. aureus strain was used, herein, as model bacteria to evaluate the bactericidal activity of the EBM. This strain was selected since it is described as the most common pathogen found in skin infections when biomaterials are used for wound treatments [91].

To determine the antimicrobial activity of the individual layers (HA_PCL and CS_ZN_SA) and EBM, membranes were placed on agar plates in contact with *S.aureus* during 5 days. The diameter of the inhibitory halos was measured (figure 24). Furthermore, biofilm formation on membrane surface was evaluated by SEM analysis during 5 days. The EBM presented inhibitory halos of 9,84 ± 3,64 mm (figure 24B) and the absence of biofilm formation on their surface was confirmed for 5 days by SEM analysis (figure 25B). In comparison with the individual electrospun membranes, EBM showed the highest inhibitory halo diameter. This capacity can be attributed to a synergetic effect resulting from the assembly of two hydrophobic layers. Besides that, the antimicrobial activity of EBM results also from the presence of SA and CS that are already extensively described in the literature as holders of antimicrobial properties [135].

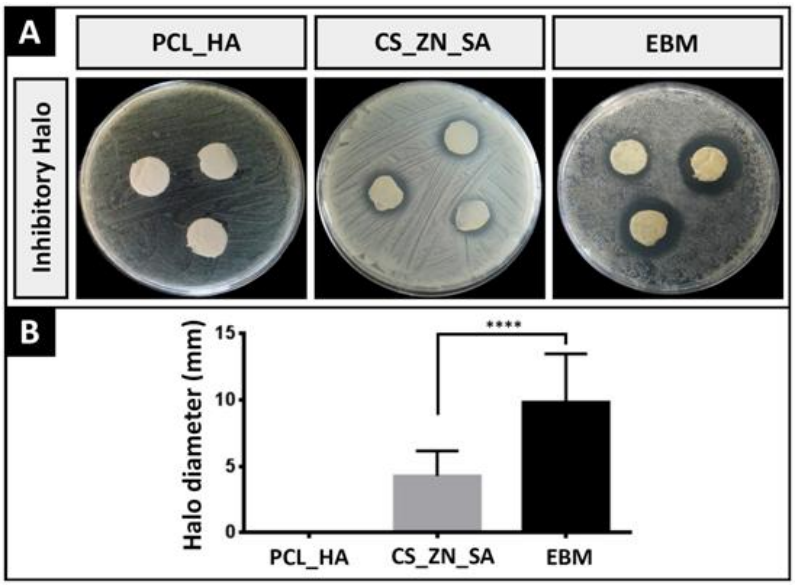

Figure 24. Evaluation of the bactericidal activity of the produced membranes: Macroscopic images of the inhibitory halos around the membrane produced in this study (A); Determination of the diameter of inhibitory halos obtained for membranes in contact with S. aureus (B).

SA is a phenolic compound produced by plants that play an important role in several physiological processes, such as the induction of plant defense responses against pathogen attacks [139]. Furthermore, it is also responsible for the inhibition of cyclooxygenase (COX), known to be a key player in body's inflammatory response [140]. The antimicrobial activity of SA is not yet widely described in the literature, but there are some authors that have already demonstrated the effect of SA against the formation and growth of biofilms [141]. Lee *et al* proposed that the free phenolic hydroxyl group of SA is able to kill bacteria, through a mechanism where the proton

gradient present in bacterial cells is destroyed [142]. Kupferwasser and collaborators showed that the treatment of infections caused by *S. aureus* with aspirin resulted in a significant reduction of bacterial densities at the target tissues [143]. Later, the same author reported that SA leads to a subexpression of structural genes of *S. aureus*, namely alpha-hemolysin gene promoter (hla) and the fibronectin gene promoter (fnbA). As a consequence, staphylococcal malignancy is decreased [144]. On the other hand, CS is a polysaccharide obtained by the deacetylation of chitin. CS antimicrobial activity is associated with its positively charged amino groups that are able to interact with negatively charged groups available at microbial cell wall, leading to the leakage of the intracellular constituents of the microorganisms [145]. For that reason, several studies showed that CS has a strong bactericidal activity against gram-positive bacteria, such as *S. aureus* [146, 147].

The synergistic effect observed between CS and SA results in a bilayered system with antimicrobial activity for at least 5 days. This profile is suitable to provide an aseptic environment at the wound site, inhibiting the bacterial proliferation, and hence, facilitating the wound healing process.

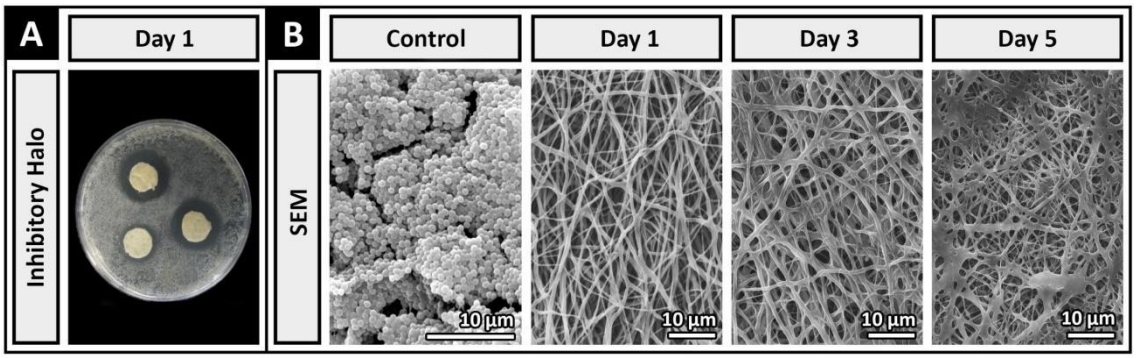

Figure 25. Evaluation of the bactericidal activity of the produced membranes: Macroscopic images of the inhibitory halos (A); SEM images of membranes in contact with S. aureus and the bacterial growth at agar plate (negative control) (B).

Chapter IV - Conclusion

4. Conclusion

Every year millions of people around the world experience both acute and chronic skin injuries. Among several types of dressings applied in the treatment of skin damages, the bioactive dressings such as electrospun membranes are the most effective. This type of membranes gained special attention in the area of skin tissue engineering since they present a similar morphology and structure to that of the ECM. Furthermore, the easy incorporation of drugs into nanofibrous structures can also improve the healing process. In this study, an innovative bilayer electrospun membrane was produced to cover/protect the wound as well as promote the wound healing process. The top and bottom layers were produced using natural (CS, ZN, and HA) and synthetic (PCL) materials, respectively. The combination of natural and synthetic materials in a bilayer scaffold resulted in a system with suitable physicochemical properties as well as excellent biological performance. Furthermore, the encapsulation of the active component of aspirin, SA, in EBM avoided the bacterial growth on the surface of the nanofibrous matrix. The *in vitro* assays revealed that the wound dressing is noncytotoxic and provides a 3D polymeric support to allow cell adhesion and proliferation.

The incorporation of growth factors, vitamins, and other biomolecules to enhance the healing processes can be hypothesized as a future prospect for improving the performance of these membranes. Furthermore, the real-time detection of the wound bed environment parameters, including pH or temperature, through biosensors that can be incorporated in the skin substitutes can allow the development smart devices capable of monitoring the healing process in real time.

🕮 Chapter V - Bibliography

5. Bibliography

1. Heuke, S., et al., *Multimodal mapping of human skin.* British Journal of Dermatology, 2013. **169**(4): p. 794-803.
2. Zhong, S., Y. Zhang, and C. Lim, *Tissue scaffolds for skin wound healing and dermal reconstruction.* Wiley Interdisciplinary Reviews: Nanomedicine and Nanobiotechnology, 2010. **2**(5): p. 510-525.
3. Wong, R., et al., *The dynamic anatomy and patterning of skin.* Experimental dermatology, 2015. 25 (**2**): p. 92-98.
4. Decker, R.H., E.A. Strom, and L.D. Wilson, *Skin Surface, Dermis, and Wound Healing*, in *ALERT• Adverse Late Effects of Cancer Treatment*. 2014, Springer. p. 205-226.
5. Haftek, M., *'Memory'of the stratum corneum: exploration of the epidermis' past.* British Journal of Dermatology, 2014. **171**(s3): p. 6-9.
6. Wortsman, X., et al., *Sonographic anatomy of the skin, appendages, and adjacent structures*, in *Dermatologic Ultrasound with Clinical and Histologic Correlations*. 2013, Springer. p. 15-35.
7. Brohem, C.A., et al., *Artificial skin in perspective: concepts and applications.* Pigment cell & melanoma research, 2011. **24**(1): p. 35-50.
8. Nishifuji, K. and J.S. Yoon, *The stratum corneum: the rampart of the mammalian body.* Veterinary dermatology, 2013. **24**(1): p. 60-e16.
9. Visscher, M. and V. Narendran, *Neonatal infant skin: development, structure and function.* Newborn and Infant Nursing Reviews, 2014. **14**(4): p. 135-141.
10. Masunaga, T., *Epidermal basement membrane: its molecular organization and blistering disorders.* Connective tissue research, 2006. **47**(2): p. 55-66.
11. Zhang, Z. and B.B. Michniak-Kohn, *Tissue engineered human skin equivalents.* Pharmaceutics, 2012. **4**(1): p. 26-41.
12. Breitkreutz, D., N. Mirancea, and R. Nischt, *Basement membranes in skin: unique matrix structures with diverse functions?* Histochemistry and cell biology, 2009. **132**(1): p. 1-10.
13. Behrens, D.T., et al., *The epidermal basement membrane is a composite of separate laminin-or collagen IV-containing networks connected by aggregated perlecan, but not by nidogens.* Journal of Biological Chemistry, 2012. **287**(22): p. 18700-18709.
14. Jepps, O.G., et al., *Modeling the human skin barrier—Towards a better understanding of dermal absorption.* Advanced drug delivery reviews, 2013. **65**(2): p. 152-168.
15. Metcalfe, A.D. and M.W. Ferguson, *Tissue engineering of replacement skin: the crossroads of biomaterials, wound healing, embryonic development, stem cells and regeneration.* Journal of the Royal Society Interface, 2007. **4**(14): p. 413-437.

16. Legué, E. and J.-F. Nicolas, *Hair follicle renewal: organization of stem cells in the matrix and the role of stereotyped lineages and behaviors*. Development, 2005. **132**(18): p. 4143-4154.
17. Tobin, D.J., *Biochemistry of human skin—our brain on the outside*. Chemical Society Reviews, 2006. **35**(1): p. 52-67.
18. Saito, M., M. Ohyama, and M. Amagai, *Exploring the biology of the nail: An intriguing but less-investigated skin appendage*. Journal of dermatological science, 2015. **79**(3): p. 187-193.
19. Fleckman, P., et al., *Comparative anatomy of mouse and human nail units*. The Anatomical Record, 2013. **296**(3): p. 521-532.
20. Smith, K. and D. Thiboutot, *Thematic review series: skin lipids. Sebaceous gland lipids: friend or foe?* Journal of lipid research, 2008. **49**(2): p. 271-281.
21. Noel, F., et al., *Immunohistochemical sweat gland profiles*. Journal of cosmetic dermatology, 2013. **12**(3): p. 179-186.
22. Boateng, J.S., et al., *Wound healing dressings and drug delivery systems: a review*. Journal of pharmaceutical sciences, 2008. **97**(8): p. 2892-2923.
23. Behm, B., et al., *Cytokines, chemokines and growth factors in wound healing*. Journal of the European Academy of Dermatology and Venereology, 2012. **26**(7): p. 812-820.
24. Rizzi, S.C., et al., *Recent advances in dermal wound healing: biomedical device approaches*. Expert review of medical devices, 2010. **7**(1): p. 143-154.
25. Sun, B.K., Z. Siprashvili, and P.A. Khavari, *Advances in skin grafting and treatment of cutaneous wounds*. Science, 2014. **346**(6212): p. 941-945.
26. Rowan, M.P., et al., *Burn wound healing and treatment: review and advancements*. Critical Care, 2015. **19**(1): p. 1-12.
27. Sen, C.K., et al., *Human skin wounds: a major and snowballing threat to public health and the economy*. Wound Repair and Regeneration, 2009. **17**(6): p. 763-771.
28. Papini, R., *Management of burn injuries of various depths*. Bmj, 2004. **329**(7458): p. 158-160.
29. Shevchenko, R.V., S.L. James, and S.E. James, *A review of tissue-engineered skin bioconstructs available for skin reconstruction*. Journal of the Royal Society Interface, 2010. **7**(43): p. 229-258.
30. Martin, P. and R. Nunan, *Cellular and molecular mechanisms of repair in acute and chronic wound healing*. British Journal of Dermatology, 2015. **173**(2): p. 370-378.
31. Menke, N.B., et al., *Impaired wound healing*. Clinics in dermatology, 2007. **25**(1): p. 19-25.
32. Rieger, K.A., N.P. Birch, and J.D. Schiffman, *Designing electrospun nanofiber mats to promote wound healing-a review*. Journal of Materials Chemistry B, 2013. **1**(36): p. 4531-4541.
33. Guo, S. and L.A. DiPietro, *Factors affecting wound healing*. Journal of dental research, 2010. **89**(3): p. 219-229.

34. Maxson, S., et al., *Concise review: role of mesenchymal stem cells in wound repair*. Stem cells translational medicine, 2012. **1**(2): p. 142-149.
35. Wild, T., et al., *Basics in nutrition and wound healing*. Nutrition, 2010. **26**(9): p. 862-866.
36. Bielefeld, K.A., S. Amini-Nik, and B.A. Alman, *Cutaneous wound healing: recruiting developmental pathways for regeneration*. Cellular and Molecular Life Sciences, 2013. **70**(12): p. 2059-2081.
37. Blais, M., et al., *Concise review: tissue-engineered skin and nerve regeneration in burn treatment*. Stem cells translational medicine, 2013. **2**(7): p. 545-551.
38. Miner, J., P. Gruber, and T.L. Perry, *Early excision and grafting, an alternative approach to the surgical management of large body surface area levamisole-adulterated cocaine induced skin necrosis*. Burns, 2015. **41**(3): p. e34-e40.
39. Catalano, E., et al., *Tissue-engineered skin substitutes: an overview*. Journal of Artificial Organs, 2013. **16**(4): p. 397-403.
40. Dvir, T., et al., *Nanotechnological strategies for engineering complex tissues*. Nature nanotechnology, 2011. **6**(1): p. 13-22.
41. Zahedi, P., et al., *A review on wound dressings with an emphasis on electrospun nanofibrous polymeric bandages*. Polymers for Advanced Technologies, 2010. **21**(2): p. 77-95.
42. Kamolz, L., et al., *Tissue engineering for cutaneous wounds: an overview of current standards and possibilities*. European Surgery, 2008. **40**(1): p. 19-26.
43. Jayarama Reddy, V., et al., *Nanofibrous structured biomimetic strategies for skin tissue regeneration*. Wound Repair and Regeneration, 2013. **21**(1): p. 1-16.
44. Clark, R.A., K. Ghosh, and M.G. Tonnesen, *Tissue engineering for cutaneous wounds*. Journal of Investigative Dermatology, 2007. **127**(5): p. 1018-1029.
45. Greaves, N.S., et al., *The role of skin substitutes in the management of chronic cutaneous wounds*. Wound repair and regeneration, 2013. **21**(2): p. 194-210.
46. Schwarze, H., et al., *Suprathel, a new skin substitute, in the management of partial-thickness burn wounds: results of a clinical study*. Annals of plastic surgery, 2008. **60**(2): p. 181-185.
47. Shakespeare, P.G., *The role of skin substitutes in the treatment of burn injuries*. Clinics in dermatology, 2005. **23**(4): p. 413-418.
48. Chiu, T. and A. Burd, *"Xenograft" dressing in the treatment of burns*. Clinics in dermatology, 2005. **23**(4): p. 419-423.
49. Sahay, R., et al., *Electrospun composite nanofibers and their multifaceted applications*. Journal of Materials Chemistry, 2012. **22**(26): p. 12953-12971.
50. Jiang, T., et al., *Electrospinning of polymer nanofibers for tissue regeneration*. Progress in Polymer Science, 2015. **46**: p. 1-24.
51. Khorshidi, S., et al., *A review of key challenges of electrospun scaffolds for tissue-engineering applications*. Journal of tissue engineering and regenerative medicine, 2015. DOI: 10.1002/term.1978.

52. Abrigo, M., S.L. McArthur, and P. Kingshott, *Electrospun nanofibers as dressings for chronic wound care: advances, challenges, and future prospects*. Macromolecular Bioscience, 2014. **14**(6): p. 772-792.
53. Augustine, R., N. Kalarikkal, and S. Thomas, *Advancement of wound care from grafts to bioengineered smart skin substitutes*. Progress in Biomaterials, 2014. **3**(2-4): p. 103-113.
54. Sundaramurthi, D., U.M. Krishnan, and S. Sethuraman, *Electrospun nanofibers as scaffolds for skin tissue engineering*. Polymer Reviews, 2014. **54**(2): p. 348-376.
55. Yarin, A., *Coaxial electrospinning and emulsion electrospinning of core–shell fibers*. Polymers for Advanced Technologies, 2011. **22**(3): p. 310-317.
56. Gasperini, L., J.F. Mano, and R.L. Reis, *Natural polymers for the microencapsulation of cells*. Journal of The Royal Society Interface, 2014. **11**(100): p. 20140817.
57. Zhou, Y., et al., *Electrospun water-soluble carboxyethyl chitosan/poly (vinyl alcohol) nanofibrous membrane as potential wound dressing for skin regeneration*. Biomacromolecules, 2007. **9**(1): p. 349-354.
58. Cai, Z.-x., et al., *Fabrication of chitosan/silk fibroin composite nanofibers for wound-dressing applications*. International journal of molecular sciences, 2010. **11**(9): p. 3529-3539.
59. Antunes, B., et al., *Chitosan/arginine–chitosan polymer blends for assembly of nanofibrous membranes for wound regeneration*. Carbohydrate polymers, 2015. **130**: p. 104-112.
60. Carvalho, M.P., et al., *Tumor spheroid assembly on hyaluronic acid-based structures: a review*. Carbohydrate Polymers, 2016. **150**: p.139-148.
61. Bhardwaj, N. and S.C. Kundu, *Electrospinning: a fascinating fiber fabrication technique*. Biotechnology advances, 2010. **28**(3): p. 325-347.
62. Hsu, F.-Y., et al., *Electrospun hyaluronate–collagen nanofibrous matrix and the effects of varying the concentration of hyaluronate on the characteristics of foreskin fibroblast cells*. Acta biomaterialia, 2010. **6**(6): p. 2140-2147.
63. Li, L., et al., *The use of hyaluronan to regulate protein adsorption and cell infiltration in nanofibrous scaffolds*. Biomaterials, 2012. **33**(12): p. 3428-3445.
64. Wang, Z., et al., *Evaluation of emulsion electrospun polycaprolactone/hyaluronan/epidermal growth factor nanofibrous scaffolds for wound healing*. Journal of biomaterials applications, 2015: p. 0885328215586907.
65. Lai, H.-J., et al., *Tailored design of electrospun composite nanofibers with staged release of multiple angiogenic growth factors for chronic wound healing*. Acta biomaterialia, 2014. **10**(10): p. 4156-4166.
66. Lawton, J.W., *Zein: A history of processing and use*. Cereal Chemistry, 2002. **79**(1): p. 1-18.
67. Luo, Y. and Q. Wang, *Zein-based micro-and nano-particles for drug and nutrient delivery: A review*. Journal of Applied Polymer Science, 2014. **131**(16): p. 40696.

68. Yao, C., et al., *Biodegradable nanofibrous membrane of zein/silk fibroin by electrospinning*. Polymer international, 2009. **58**(4): p. 396-402.
69. Huang, W., et al., *Drug-loaded zein nanofibers prepared using a modified coaxial electrospinning process*. AAPS PharmSciTech, 2013. **14**(2): p. 675-681.
70. Unnithan, A.R., et al., *Electrospun antibacterial polyurethane–cellulose acetate–zein composite mats for wound dressing*. Carbohydrate polymers, 2014. **102**: p. 884-892.
71. Dashdorj, U., et al., *Fabrication and characterization of electrospun zein/Ag nanocomposite mats for wound dressing applications*. International journal of biological macromolecules, 2015. **80**: p. 1-7.
72. Khajavi, R., M. Abbasipour, and A. Bahador, *Electrospun biodegradable nanofibers scaffolds for bone tissue engineering*. Journal of Applied Polymer Science, 2016. **133**(3): p. 42883.
73. Duan, H., et al., *Engineering of epidermis skin grafts using electrospun nanofibrous gelatin/polycaprolactone membranes*. Internation Journal of Nanomedicine, 2013. **8**: p. 2077-2084.
74. Bonvallet, P.P., et al., *Microporous dermal-like electrospun scaffolds promote accelerated skin regeneration*. Tissue Engineering Part A, 2014. **20**(17-18): p. 2434-2445.
75. van Oosten, M., et al., *Real-time in vivo imaging of invasive-and biomaterial-associated bacterial infections using fluorescently labelled vancomycin*. Nature communications, 2013. **4**: p. 1-8.
76. Fux, C.A., et al., *Bacterial biofilms: a diagnostic and therapeutic challenge*. Expert review of anti-infective therapy, 2003. **1**(4): p. 667-683.
77. Page, K., M. Wilson, and I.P. Parkin, *Antimicrobial surfaces and their potential in reducing the role of the inanimate environment in the incidence of hospital-acquired infections*. Journal of Materials Chemistry, 2009. **19**(23): p. 3819-3831.
78. Guo, Q., et al., *"Paintable" 3D printed structures via a post-ATRP process with antimicrobial function for biomedical applications*. Journal of Materials Chemistry B, 2013. **1**(48): p. 6644-6649.
79. Zhao, Q., et al., *Evaluation of bacterial adhesion on Si-doped diamond-like carbon films*. Applied surface science, 2007. **253**(17): p. 7254-7259.
80. Hauert, R., *A review of modified DLC coatings for biological applications*. Diamond and Related Materials, 2003. **12**(3): p. 583-589.
81. Park, S.-N., J.K. Kim, and H. Suh, *Evaluation of antibiotic-loaded collagen-hyaluronic acid matrix as a skin substitute*. Biomaterials, 2004. **25**(17): p. 3689-3698.
82. De Giglio, E., et al., *An innovative, easily fabricated, silver nanoparticle-based titanium implant coating: development and analytical characterization*. Analytical and bioanalytical chemistry, 2013. **405**(2-3): p. 805-816.
83. Holt, J., et al., *Decreasing bacterial colonization of external fixation pins via nitric oxide release coatings*. Journal of orthopaedic trauma, 2011. **25**(7): p. 432-437.

84. Chen, X., et al., *Dual action antibacterial TiO 2 nanotubes incorporated with silver nanoparticles and coated with a quaternary ammonium salt (QAS).* Surface and Coatings Technology, 2013. **216**: p. 158-165.
85. Kargupta, R., et al., *Coatings and surface modifications imparting antimicrobial activity to orthopedic implants.* Wiley Interdisciplinary Reviews: Nanomedicine and Nanobiotechnology, 2014. **6**(5): p. 475-495.
86. Verberne, M.C., et al., *Method for the extraction of the volatile compound salicylic acid from tobacco leaf material.* Phytochemical Analysis, 2002. **13**(1): p. 45-50.
87. Surjushe, A., R. Vasani, and D. Saple, *Aloe vera: a short review.* Indian journal of dermatology, 2008. **53**(4): p. 163-166.
88. Suresh, S., S. Gunasekaran, and S. Srinivasan, *Spectroscopic (FT-IR, FT-Raman, NMR and UV-Visible) and quantum chemical studies of molecular geometry, Frontier molecular orbital, NLO, NBO and thermodynamic properties of salicylic acid.* Spectrochimica Acta Part A: Molecular and Biomolecular Spectroscopy, 2014. **132**: p. 130-141.
89. Zhang, T., et al., *A novel naturally occurring salicylic acid analogue acts as an anti-inflammatory agent by inhibiting nuclear factor-kappaB activity in RAW264. 7 macrophages.* Molecular pharmaceutics, 2012. **9**(3): p. 671-677.
90. Griffin, J., et al., *Salicylic acid-derived poly (anhydride-ester) electrospun fibers designed for regenerating the peripheral nervous system.* Journal of Biomedical Materials Research Part A, 2011. **97**(3): p. 230-242.
91. Miguel, S.P., et al., *Thermoresponsive chitosan-agarose hydrogel for skin regeneration.* Carbohydrate polymers, 2014. **111**: p. 366-373.
92. Muzzarelli, R.A. and R. Rocchetti, *Determination of the degree of acetylation of chitosans by first derivative ultraviolet spectrophotometry.* Carbohydrate Polymers, 1985. **5**(6): p. 461-472.
93. Morgado, P.I., et al., *Poly (vinyl alcohol)/chitosan asymmetrical membranes: Highly controlled morphology toward the ideal wound dressing.* Journal of Membrane Science, 2014. **469**: p. 262-271.
94. Ouimet, M.A., et al., *Poly (anhydride-ester) and Poly (N-vinyl-2-pyrrolidone) Blends: Salicylic Acid-Releasing Blends with Hydrogel-Like Properties that Reduce Inflammation.* Macromolecular bioscience, 2015. **15**(3): p. 342-350.
95. Zhou, Y., et al., *Radiation synthesis and characterization of nanosilver/gelatin/carboxymethyl chitosan hydrogel.* Radiation Physics and Chemistry, 2012. **81**(5): p. 553-560.
96. Fei Liu, X., et al., *Antibacterial action of chitosan and carboxymethylated chitosan.* Journal of Applied Polymer Science, 2001. **79**(7): p. 1324-1335.
97. Minagawa, T., et al., *Effects of molecular weight and deacetylation degree of chitin/chitosan on wound healing.* Carbohydrate Polymers, 2007. **67**(4): p. 640-644.

98. Correia, T.R., et al., *A bi-layer electrospun nanofiber membrane for plasmid DNA recovery from fermentation broths*. Separation and Purification technology, 2013. **112**: p. 20-25.
99. Moros, E., et al., *Analysis of xanthophylls in corn by HPLC*. Journal of Agricultural and Food Chemistry, 2002. **50**(21): p. 5787-5790.
100. Sessa, D. and D. Palmquist, *Effect of heat on the adsorption capacity of an activated carbon for decolorizing/deodorizing yellow zein*. Bioresource technology, 2008. **99**(14): p. 6360-6364.
101. Chen, M., et al., *Role of fiber diameter in adhesion and proliferation of NIH 3T3 fibroblast on electrospun polycaprolactone scaffolds*. Tissue Engineering, 2007. **13**(3): p. 579-587.
102. Nath, S.D., et al., *Chitosan–hyaluronic acid polyelectrolyte complex scaffold crosslinked with genipin for immobilization and controlled release of BMP-2*. Carbohydrate polymers, 2015. **115**: p. 160-169.
103. Croisier, F. and C. Jérôme, *Chitosan-based biomaterials for tissue engineering*. European Polymer Journal, 2013. **49**(4): p. 780-792.
104. Anisha, B., et al., *Chitosan–hyaluronic acid/nano silver composite sponges for drug resistant bacteria infected diabetic wounds*. International journal of biological macromolecules, 2013. **62**: p. 310-320.
105. Saraiva, S.M., et al., *Synthesis and characterization of a photocrosslinkable chitosan-gelatin hydrogel aimed for tissue regeneration*. RSC Advances, 2015. **5**(78): p. 63478-63488.
106. Saithongdee, A., N. Praphairaksit, and A. Imyim, *Electrospun curcumin-loaded zein membrane for iron (III) ions sensing*. Sensors and Actuators B: Chemical, 2014. **202**: p. 935-940.
107. Diridollou, S., et al., *In vivo model of the mechanical properties of the human skin under suction*. Skin Research and technology, 2000. **6**(4): p. 214-221.
108. Silver, F.H., J.W. Freeman, and D. DeVore, *Viscoelastic properties of human skin and processed dermis*. Skin Research and Technology, 2001. **7**(1): p. 18-23.
109. Powell, H.M. and S.T. Boyce, *Engineered human skin fabricated using electrospun collagen–PCL blends: morphogenesis and mechanical properties*. Tissue Engineering Part A, 2009. **15**(8): p. 2177-2187.
110. Lee, J., et al., *The effect of gelatin incorporation into electrospun poly (l-lactide-co-ε-caprolactone) fibers on mechanical properties and cytocompatibility*. Biomaterials, 2008. **29**(12): p. 1872-1879.
111. Liang, Y., et al., *Heat treatment of electrospun Polyvinylidene fluoride fibrous membrane separators for rechargeable lithium-ion batteries*. Journal of Power Sources, 2013. **240**: p. 204-211.
112. Labet, M. and W. Thielemans, *Synthesis of polycaprolactone: a review*. Chemical Society Reviews, 2009. **38**(12): p. 3484-3504.

113. Liu, X. and P.X. Ma, *Polymeric scaffolds for bone tissue engineering*. Annals of biomedical engineering, 2004. **32**(3): p. 477-486.
114. Xiao, S.-C., et al., *The role of pores in acellular dermal matrix substitute*. Annals of burns and fire disasters, 2006. **19**(4): p. 192-195.
115. Loh, Q.L. and C. Choong, *Three-dimensional scaffolds for tissue engineering applications: role of porosity and pore size*. Tissue Engineering Part B: Reviews, 2013. **19**(6): p. 485-502.
116. Freyman, T., I. Yannas, and L. Gibson, *Cellular materials as porous scaffolds for tissue engineering*. Progress in Materials Science, 2001. **46**(3): p. 273-282.
117. Pavithra, D. and M. Doble, *Biofilm formation, bacterial adhesion and host response on polymeric implants—issues and prevention*. Biomedical Materials, 2008. **3**(3): p. 034003.
118. Priya, S.G., H. Jungvid, and A. Kumar, *Skin tissue engineering for tissue repair and regeneration*. Tissue Engineering Part B: Reviews, 2008. **14**(1): p. 105-118.
119. Jung, Y.C. and B. Bhushan, *Contact angle, adhesion and friction properties of micro-and nanopatterned polymers for superhydrophobicity*. Nanotechnology, 2006. **17**(19): p. 4970-4980.
120. Mittal, K.L., *Contact angle, wettability and adhesion*. Vol. 4. 2006: CRC Press.
121. Lin, J., et al., *Co-electrospun nanofibrous membranes of collagen and zein for wound healing*. ACS applied materials & interfaces, 2012. **4**(2): p. 1050-1057.
122. Alhusein, N., et al., *Killing bacteria within biofilms by sustained release of tetracycline from triple-layered electrospun micro/nanofibre matrices of polycaprolactone and poly (ethylene-co-vinyl acetate)*. Drug delivery and translational research, 2013. **3**(6): p. 531-541.
123. Chen, Y., et al., *Asymmetric polyurethane membrane with in situ-generated nano-TiO2 as wound dressing*. Journal of Applied Polymer Science, 2011. **119**(3): p. 1532-1541.
124. Elsner, J.J. and M. Zilberman, *Novel antibiotic-eluting wound dressings: An in vitro study and engineering aspects in the dressing's design*. Journal of tissue viability, 2010. **19**(2): p. 54-66.
125. Gunatillake, P.A. and R. Adhikari, *Biodegradable synthetic polymers for tissue engineering*. European cells & materials, 2003. **5**(1): p. 1-16.
126. Dai, N.-T., et al., *Composite cell support membranes based on collagen and polycaprolactone for tissue engineering of skin*. Biomaterials, 2004. **25**(18): p. 4263-4271.
127. Collins, M.N. and C. Birkinshaw, *Hyaluronic acid based scaffolds for tissue engineering—A review*. Carbohydrate polymers, 2013. **92**(2): p. 1262-1279.
128. Sun, Q.S., et al., *Comparison of cytocompatibility of zein film with other biomaterials and its degradability in vitro*. Biopolymers, 2005. **78**(5): p. 268-274.
129. Regier, M.C., et al., *Fabrication and characterization of DNA-loaded zein nanospheres*. Journal of nanobiotechnology, 2012. **10**(1): p. 44.

130. St Denis, T.G., et al., *Wound-Healing Properties of Chitosan and Its Use in Wound Dressing Biopharmaceuticals*. Chitosan-Based Systems for Biopharmaceuticals: Delivery, Targeting and Polymer Therapeutics, 2012: p. 429-450.
131. Hurtado-López, P. and S. Murdan, *Zein microspheres as drug/antigen carriers: a study of their degradation and erosion, in the presence and absence of enzymes*. Journal of microencapsulation, 2006. **23**(3): p. 303-314.
132. Ribeiro, M.P., et al., *Development of a new chitosan hydrogel for wound dressing*. Wound repair and regeneration, 2009. **17**(6): p. 817-824.
133. Nguyen, T.T.T., et al., *Porous core/sheath composite nanofibers fabricated by coaxial electrospinning as a potential mat for drug release system*. International journal of pharmaceutics, 2012. **439**(1): p. 296-306.
134. Davis, S.C. and R. Perez, *Cosmeceuticals and natural products: wound healing*. Clinics in dermatology, 2009. **27**(5): p. 502-506.
135. Qureshi, M., F. Khatoon, and S. Ahmed, *An Overview on Wounds Their Issues and Natural Remedies for Wound Healing*. Journal of physiology and biochemestry, 2015. **4**(3): p. 1000165.
136. Kim, W.-S., et al., *Wound healing effect of adipose-derived stem cells: a critical role of secretory factors on human dermal fibroblasts*. Journal of dermatological science, 2007. **48**(1): p. 15-24.
137. van Meerloo, J., G.J. Kaspers, and J. Cloos, *Cell sensitivity assays: the MTT assay*. Cancer cell culture: methods and protocols, 2011: p. 237-245.
138. Stevens, M.M. and J.H. George, *Exploring and engineering the cell surface interface*. Science, 2005. **310**(5751): p. 1135-1138.
139. Prithiviraj, B., et al., *Down regulation of virulence factors of Pseudomonas aeruginosa by salicylic acid attenuates its virulence on Arabidopsis thaliana and Caenorhabditis elegans*. Infection and immunity, 2005. **73**(9): p. 5319-5328.
140. Romanò, C.L., et al., *Antibiofilm agents and implant-related infections in orthopaedics: where are we?* Journal of Chemotherapy, 2013. **25**(2): p. 67-80.
141. Alem, M.A. and L.J. Douglas, *Effects of aspirin and other nonsteroidal anti-inflammatory drugs on biofilms and planktonic cells of Candida albicans*. Antimicrobial agents and chemotherapy, 2004. **48**(1): p. 41-47.
142. Lee, I.-Y., et al., *Structure-activity relationships of antitubercular salicylanilides consistent with disruption of the proton gradient via proton shuttling*. Bioorganic & medicinal chemistry, 2013. **21**(1): p. 114-126.
143. Kupferwasser, L.I., et al., *Acetylsalicylic acid reduces vegetation bacterial density, hematogenous bacterial dissemination, and frequency of embolic events in experimental Staphylococcus aureus endocarditis through antiplatelet and antibacterial effects*. Circulation, 1999. **99**(21): p. 2791-2797.

144. Kupferwasser, L.I., et al., *Salicylic acid attenuates virulence in endovascular infections by targeting global regulatory pathways in Staphylococcus aureus*. The Journal of clinical investigation, 2003. **112**(2): p. 222-233.

145. Jridi, M., et al., *Physical, structural, antioxidant and antimicrobial properties of gelatin–chitosan composite edible films*. International journal of biological macromolecules, 2014. **67**: p. 373-379.

146. Gómez-Estaca, J., et al., *Effects of gelatin origin, bovine-hide and tuna-skin, on the properties of compound gelatin–chitosan films*. Food Hydrocolloids, 2011. **25**(6): p. 1461-1469.

147. No, H., et al., *Applications of chitosan for improvement of quality and shelf life of foods: a review*. Journal of food science, 2007. **72**(5): p. R87-R100.

Appendix

- Fradique, R., Correia, T. R., Miguel, S. P., de Sá, K. D., Figueira, D. R., Mendonça, A. G., & Correia, I. J., *Production of new 3D scaffolds for bone tissue regeneration by rapid prototyping*. Journal of Materials Science: Materials in Medicine, 20016. *27*(4), 1-14.

J Mater Sci: Mater Med (2016)27:69
DOI 10.1007/s10856-016-5681-x

BIOMATERIALS SYNTHESIS AND CHARACTERIZATION

Original Research

Production of new 3D scaffolds for bone tissue regeneration by rapid prototyping

R. Fradique[1] · T. R. Correia[1] · S. P. Miguel[1] · K. D. de Sá[1] · D. R. Figueira[1] · A. G. Mendonça[1,2] · I. J. Correia[1]

Received: 5 August 2015 / Accepted: 27 January 2016

Abstract The incidence of bone disorders, whether due to trauma or pathology, has been trending upward with the aging of the worldwide population. The currently available treatments for bone injuries are rather limited, involving mainly bone grafts and implants. A particularly promising approach for bone regeneration uses rapid prototyping (RP) technologies to produce 3D scaffolds with highly controlled structure and orientation, based on computer-aided design models or medical data. Herein, tricalcium phosphate (TCP)/alginate scaffolds were produced using RP and subsequently their physicochemical, mechanical and biological properties were characterized. The results showed that 60/40 of TCP and alginate formulation was able to match the compression and present a similar Young modulus to that of trabecular bone while presenting an adequate biocompatibility. Moreover, the biomineralization ability, roughness and macro and microporosity of scaffolds allowed cell anchoring and proliferation at their surface, as well as cell migration to its interior, processes that are fundamental for osteointegration and bone regeneration.

R. Fradique and T. R. Correia have contributed equally to this work.

Electronic supplementary material The online version of this article (doi:10.1007/s10856-016-5681-x) contains supplementary material, which is available to authorized users.

✉ I. J. Correia
icorreia@fcsaude.ubi.pt; icorreia@ubi.pt

[1] CICS-UBI—Health Sciences Research Centre, University of Beira Interior, Av. Infante D. Henrique, 6200-506 Covilhã, Portugal

[2] Department of Chemistry, University of Beira Interior, R. Marquês d'Ávila e Bolama, 6201-001 Covilhã, Portugal

1 Introduction

Apart from traumatic events, the aging of the worldwide population has led to an increased prevalence of bone tissue diseases, with up to 2.2 million people needing surgery every year [1]. The currently available treatments for bone defects involve the use of bone grafts, particularly autografts, which present serious restrictions such as limited availability, induction of chronic pain and the inability to promote the complete recovery of the patient. To overcome this healthcare problem, a huge effort has been made on the topic of bone tissue engineering in order to create new therapeutic approaches [2]. Artificial bone implants produced from metals, ceramics, polymers and composites have been widely used in bone reconstruction and regeneration [3–10]. Three dimensional (3D) structures, known as scaffolds, constitute one example of these artificial implants and have been produced with materials such as hydroxyapatite (HA), tricalcium phosphate (TCP), poly(lactic-co-glycolic acid) (PLGA) or sodium alginate. Furthermore, scaffolds surfaces can be modified (surface coating, chemical treatment and polymerization) to improve bone healing [11], with some types of scaffolds being used for cell and growth factor delivery to the damaged tissues, while providing mechanical support during the tissue regeneration process [12].

Nowadays, the development of a bone substitute involves the optimization of several parameters, such as biocompatibility, manufacturing simplicity, mechanical requirements, osteoconductivity, osteoinductivity and, depending on the type of implant to be produced (permanent or temporary), its degradation rate, that in some cases must be synchronized with the rate of tissue regeneration [2, 12–17].

Several techniques have been described in literature as being suitable for producing bone replacements. Fiber

Published online: 17 February 2016

bonding [18, 19], freeze drying [20, 21], melting [22, 23], phase inversion [24, 25] and solvent casting [26, 27] are the most employed techniques for scaffolds production. However, some of them present several disadvantages, such as the use of toxic solvents, inability to create large structures with appropriate mechanical properties, absence of pore size control and a limited number of usable materials [28].

The latest advances in the area of computer technology allowed the development of rapid prototyping (RP) techniques that recently started to be used in the design of new 3D constructs aimed to be applied in the area of tissue engineering [29, 30]. So far, computer assisted design (CAD) models supported the manufacturing of highly reproducible 3D scaffolds [31]. To accomplish that, the 3D CAD models are replicated in a layer-by-layer routine, allowing scaffolds to be printed with different conformations and geometries, that may contribute for a significant improvement of scaffold's mechanical properties according to the demands of the damaged bone [32]. As an alternative, other researchers adapted a different strategy based on data collected from routine medical examinations, where the produced scaffolds were specifically tailored, i.e. produced with high anatomic accuracy, to fulfil the particular demands of the injured bone tissue [33–35]. Santos et al. used a 3D printer (Zprinter 310 Plus) to produce scaffolds that replicated the computer tomography data of a human hand [35].

Recently, our group used a Fab@Home plotter to produce TCP/alginate scaffolds with high accuracy, that were previously designed with CAD software [36]. This procedure was adopted taking into account the plotter's cost, versatility and capacity to replicate CAD models with control and reproducibility, in a short period of time [36, 37].

In this study, alginate and TCP were selected to reproduce the organic and inorganic components of the native bone matrix. TCP was used to mimic the mineral phase of the bone, due to its composition, high biocompatibility, bioactivity, great compressive strength osteoconductivity, and also by presenting an in vivo bio-resorption rate that fulfills bone regeneration demands [14, 38, 39]. However, as other ceramics, it possesses a brittle behavior. To overcome this bottleneck, two strategies were selected to improve the mechanical properties of the scaffolds: various ratios of TCP/alginate were used and scaffolds with different geometries were designed using CAD software.

Alginate is a natural polysaccharide derived from brown seaweeds composed of 1,4-linked D-mannuronic acid (M) and α-L-guluronic acid (G) residues [40–42], and is known by its ability to form stable hydrogels when ionically crosslinked with divalent cations (e.g. Ca^{2+},$Sr^{2+}$and Ba^{2+}) [40, 43]. In previous studies it has already been described the successful application of alginate in bone regeneration, either alone or in combination with other polymers and ceramics [36, 43–46].

2 Materials and methods

2.1 Materials

Amphotericin B, bovine serum albumin (BSA), cacodylate buffer (MW = 214.03 g/mol), calcein, calcium chloride, Dulbecco's modified Eagle medium: nutrient mixture F12 (DMEM-F12), ethylenediaminetetraacetic acid (EDTA), gentamicin, glutaraldehyde 25 % (v/v), L-glutamine, sodium alginate (MW = 120–190 kDa), trypan blue and trypsin were purchased from Sigma-Aldrich (Sintra, Portugal). Tricalcium phosphate (TCP) powder (MW = 310.20 g/mol) was obtained from Panreac® (Barcelona, Spain). 3-(4,5-dimethylthiazol-2-yl)-5-(3-carboxymethoxyphenyl)-2-(4-sulfophenyl)-2H tetrazolium reagent, inner salt (MTS) was bought from Promega (Madison, USA). Fetal bovine serum (FBS) was purchased from Biochrom AG (Berlin, Germany). Human osteoblast cells (406-05f) were obtained from Cell Applications, Inc. (San Diego, CA). 24 and 96-well plates were acquired from Orange Scientific (Braine L'Alleud, Belgium). Tris Base was obtained from Fischer Scientific (Lisbon, Portugal). Hoechst 33342® was acquired from Invitrogen (Carlsbad, CA).

2.2 Production of TCP/alginate composite scaffolds by RP

The 3D scaffolds were produced by RP using a Fab@Home plotter, as previously described [36]. TCP/alginate scaffolds were produced using prepared solutions of each compound in a proportion of 60/40 % (w/w), 70/30 % (w/w) and 80/20 % (w/w). Briefly, a 15 % (w/v) alginate solution was prepared by dissolving the polymer in double deionized and filtered water (obtained using a Milli-Q Advantage A10 ultrapure Water Purification System; resistivity = 18.2 MΩ/cm at 25 °C), with overnight agitation. The solution was then homogenized using an X10/25 Ultra-turrax (Ystral, Germany) for 30 min. Finally, TCP powder was added to the alginate solutions to obtain the specific ratios described above, and subsequently the samples were homogenized. Then, a 5 % $CaCl_2$ solution was added to the composite sample (in a 0.14:1 volume ratio of $CaCl_2$ to alginate), and alginate polymer chains got crosslinked leading to an increase of the solution's viscosity that is fundamental for scaffolds production [36]. The used 3D model was designed using CAD/CAM software (OpenSCAD version 2014.3, ©2009–2014 Marius Kintel and Clifford Wolf). The developed 3D model was composed of several layers angled at 45° with the underlying layer (0°–45°–90°–135°), as shown in Fig. 1. Briefly,

the file containing the scaffold model was converted and exported to STL format. Following, a syringe (10 cc Luer Lock) was filled with the composite solution for posterior extrusion. After the extrusion process, the scaffolds were maintained in a 5 % $CaCl_2$ bath for 24 h to achieve a complete crosslinking. Afterwards, the scaffolds were air-dried at RT and subsequently freeze-dried for 24 h.

2.3 Scanning electron microscopy analysis

Scanning electron microscopy (SEM) analysis of the scaffolds was performed in order to characterize the morphology, porosity and surface of the scaffolds. Samples were mounted onto aluminum stubs with Araldite glue and sputter-coated with gold using a Quorum Q150R ES sputter coater (Quorum Technologies, UK). The SEM images were then captured with different magnifications, at an acceleration voltage of 20 kV, using a Hitachi S-3400 N scanning electron microscope (Hitachi, Japan).

2.4 Attenuated total reflectance—fourier transform infrared spectroscopy analysis

To characterize the chemical composition of the scaffolds, Attenuated total reflectance-Fourier transform infrared spectroscopy (ATR-FTIR) was used. The spectra obtained for the samples represent the average of 128 scans, between 400 and 4000 cm^{-1}, with a spectral resolution of 4 cm^{-1}. All the samples were crushed to a powder, mounted on a diamond window, and the spectra were recorded with a Nicolet iS10 FTIR spectrophotometer (Thermo Scientific, Waltham, MA, USA). All the components used for scaffold production were also analyzed in pure state for a comparison to be made with the prepared samples [47].

2.5 Energy dispersive spectroscopic analysis

Energy dispersive spectroscopy (EDS) was used to perform the elemental composition analysis of the various scaffolds. The samples were placed on aluminum stubs, air-dried at RT and examined in an XFlash Detector 5010 (Bruker Nano, Germany).

2.6 Mechanical characterization of the scaffolds

In order to mimic the native environment found in vivo, all specimens of each sample were pre-soaked in culture medium for 4 h. Scaffold's dimensions were determined and then compression assays were performed to characterize the mechanical properties of the scaffolds using a Zwick® 1435 Material Prüfung (Ulm, Germany). A crosshead speed of 3 mm/min and a load cell of 5kN were used for analyzing five specimens of the different formulations in each assay.

The compressive strength (C_s) of each scaffold was calculated according to Eq. (1) [48].

$$C_s = \frac{F}{w * l} \tag{1}$$

where F is the load at the time of fracture, and w and l represent the width and length of the scaffold, respectively.

The Young modulus (YM) of each scaffold was calculated from the stress–strain relation, calculated by applying Eq. (2).

$$YM = \frac{C_s}{H_d} \tag{2}$$

where H_d stands for the height deformation at maximum load and C_s is the scaffold compressive strength. Average

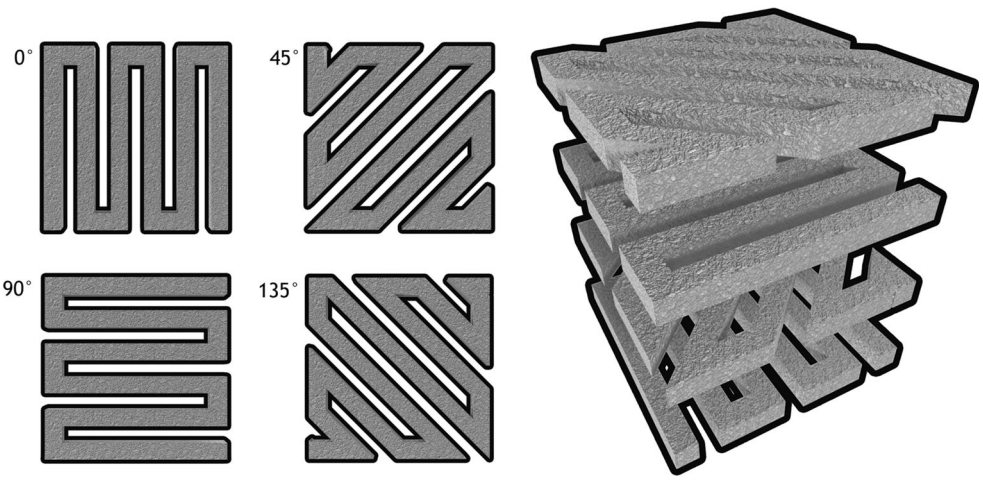

Fig. 1 Schematic overview of the layered structure of the model

values and standard deviations (S.D.) were determined for each sample.

2.7 Swelling studies

The swelling capacity of the scaffolds was determined through a method adapted from literature [43]. In brief, samples were immersed in Tris buffer (1 M, Ph 7.4), at 37 °C, for 2 days (n = 3). After absorbing the excess of Tris with filter paper, scaffolds were removed from the solution at predetermined intervals and weighed. Following this process, the samples were re-immersed in the swelling solution. The swelling ratio of the scaffolds was evaluated using Eq. (3).

$$Swelling\ ratio\ (\%) = \frac{W_t - W_0}{W_0} * 100 \quad (3)$$

where W_t is the final weight of the scaffolds and W_0 their initial weight.

2.8 Contact angle measurements

Contact angle measurements were performed using a OCAH 200 Contact Angle System (DataPhysics Instruments, Germany), operated in static mode at RT. This assay was performed using water as reference fluid [36]. For each sample, water drops were placed at various locations of the surface of the scaffold. The reported contact angles are the average of at least three measurements.

2.9 Evaluation of the porosity of the scaffolds

To determine the microporosity of the different scaffolds a liquid displacement method was used, according to the procedure previously reported [48]. In brief, scaffolds were weighed, immersed in absolute ethanol (EtOH) for 48 h, and weighed again. EtOH was chosen for its ability to penetrate throughout the scaffolds without causing shrinking or swelling of the matrix [49]. The porosity was then calculated by determining the amount of EtOH absorbed, through Eq. (4):

$$Porosity(\%) = \frac{W_w - W_d}{D_{ethanol} * V_{Scaffold}} * 100 \quad (4)$$

where W_w and W_d are the wet and dry weights of the scaffolds, respectively, $D_{ethanol}$ represents the density of EtOH at RT and $V_{scaffold}$ the volume of the wet scaffold. Five replicates of each scaffold were used, and the data represents the average values obtained.

2.10 Characterization of the degradation profile of the scaffolds

The degradation profile of the composite scaffolds was investigated through a method previously published. [50, 51] In brief, scaffolds were placed in 24-well plates, fully immersed in DMEM-F12 at 37 °C. At predetermined intervals, samples were removed, completely dried and weighted. The degradation percentage at each point was calculated through Eq. (5):

$$Weight\ loss\ (\%) = (\frac{W_i - W_t}{W_i}) * 100 \quad (5)$$

where *Wi* corresponds to the initial weight of the sample and *Wt* to the weight of the sample at time t.

2.11 In vitro biomineralization assay

The in vitro bioactivity of each scaffold was evaluated by submerging them in standard simulated body fluid (SBF), followed by incubation at 37 °C for 7, 14, and 21 days, according to a method previously described in literature [52]. The SBF solution had a similar ionic concentration to that found in human blood plasma (142.0 mM Na^+, 5 mM K^+, 1.5 mM Mg^{2+}, 2.5 mM Ca^{2+}, 147.8 mM Cl^-, 4.2 mM HCO_3^-, 1.0 mM HPO_4^{2-}, and 0.5 mM SO_4^{2-}), and a pH of 7.4 at 37 °C [53]. Three scaffolds of equal weight and shape were used. After each period of incubation, the scaffolds were removed and rinsed three times with deionised water to remove soluble inorganic ions. The deposition of calcium and phosphate ions on the composite surface was characterized by EDS.

2.12 Characterization of the biological properties of the scaffolds

2.12.1 Evaluation of cell viability and proliferation in the presence of the scaffolds

Human osteoblasts cells (hOB) were cultured in DMEM-F12, supplemented with 10 % heat inactivated FBS, amphotericin B (100 µg/mL) and gentamicin (100 µg/mL) in 75 cm^2 T-flasks. Cells were maintained in a humidified environment at 37 °C, with 5 % CO_2, until confluence was attained. Subsequently, cells were trypsinized with 0.18 % trypsin (1:250) and 5 mM EDTA, and centrifuged for 5 min. Prior to cell seeding, scaffolds were cut into pieces with appropriate sizes and placed into 96-well plates to be sterilized by UV irradiation for 30 min. Following, cells were seeded at a density of 10×10^3 cells per well, in order to evaluate cell viability and proliferation. The culture medium was replaced every 2 days until the end of the assay.

To evaluate the cytotoxic character of the 3D scaffolds, an MTS assay was performed at day 4 and 7 [36]. The metabolic activity of the cells was assessed by quantifying the metabolic conversion of MTS to formazan. Briefly, the medium in each well was replaced with a mixture of

100 µL of fresh culture medium and 20 µL of MTS/phenazine methosulfate (PMS) reagent solution, and then the plate was incubated for 4 h at 37 °C. Following the incubation period, the supernatant was transferred into a 96-well microplate and the fluorescence intensity measured at 492 nm, using a microplate reader (Anthos 2020, Biochrom, UK). Five replicates of each sample were used for each experimental condition. Cells cultured without materials were used as negative control (K^-) and cells cultured with EtOH (70 %) were used as positive control (K^+).

2.12.2 Scanning electron microscopy analysis

In order to evaluate the cellular behavior in the presence of the scaffolds, SEM analysis was performed according to the method previously described by Lee and Chow [54]. Briefly, the samples were washed at RT with sodium cacodylate buffer solution (0.1 M, pH 7.4), and then fixed for 30 min in a 2.5 % (v/v) glutaraldehyde in 0.1 M sodium cacodylate solution. Subsequently, samples were frozen in liquid nitrogen for 2 min and then freeze-dried for 2 h. SEM analysis was performed as described in Sect. 2.3.

2.12.3 Confocal laser scanning microscopy analysis

Confocal laser scanning microscopy (CLSM) was used to characterize the cell distribution within the 60/40 scaffold. This formulation was selected based on the results obtained herein. hOB nucleus were labelled with Hoescht 33342 (5 µg/mL) and seeded in the presence of the scaffolds (10×10^3 cells/scaffold), in µ-Slide 8-well Ibidi imaging plates (Ibidi GmbH, Germany). After 24 h, the scaffold was labelled with calcein (20 µg/mL) and confocal images were acquired. Imaging experiments were performed in a Zeiss LSM 710 laser scanning confocal microscope (Carl Zeiss AG, Germany), where consecutive z-stacks were acquired. The 3D reconstruction and image analysis were performed using Zeiss Zen 2010 software [36].

2.13 Statistical analysis

One-way analysis of variance (ANOVA), with the Newman–Keuls post hoc test was used for comparison of the different test groups. A p value lower than 0.05 ($p < 0.05$) was considered statistically significant. Data analysis was performed in GraphPad Prism v.6.0 software (Trial version, GraphPadSoftware, CA, USA).

3 Results and discussion

3.1 Morphological characterization of the produced scaffolds

Different approaches have been used in the area of regenerative medicine to answer the limitations of the currently available therapeutics. Among them, RP technologies have proven to be a precious tool in every stage of development, greatly improving the design decision process and the scaffold's mechanical properties.

In this work, composite scaffolds constituted by TCP and alginate were produced by RP, for mimicking the natural bone matrix properties (20–30 % organic, 70–80 % inorganic) [14, 17]. To do so, an optimization of the scaffold's production parameters was done. Figure 2 presents the CAD model used, as well as one of the scaffolds printed by RP. The designed model is a 13 mm × 13 mm × 13 mm cube, with a porous structure. As described, it is composed by layers rotated 45° in relation to the underlying layer (0°–45°–90°–135°), in order to increase its mechanical resistance.

Alginate was selected for scaffolds production due to its capacity to act as temporary extracellular matrix (ECM) for bone cells. In addition, the possibility of controlling the degradation rate of this polymer is of great importance for tailoring the properties of the scaffold [40, 41]. On the other hand, TCP was chosen due to its resemblance with the natural ceramic component of bone tissue, increased biocompatibility, low cost, osteoconductivity and enhanced mechanical resistance [2, 38, 55]. Furthermore, the combination of these materials has already been shown to improve cell adhesion and proliferation, with the potential to allow cell growth and differentiation before implantation [36, 56]. Macroscopic images of the produced scaffolds are presented in Fig. 3.

Through the analysis of the images shown in Fig. 3 it is possible to observe that the TCP content had a direct effect on the scaffold's structure, namely on the scaffold's dimensions, decreasing the shrinking endured. It was previously described that alginate gels and scaffolds suffer shrinkage during the drying process [57]. Other researchers have also reported that the presence of solid fillers, such as ceramic particles, in an alginate solution has a direct effect on the volume loss during the drying process [58]. It was noticed that the compression of the polymeric matrix leads to the compression of the TCP particles against each other. Herein, it was verified that the scaffolds containing the highest percentage of TCP suffered less shrinkage, since the amount of incompressible ceramic particles limits the shrinking that

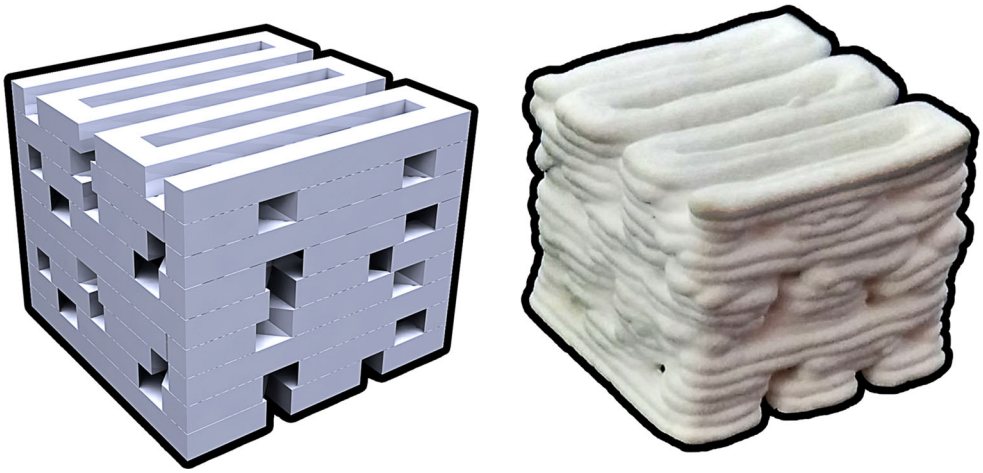

Fig. 2 Images of the CAD model used (*left*) and of the final printed model (*right*)

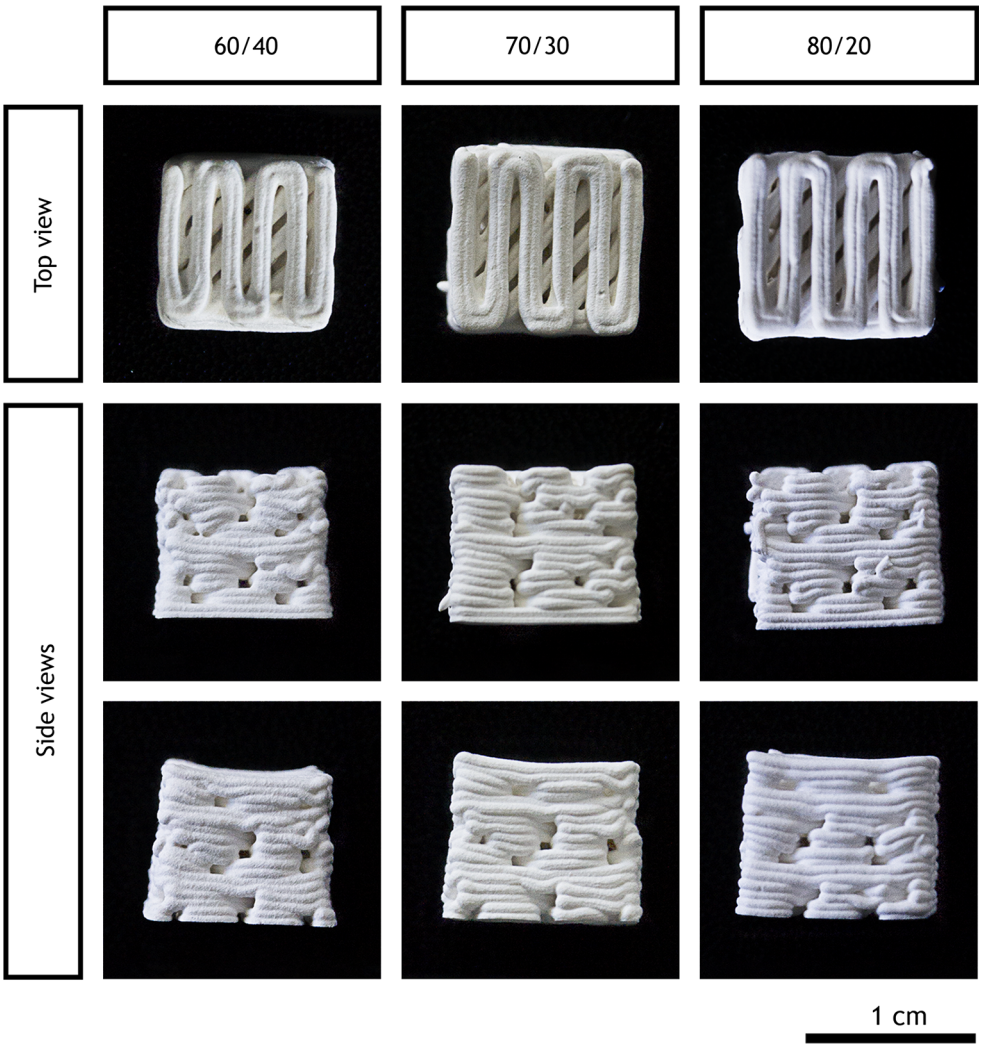

Fig. 3 Representative macroscopic images of the different produced scaffolds

scaffolds can suffer. This is important, since an excess shrinking can greatly affect the scaffold's porosity and its mechanical properties.

Furthermore, the scaffolds surface morphology has a great effect on cell adhesion and, consequently, on the successful material implantation. Figure 4 shows SEM

images acquired to characterize the surface morphology of the produced scaffolds.

Through the analysis of Fig. 4 it is possible to verify that all the scaffolds presented similar surface characteristics, with high roughness and irregularities. It has been previously described that the surface roughness of a scaffold has a great effect on protein adsorption and cell adhesion, upon scaffold implantation [59, 60]. On irregular surfaces, human osteoblasts present increased metabolism and ECM production, due to an increased contact surface available for promoting adhesion contact points [6].

3.2 Characterization of the physicochemical properties of the scaffolds

3.2.1 ATR-FTIR analysis

An ATR-FTIR analysis was performed to evaluate the chemical composition of the scaffolds. The ATR-FTIR spectra of the raw materials and of the produced scaffolds are presented in Fig. 5.

The ATR-FTIR spectrum of TCP presents a peak at 1020 cm^{-1} (I), that is characteristic of a P=O stretch vibration, thus revealing the presence of the inorganic phosphate components of TCP [35]. This peak is also present on the spectra of the produced scaffolds, with an intensity that is proportional to the ceramic content present in each sample. The ATR-FTIR spectrum of sodium alginate powder presented two peaks at 1400 and 1600 cm^{-1} (II), corresponding to the C=O stretching of the carboxylate group [61]. In addition, a stretching vibration correspondent to the O–H bonds of alginate appeared in the range 3000–3600 cm^{-1} (III) [62]. These peaks were also present in the spectra of the different scaffolds, without perceptible variations among them.

3.2.2 Energy dispersive spectroscopy analysis

The elemental composition of the scaffolds was also characterized through EDS analysis, to elucidate the chemical composition of the scaffolds. Table 1 shows that samples with a higher amount of ceramic component have a greater percentage of phosphate and calcium. Such results are in agreement with the expectations, since these are the

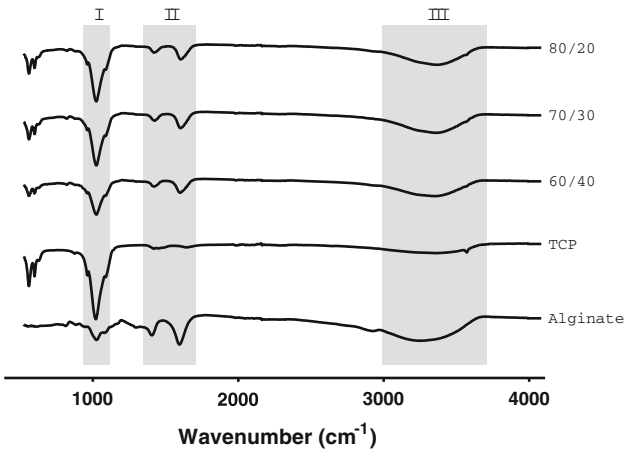

Fig. 5 ATR-FTIR analysis of the alginate, TCP and TCP/alginate scaffolds (80/20, 70/30, and 60/40)

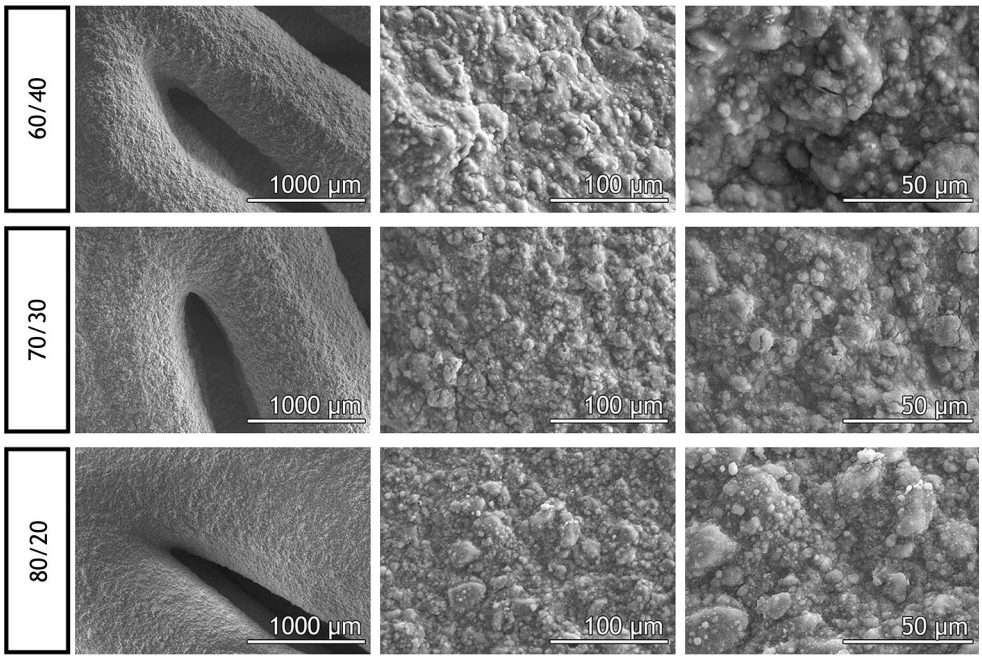

Fig. 4 SEM images showing the morphology of the different produced scaffolds at different magnifications

Table 1 EDS analysis of the produced TCP/alginate scaffolds (60/40, 70/30 and 80/20) and the Ca/P ratios determined for the produced scaffolds

	P	Ca	Ca/P ratio
60/40	2.89	8.48	2.93
70/30	4.35	9.42	2.17
80/20	4.71	10.28	2.18

main components of TCP. In addition, the Ca/P ratios of the produced scaffolds are within the range described for native trabecular bone (2.33 ± 0.34) [63].

3.2.3 *Characterization of the mechanical properties of the scaffolds*

A scaffold to be used in bone tissue regeneration must present adequate resistance and flexibility. The mechanical behavior of the produced scaffolds was analyzed by determining the resistance to compression and the Young's modulus (Fig. 6).

Previous studies described that 3D constructs with an increased ceramic content have an increased brittleness and, consequently, a lower mechanical resistance [64, 65]. The high TCP content of the 70/30 and 80/20 scaffolds produced here led to an increased brittleness and fragility, characteristic of pure ceramic scaffolds [65]. Furthermore, in a biphasic solution, the polymeric component (alginate in this case) creates a bone like structure by trapping the ceramic particles [66].

In this study, to simulate the mechanical performance of the scaffolds under in vivo conditions, their mechanical properties were evaluated in wet conditions. Figure 6 shows the results obtained for the different samples in the compression strength and modulus young assays. The 60/40 sample showed a compressive strength of 20 MPa, the 70/30 a value of ~10 MPa and the 80/20 a value of 2 MPa. Such results are agreement with previous studies [65], where an increase in ceramic content leads to a lower compressive strength. Although, all the produced specimens presented a compressive strength similar to that displayed by trabecular bone (0.5–15 MPa). Based on the collected data it can be inferred that these type of scaffolds have the required mechanical properties to be applied in non-load bearing sites.

Moreover, a large mismatch of the elastic modulus of the implant and that of the native bone tissue can be responsible for stress shielding, and consequently, result in a limited scaffold osteointegration [67]. In this context, the Young modulus of the three specimens was also investigated in wet conditions, showing that the scaffolds with the lowest ceramic content (60/40) presented the highest modulus (70 MPa), while the 70/30 and 80/20 formulations presented 40 and 9 MPa, respectively. In comparison with the Young modulus characteristic of cancellous bone(100–200 MPa [15]), the 60/40 scaffolds had the closest value.

Therefore, taking into account these results the 60/40 scaffolds are the most promising candidates to be applied in bone regeneration, since they closely reproduce the native bone matrix structure, while they are able to present mechanical properties similar to those of trabecular bone tissue.

3.2.4 *Swelling studies*

The swelling capacity of a scaffold can have a deep impact on its biocompatibility and biologic performance. In fact, scaffolds with an increased capacity to absorb water promote protein adsorption and cell adhesion, leading to a reduced immune response from the host [68]. The swelling profiles obtained for the produced scaffolds are presented in Fig. 7a. All scaffolds presented a rapid swelling in the first minutes and then stabilized after about 10 h of immersion in Tris buffer (1 M, pH 7.4).

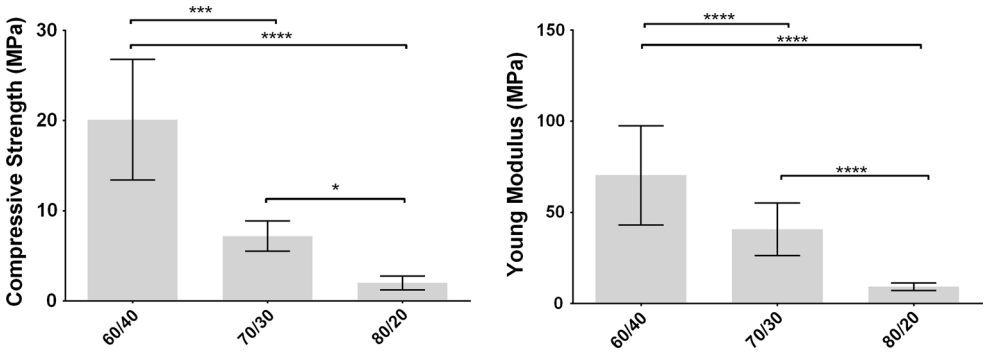

Fig. 6 Characterization of the compressive strength (*left*) and young modulus (*right*) of the scaffolds. Statistical analysis of the results was performed using one-way ANOVA with Newman–Keuls post hoc test (****$p \leq 0.0001$)

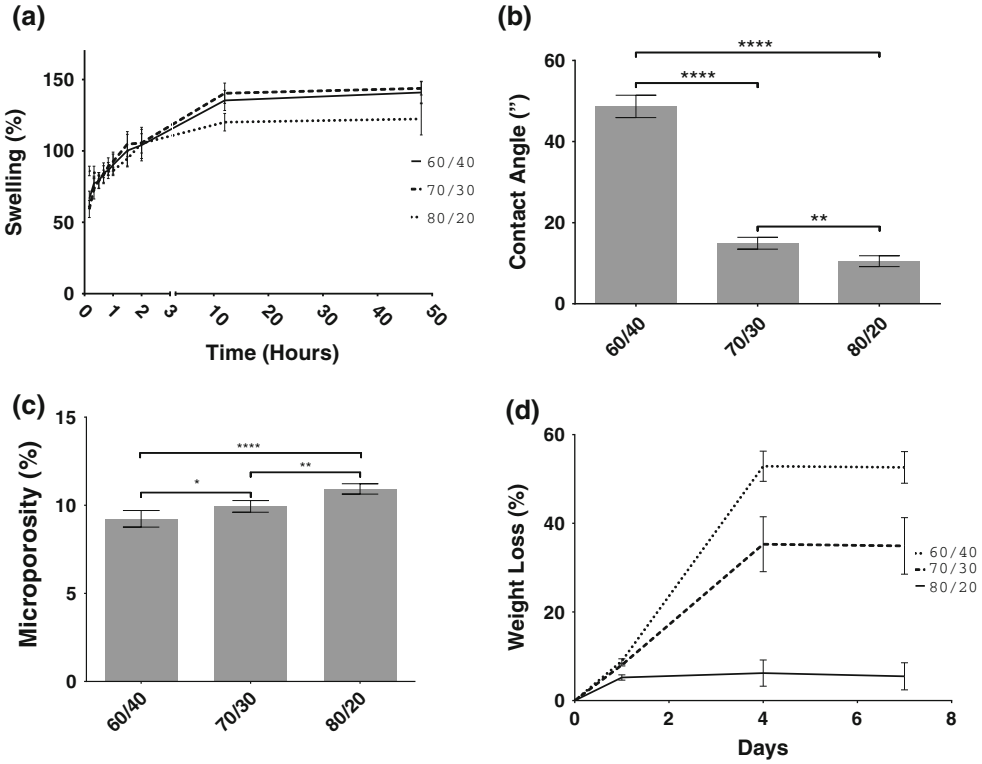

Fig. 7 Characterization of the swelling profile of the scaffolds (**a**); contact angle of the different produced scaffolds (**b**); statistical analysis of the results was performed using one-way ANOVA with a Newman–Keuls test (**$p \leq 0.01$, ****$p \leq 0.0001$); scaffold's microporosity (**c**); Statistical analysis of the data was performed using one-way ANOVA with a Newman–Keuls test (*$p \leq 0.05$, **$p \leq 0.01$, ****$p \leq 0.0001$, n = 5); and degradation profile of the scaffolds (**d**)

Valente et al. have already reported that a polymeric network composed of alginate is capable of absorbing large quantities of water by filling its void regions [43]. This effect was also confirmed in this study, where the scaffolds containing higher amounts of alginate presented a higher swelling ratio.

3.2.5 *Contact angle analysis*

In order to evaluate the hydrophilic character of the scaffolds, the contact angles were determined, as can be observed in Fig. 7b. It is possible to perceive that all the scaffolds presented a hydrophilic character, with contact angles below 70°. The 60/40 scaffolds showed a moderated hydrophilic character ($\approx$50°) while the 70/30 and 80/20 presented an almost superhydrophilic character ($\approx$20°). Hu et al. previously reported a direct correlation between the increase in the TCP content of the scaffolds and its hydrophilic character [69]. Scaffolds with moderate wettability improve cell attachment and growth, since their surfaces have preferential adsorption of cell-adhesive proteins [69, 70].

3.2.6 *Scaffolds porosity evaluation*

The microporosity of the scaffolds was determined by a liquid displacement method, using ethanol as displacement fluid. Figure 7c shows that the scaffolds with highest TCP content presented the highest porosity values (>10 % porosity). During the drying process the scaffolds suffer shrinking, which is responsible for the compression of the polymeric matrix. In this stage, the scaffolds with high ceramic content present more incompressible particles, thus limiting the amount of shrinkage that they can suffer, and consequently displaying an increased porosity [35, 36].

These results corroborate the mechanical resistance data obtained. Porosity and density are inversely proportional, and are closely related to the mechanical resistance of a scaffold [71]. Therefore, the most resistant scaffolds are the denser, as can be observed in Fig. 7c.

The porosity values obtained for the produced scaffolds are more similar to that of compact bone (3 %), than those displayed by trabecular bone (80 %) [72]. However, this lack of microporosity is balanced by a regular and sufficient macroporosity, as can be observed in Fig. 4. This macroporosity allows tissue ingrowth and osteointegration, and also facilitates the exchange of nutrients and metabolites from the interior of the scaffolds.

3.2.7 *Characterization of the degradation profile of the scaffolds*

The degradation rate of the scaffolds should be compatible with the time needed to occur new bone formation, in order for the scaffold be replaced during the regeneration process without affecting the mechanical stability of the tissue, at

the injured site [73]. The degradation profile of the produced scaffolds is presented in Fig. 7d. The results obtained showed that the scaffolds present a degradation profile dependent on its relative alginate content, with those containing a higher percentage of the polymer enduring a greater loss of mass. Under in vivo conditions, alginate depolymerizes by spontaneous alkaline elimination of its glycosidic linkages. Moreover, this polymer can also suffer disintegration by gradual exchange of calcium ions with sodium, reversing the gelling process [40]. On the other hand, TCP can suffer cell-mediated degradation when implanted in vivo, being solubilized while new tissue formation occurs [74].

Nonetheless, none of the scaffolds produced here lost more than 60 % of its mass, and all of them stabilized after 4 days, which is compatible with their application in bone tissue regeneration.

3.3 In vitro biomineralization assay

The in vitro mineralization ability of the composite scaffolds was studied using an SBF assay (Fig. 8). The obtained results revealed that calcium and phosphate content of the scaffolds increased along time. In addition, this increase was more pronounced for the formulations with higher TCP content. As previously described, TCP is a bioactive ceramic capable of inducing mineralization at the surface of the scaffolds, increasing their biointegration [52, 75], and consequently the bone regeneration process [75].

3.4 Characterization of the biological properties of the scaffolds

In vitro studies were performed to study the cytotoxic profile of the scaffolds. Human osteoblast cells were cultured in contact with the scaffolds for up to 7 days, and their viability assessed at days 4 and 7. The optical images acquired at the mentioned time points demonstrated that cells were able to proliferate in the presence of the composite scaffolds (please see Figure S1 for further details) and in the negative control. In the positive control, dead cells with their characteristic spherical shape were observed. To further characterize the cellular adhesion on the surface of the scaffolds, SEM images were also acquired (Fig. 9a).

As previously demonstrated, scaffolds showed a surface with high roughness, irregularities and a hydrophilic character that allowed cell adhesion. In fact, it is possible to observe that the cells were able to adhere to the surface of the material after 24 h of being seeded. Moreover, after 7 days, most cells had spread throughout the entire surface of the scaffold, and a cell layer was observed, demonstrating that all the scaffolds presented a suitable surface for cell adhesion and proliferation.

The biocompatibility of the scaffolds was further evaluated through an MTS assay (Fig. 9b). The results obtained in the MTS assay show that the cells remained viable after 4 and 7 days in the presence of all the produced scaffolds, indicating that all scaffolds provide an appropriate environment for cell adhesion and proliferation. The 60/40 formulation presented the highest cellular viability, which may be explained by their increased alginate content [43, 45]. Moreover, this formulation is the one that better reproduce the bone native constitution, further enhancing cell proliferation. These results can also be attributed to the osteogenic potential of TCP, which creates a layer that is similar to apatite on the surface of the material, due to its interaction with the surrounding medium [76].

CLSM analysis was performed 24 h after osteoblasts being seeded in contact with the 60/40 scaffold (Fig. 9c). This formulation was selected based on the previously achieved results. A 3D reconstruction image is presented in Fig. 9c_1, c_2, showing that the osteoblasts were able to adhere and proliferate in the tested formulation. Such highlights its biocompatibility and appropriate physicochemical properties. Moreover, the analysis of the orthogonal slices (Fig. 9c_3) and colour coded depth analysis (Fig. 9c_4) of 60/40 scaffold showed that osteoblasts migrate to the interior of the scaffold, with some cells being observed between 5 and 20 μm within the structure

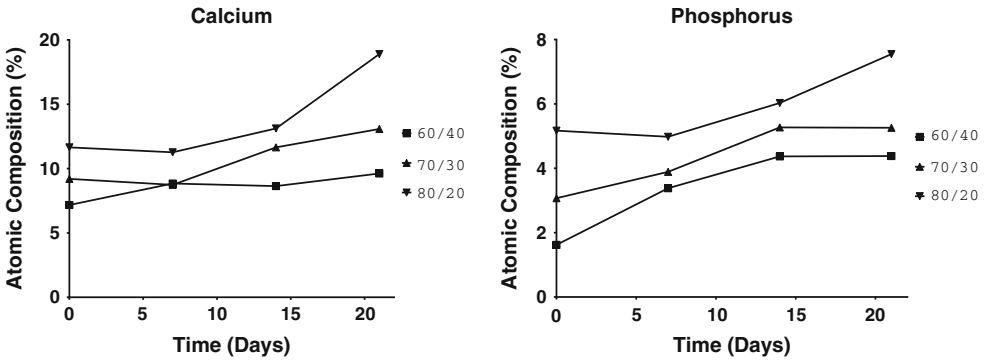

Fig. 8 EDS analysis of the different scaffolds after 7, 14 and 21 days in SBF

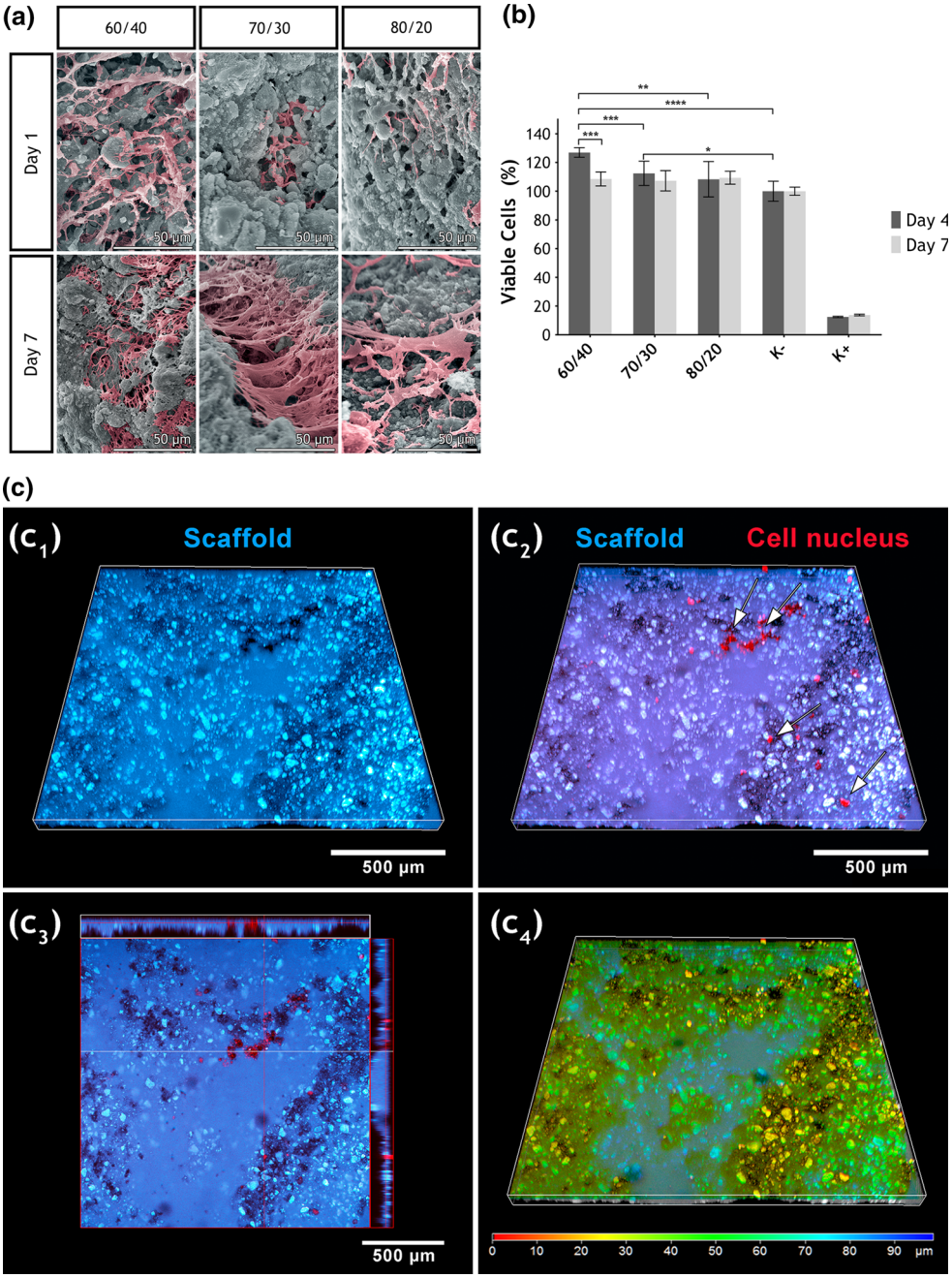

Fig. 9 Characterization of the biological properties of the scaffolds. **a** SEM images of hOB in the presence of the scaffolds; **b** evaluation of hOB viability when cultured in contact with the different scaffolds after 4 and 7 days; live cells (K−); dead cells (K+). Each result is the mean ± standard deviation of the mean of at least three independent experiments. Statistical analysis was performed using one-way ANOVA with Newman–Keuls post hoc test (*$p < 0.05$, **$p \leq 0.01$, ***$p \leq 0.001$, ****$p \leq 0.0001$); **c** 3D reconstruction images (*c1* and *c2*), orthogonal projections (*c3*), and colour coded depth analysis (*c4*) of cells in contact with the 60/40 TCP/alginate scaffold (*red* 0 µm, *blue* 90 µm). *Arrows* show the presence of cells (Color figure online)

of the scaffold. This cellular colonization of the structure will eventually allow the filling of the bone defect with new bone matrix, while the scaffold is biodegraded, thus leading to the restoring of the structure and functions of the native tissue.

4 Conclusion

The huge demand of new therapeutic approaches for bone regeneration triggered the development of different studies. Herein, scaffolds with different ratios of TCP and alginate were successfully produced using a Fab@Home. Besides optimizing the ratios of TCP/alginate for scaffolds manufacture, authors also used CAD software to further improve the mechanical characteristics of the 3D constructs. The compression and young modulus of the different produced scaffolds were characterized and those with 60/40 of TCP and alginate were selected as the best formulation. The results obtained revealed that the properties of these scaffolds matched the standard values for compression and have a similar Young modulus of the trabecular bone. In addition, the hydrophilic character of the produced scaffolds was also investigated. The 60/40 formulation showed

a moderately hydrophilic character ($\approx 50°$) while the others presented a superhydrophilic character ($\approx 20°$). The moderately hydrophilic behaviour displayed by the 60/40 structures allows protein adhesion at the surface of the materials, which is essential for cell adhesion and proliferation. Moreover, the biomineralization ability, roughness and macro and microporosity of scaffolds also contributed for cell anchoring and proliferation at their surface, as well as cell migration to its interior. These processes are fundamental for osteointegration and bone regeneration. Furthermore, the application of RP technologies for the production of the scaffolds can provide a great contribution to personalized therapy, since CAD tools can be used to design 3D structures that fulfil patient requirements and contribute to decrease the healing time. Encapsulation of cells and bioactive molecules in the produced scaffolds can also be hypothesized in a future of work, since no hazard agent is used during the scaffolds manufacture.

Acknowledgments Authors would like to acknowledge funding from FEDER (POCI-COMPETE 2020, project number 007491), Portuguese Science Foundation (FCT) (UID/Multi/00709) and QREN (Programa Mais Centro) (CENTRO-07-0224-FEDER-002014).

References

1. Giannoudis PV, Dinopoulos H, Tsiridis E. Bone substitutes: an update. Injury. 2005;36(Suppl 3):S20–7. doi:10.1016/j.injury.2005.07.029.
2. O'Brien FJ. Biomaterials & scaffolds for tissue engineering. Mater Today. 2011;14(3):88–95. doi:10.1016/S1369-7021(11)70058-X.
3. Bobe K, Willbold E, Morgenthal I, Andersen O, Studnitzky T, Nellesen J, et al. In vitro and in vivo evaluation of biodegradable, open-porous scaffolds made of sintered magnesium W4 short fibres. Acta Biomater. 2013;9(10):8611–23.
4. Rai R, Keshavarz T, Roether JA, Boccaccini AR, Roy I. Medium chain length polyhydroxyalkanoates, promising new biomedical materials for the future. Mater Sci Eng, R. 2011;72(3):29–47.
5. He J, Huang T, Gan L, Zhou Z, Jiang B, Wu Y, et al. Collagen-infiltrated porous hydroxyapatite coating and its osteogenic properties: in vitro and in vivo study. J Biomed Mater Res Part A. 2012;100(A(7)):1706–15.
6. Chiara G, Letizia F, Lorenzo F, Edoardo S, Diego S, Stefano S, et al. Nanostructured biomaterials for tissue engineered bone tissue reconstruction. Int J Mol Sci. 2012;13(1):737–57.
7. Xie M, Olderøy MO, Zhang Z, Andreassen JP, Strand BL, Sikorski P. Biocomposites prepared by alkaline phosphatase mediated mineralization of alginate microbeads. RSC Adv. 2012;2(4):1457–65.
8. Wu S, Liu X, Yeung KWK, Hu T, Xu Z, Chung JCY, et al. Hydrogen release from titanium hydride in foaming of orthopedic NiTi scaffolds. Acta Biomater. 2011;7(3):1387–97.
9. Alvarez K, Nakajima H. Metallic Scaffolds for Bone Regeneration. Materials. 2009;2(3):790–832.
10. Li Z, Gu X, Lou S, Zheng Y. The development of binary Mg-Ca alloys for use as biodegradable materials within bone. Biomaterials. 2008;29(10):1329–44.
11. Wu S, Liu X, Yeung KW, Liu C, Yang X. Biomimetic porous scaffolds for bone tissue engineering. Mater Sci Eng. 2014;80:1–36.
12. Malda J, Visser J, Melchels FP, Jüngst T, Hennink WE, Dhert WJA, et al. 25th anniversary article: engineering hydrogels for biofabrication. Adv Mater. 2013;25(36):5011–28. doi:10.1002/adma.201302042.
13. Frohlich M, Grayson W, Wan L, Marolt D, Drobnic M, Vunjak-Novakovic G. Tissue engineered bone grafts: biological requirements, tissue culture and clinical relevance. Curr Stem Cell Res Ther. 2008;3(4):254–64. doi:10.2174/157488808786733962.
14. Gaalen SV, Kruyt M, Meijer G, Mistry A, Mikos A, Beucken JVD, et al. Tissue engineering of bone. In: Blitterswijk CV, Thomsen P, Lindahl A, Hubbell J, Williams DF, Cancedda R, et al., editors. Tissue engineering. Burlington: Academic Press; 2008. p. 559–610.
15. Bose S, Roy M, Bandyopadhyay A. Recent advances in bone tissue engineering scaffolds. Trends Biotechnol. 2012;30(10):546–54.
16. Ma PX. Biomimetic materials for tissue engineering. Adv Drug Deliv Rev. 2008;60(2):184–98. doi:10.1016/j.addr.2007.08.041.
17. Kneser U, Schaefer DJ, Polykandriotis E, Horch RE. Tissue engineering of bone: the reconstructive surgeon's point of view. J Cell Mol Med. 2006;10(1):7–19. doi:10.1111/j.1582-4934.2006.tb00287.x.
18. Mikos AG, Bao Y, Cima LG, Ingber DE, Vacanti JP, Langer R. Preparation of poly(glycolic acid) bonded fiber structures for cell attachment and transplantation. J Biomed Mater Res. 1993;27(2):183–9. doi:10.1002/jbm.820270207.
19. Tuzlakoglu K, Bolgen N, Salgado AJ, Gomes ME, Piskin E, Reis RL. Nano- and micro-fiber combined scaffolds: a new architecture for bone tissue engineering. J Mater Sci. 2005;16(12):1099–104. doi:10.1007/s10856-005-4713-8.
20. Deville S, Saiz E, Tomsia AP. Freeze casting of hydroxyapatite scaffolds for bone tissue engineering. Biomaterials. 2006;27(32):5480–9. doi:10.1016/j.biomaterials.2006.06.028.
21. Kim H-W, Knowles JC, Kim H-E. Hydroxyapatite and gelatin composite foams processed via novel freeze-drying and crosslinking for use as temporary hard tissue scaffolds. J Biomed Mater Res, Part A. 2005;72A(2):136–45. doi:10.1002/jbm.a.30168.
22. Gomes ME, Ribeiro AS, Malafaya PB, Reis RL, Cunha AM. A new approach based on injection moulding to produce biodegradable starch-based polymeric scaffolds: morphology, mechanical and degradation behaviour. Biomaterials. 2001;22(9):883–9. doi:10.1016/S0142-9612(00)00211-8.
23. Mondrinos MJ, Dembzynski R, Lu L, Byrapogu VKC, Wootton DM, Lelkes PI, et al. Porogen-based solid freeform fabrication of polycaprolactone–calcium phosphate scaffolds for tissue engineering. Biomaterials. 2006;27(25):4399–408. doi:10.1016/j.biomaterials.2006.03.049.
24. Duarte ARC, Mano JF, Reis RL. Dexamethasone-loaded scaffolds prepared by supercritical-assisted phase inversion. Acta Biomater. 2009;5(6):2054–62. doi:10.1016/j.actbio.2009.01.047.
25. Tsivintzelis I, Pavlidou E, Panayiotou C. Porous scaffolds prepared by phase inversion using supercritical CO2 as antisolvent: i. Poly(l-lactic acid). J Supercrit Fluids. 2007;40(2):317–22. doi:10.1016/j.supflu.2006.06.001.
26. Suh SW, Shin JY, Kim J, Kim J, Beak CH, Kim DI, et al. Effect of different particles on cell proliferation in polymer scaffolds using a solvent-casting and particulate leaching technique. ASAIO J. 2002;48(5):460–4.
27. Sin D, Miao X, Liu G, Wei F, Chadwick G, Yan C, et al. Polyurethane (PU) scaffolds prepared by solvent casting/particulate leaching (SCPL) combined with centrifugation. Mater Sci Eng C. 2010;30(1):78–85. doi:10.1016/j.msec.2009.09.002.
28. Salgado AJ, Coutinho OP, Reis RL. Bone tissue engineering: state of the art and future trends. Macromol Biosci. 2004;4(8):743–65. doi:10.1002/mabi.200400026.

29. Daniel LC, Jeffrey IL, Lawrence JB, Hod L. Additive manufacturing for in situ repair of osteochondral defects. Biofabrication. 2010;2(3):035004.
30. Malone E, Lipson H. Fab@Home: the personal desktop fabricator kit. Rapid Prototyp J. 2007;13(4):245–55. doi:10.1108/13552540710776197.
31. Fedorovich NE, Schuurman W, Wijnberg HM, Prins H-J, van Weeren PR, Malda J, et al. Biofabrication of osteochondral tissue equivalents by printing topologically defined, cell-laden hydrogel scaffolds. Tissue Eng Part C. 2011;18(1):33–44. doi:10.1089/ten.tec.2011.0060.
32. Shaffer S, Yang K, Vargas J, Di Prima MA, Voit W. On reducing anisotropy in 3D printed polymers via ionizing radiation. Polymer. 2014;55(23):5969–79.
33. Martínez-Vázquez FJ, Perera FH, Miranda P, Pajares A, Guiberteau F. Improving the compressive strength of bioceramic robocast scaffolds by polymer infiltration. Acta Biomater. 2010;6(11):4361–8. doi:10.1016/j.actbio.2010.05.024.
34. Hockaday LA, Kang KH, Colangelo NW, Cheung PYC, Duan B, Malone E, et al. Rapid 3D printing of anatomically accurate and mechanically heterogeneous aortic valve hydrogel scaffolds. Biofabrication. 2012;4(3):035005.
35. Santos CFL, Silva AP, Lopes L, Pires I, Correia IJ. Design and production of sintered β-tricalcium phosphate 3D scaffolds for bone tissue regeneration. Mater Sci Eng. 2012;32(5):1293–8. doi:10.1016/j.msec.2012.04.010.
36. Diogo GS, Gaspar VM, Serra IR, Fradique R, Correia IJ. Manufacture of β-TCP/alginate scaffolds through a Fab@home model for application in bone tissue engineering. Biofabrication. 2014;6(2):025001. doi:10.1088/1758-5082/6/2/025001.
37. Kang KH, Hockaday LA, Butcher JT. Quantitative optimization of solid freeform deposition of aqueous hydrogels. Biofabrication. 2013;5(3):035001.
38. Rezwan K, Chen QZ, Blaker JJ, Boccaccini AR. Biodegradable and bioactive porous polymer/inorganic composite scaffolds for bone tissue engineering. Biomaterials. 2006;27(18):3413–31. doi:10.1016/j.biomaterials.2006.01.039.
39. Choi D, Kumta PN. Mechano-chemical synthesis and characterization of nanostructured β-TCP powder. Mater Sci Eng C. 2007;27(3):377–81. doi:10.1016/j.msec.2006.05.035.
40. Andersen T, Strand BL, Formo K, Alsberg E, Christensen BE. Chapter 9 Alginates as biomaterials in tissue engineering. Carbohydrate chemistry, vol. 37. Cambridge: The Royal Society of Chemistry; 2012. p. 227–58.
41. Augst AD, Kong HJ, Mooney DJ. Alginate hydrogels as biomaterials. Macromol Biosci. 2006;6(8):623–33. doi:10.1002/mabi.200600069.
42. Bonino CA, Krebs MD, Saquing CD, Jeong SI, Shearer KL, Alsberg E, et al. Electrospinning alginate-based nanofibers: from blends to crosslinked low molecular weight alginate-only systems. Carbohydr Polym. 2011;85(1):111–9. doi:10.1016/j.carbpol.2011.02.002.
43. Valente JFA, Valente TAM, Alves P, Ferreira P, Silva A, Correia IJ. Alginate based scaffolds for bone tissue engineering. Mater Sci Eng C. 2012;32(8):2596–603. doi:10.1016/j.msec.2012.08.001.
44. Lima AC, Batista P, Valente TA, Silva AS, Correia IJ, Mano JF. Novel methodology based on biomimetic superhydrophobic substrates to immobilize cells and proteins in hydrogel spheres for applications in bone regeneration. Tissue Eng Part A. 2013;19(9–10):1175–87.
45. Li Z, Ramay HR, Hauch KD, Xiao D, Zhang M. Chitosan–alginate hybrid scaffolds for bone tissue engineering. Biomaterials. 2005;26(18):3919–28. doi:10.1016/j.biomaterials.2004.09.062.
46. Lin H-R, Yeh Y-J. Porous alginate/hydroxyapatite composite scaffolds for bone tissue engineering: preparation, characterization, and in vitro studies. J Biomed Mater Res, Part B. 2004;71B(1):52–65. doi:10.1002/jbm.b.30065.
47. Yang F, Xia S, Tan C, Zhang X. Preparation and evaluation of chitosan-calcium-gellan gum beads for controlled release of protein. Eur Food Res Technol. 2013;237(4):467–79. doi:10.1007/s00217-013-2021-y.
48. Torres AL, Gaspar VM, Serra IR, Diogo GS, Fradique R, Silva AP, et al. Bioactive polymeric–ceramic hybrid 3D scaffold for application in bone tissue regeneration. Mater Sci Eng C. 2013;33(7):4460–9. doi:10.1016/j.msec.2013.07.003.
49. Jiankang H, Dichen L, Yaxiong L, Bo Y, Bingheng L, Qin L. Fabrication and characterization of chitosan/gelatin porous scaffolds with predefined internal microstructures. Polymer. 2007;48(15):4578–88. doi:10.1016/j.polymer.2007.05.048.
50. Jeong SI, Jeon O, Krebs MD, Hill MC, Alsberg E. Biodegradable photo-crosslinked alginate nanofibre scaffolds with tuneable physical properties, cell adhesivity and growth factor release. Eur cells Mater. 2012;24:331–43.
51. Freed LE, Vunjak-Novakovic G, Biron RJ, Eagles DB, Lesnoy DC, Barlow SK, et al. Biodegradable polymer scaffolds for tissue engineering. Nat Biotechnol. 1994;12(7):689–93.
52. Kokubo T, Takadama H. How useful is SBF in predicting in vivo bone bioactivity? Biomaterials. 2006;27(15):2907–15. doi:10.1016/j.biomaterials.2006.01.017.
53. Jalota S, Bhaduri SB, Tas AC. Using a synthetic body fluid (SBF) solution of 27 mM HCO3 − to make bone substitutes more osteointegrative. Mater Sci Eng C. 2008;28(1):129–40. doi:10.1016/j.msec.2007.10.058.
54. Lee JTY, Chow KL. SEM sample preparation for cells on 3D scaffolds by freeze-drying and HMDS. Scanning. 2012;34(1):12–25. doi:10.1002/sca.20271.
55. Schieker M, Seitz H, Drosse I, Seitz S, Mutschler W. Biomaterials as scaffold for bone tissue engineering. Eur J Trauma. 2006;32(2):114–24. doi:10.1007/s00068-006-6047-8.
56. Lawson MA, Barralet JE, Wang L, Shelton RM, Triffitt JT. Adhesion and growth of bone marrow stromal cells on modified alginate hydrogels. Tissue Eng. 2004;10(9–10):1480–91. doi:10.1089/ten.2004.10.1480.
57. Dittrich R, Tomandl G, Despang F, Bernhardt A, Hanke T, Pompe W, et al. Scaffolds for hard tissue engineering by ionotropic gelation of alginate-influence of selected preparation parameters. J Am Ceram Soc. 2007;90(6):1703–8. doi:10.1111/j.1551-2916.2007.01598.x.
58. Rassis DK, Saguy IS, Nussinovitch A. Collapse, shrinkage and structural changes in dried alginate gels containing fillers. Food Hydrocoll. 2002;16(2):139–51. doi:10.1016/S0268-005X(01)00071-6.
59. Deligianni DD, Katsala ND, Koutsoukos PG, Missirlis YF. Effect of surface roughness of hydroxyapatite on human bone marrow cell adhesion, proliferation, differentiation and detachment strength. Biomaterials. 2000;22(1):87–96. doi:10.1016/S0142-9612(00)00174-5.
60. Rechendorff K, Hovgaard MB, Foss M, Zhdanov VP, Besenbacher F. Enhancement of protein adsorption induced by surface roughness. Langmuir. 2006;22(26):10885–8. doi:10.1021/la0621923.
61. Lawrie G, Keen I, Drew B, Chandler-Temple A, Rintoul L, Fredericks P, et al. Interactions between Alginate and chitosan biopolymers characterized using FTIR and XPS. Biomacromolecules. 2007;8(8):2533–41. doi:10.1021/bm070014y.
62. Daemi H, Barikani M. Synthesis and characterization of calcium alginate nanoparticles, sodium homopolymannuronate salt and its calcium nanoparticles. Sci Iran. 2012;19(6):2023–8. doi:10.1016/j.scient.2012.10.005.
63. Tzaphlidou M, Zaichick V. Calcium, Phosphorus, calcium-phosphorus ratio in rib bone of healthy humans. Biol Trace Elem Res. 2003;93(1–3):63–74. doi:10.1385/BTER:93:1-3:63.

64. Mansur HS, Costa HS. Nanostructured poly(vinyl alcohol)/bioactive glass and poly(vinyl alcohol)/chitosan/bioactive glass hybrid scaffolds for biomedical applications. Chem Eng J. 2008;137(1):72–83. doi:10.1016/j.cej.2007.09.036.
65. Wei G, Ma PX. Structure and properties of nano-hydroxyapatite/polymer composite scaffolds for bone tissue engineering. Biomaterials. 2004;25(19):4749–57. doi:10.1016/j.biomaterials.2003.12.005.
66. Román J, Cabañas MV, Peña J, Doadrio JC, Vallet-Regí M. An optimized β-tricalcium phosphate and agarose scaffold fabrication technique. J Biomed Mater Res, Part A. 2008;84A(1):99–107. doi:10.1002/jbm.a.31394.
67. Shi L, Shi L, Wang L, Duan Y, Lei W, Wang Z, et al. The improved biological performance of a novel low elastic modulus implant. PLoS ONE. 2013;8(2):e55015. doi:10.1371/journal.pone.0055015.
68. Tam SK, Dusseault J, Bilodeau S, Langlois G, Hallé J-P, Yahia LH. Factors influencing alginate gel biocompatibility. J Biomed Mater Res, Part A. 2011;98A(1):40–52. doi:10.1002/jbm.a.33047.
69. Hu Y, Wang J, Xing W, Cao L, Liu C. Surface-modified pliable PDLLA/PCL/β-TCP scaffolds as a promising delivery system for bone regeneration. J Appl Polym Sci. 2014;. doi:10.1002/app.40951.
70. Dowling DP, Miller IS, Ardhaoui M, Gallagher WM. Effect of surface wettability and topography on the adhesion of osteosarcoma cells on plasma-modified polystyrene. J Biomater Appl. 2011;26(3):327–47. doi:10.1177/0885328210372148.
71. Karageorgiou V, Kaplan D. Porosity of 3D biomaterial scaffolds and osteogenesis. Biomaterials. 2005;26(27):5474–91. doi:10.1016/j.biomaterials.2005.02.002.
72. Renders GAP, Mulder L, Van Ruijven LJ, Van Eijden TMGJ. Porosity of human mandibular condylar bone. J Anat. 2007;210(3):239–48. doi:10.1111/j.1469-7580.2007.00693.x.
73. Dumas JE, Prieto EM, Zienkiewicz KJ, Guda T, Wenke JC, Bible J, et al. Balancing the rates of new bone formation and polymer degradation enhances healing of weight-bearing allograft/polyurethane composites in rabbit femoral defects. Tissue Eng Part A. 2014;20(1–2):115–29. doi:10.1089/ten.TEA.2012.0762.
74. Kamitakahara M, Ohtsuki C, Miyazaki T. Review paper: behavior of ceramic biomaterials derived from tricalcium phosphate in physiological condition. J Biomater Appl. 2008;23(3):197–212. doi:10.1177/0885328208096798.
75. Franco J, Hunger P, Launey ME, Tomsia AP, Saiz E. Direct write assembly of calcium phosphate scaffolds using a water-based hydrogel. Acta Biomater. 2010;6(1):218–28. doi:10.1016/j.actbio.2009.06.031.
76. Yin Y, Ye F, Cui J, Zhang F, Li X, Yao K. Preparation and characterization of macroporous chitosan–gelatin/β-tricalcium phosphate composite scaffolds for bone tissue engineering. J Biomed Mater Res, Part A. 2003;67A(3):844–55. doi:10.1002/jbm.a.10153.